DOCTORAL THESIS

Determination of the nature of radial transport in quasi-poloidal stellarator configurations

Departamento de Física

ESCUELA POLITECNICA SUPERIOR

UNIVERSIDAD CARLOS III DE MADRID

Author: Jorge Alberto Alcusón Belloso

Director/Tutor: Luis Raul Sánchez Fernández

Codirectors: J.M. Reynolds-Barredo, P. Xanthopoulos

Leganes, March 2017

DOCTORAL THESIS

Determination of the nature of radial transport in quasi-poloidal stellarator configurations

Author: Jorge Alberto Alcusón Belloso

Directors: Luis Raul Sánchez Fernández,
Jose Miguel Reynolds Barredo
Pavlos Xanthopoulos

Firma del Tribunal Calificador:

Presidente:

Vocal:

Secretario:

Calificación:

Leganes, de de

Dedicado a Juan Alcusón, Eloina López,
Manuel Belloso y Cristina Reyes.

Agradecimientos

Me van a permitir que los agradecimientos de esta tesis los realice en mi lengua materna, el español, ya que si bien las emociones y pasiones son en ocasiones difíciles de transmitir a través de un texto, posiblemente sea esta la mejor lengua que existe para expresarlos.

La presente tesis doctoral se ha llevado acabo gracias al apoyo y esfuerzo de mucha gente en el Departamento de Física de la Universidad Carlos III de Madrid. Quiero agradecer a todos los miembros del departamento sus gestos, ayudas y actitud. Sin duda todos ellos hacen que sea un lugar de trabajo incomparable. En concreto, me gustaría darle las gracias a mi director de tesis y tutor Raúl Sánchez, quien cercano y con infinita paciencia y conocimientos ha sabido guiarme estos años. Decir que Jose Miguel Reynolds ha sido simplemente mi codirector sería simplista y poco honorable, no sólo me ha ayudado como nadie, me llevo la amistad de una de las personas que posiblemente más han influido en mi vida recientemente. Gracias a Andrés Bustos, cuya dedicación y pasión me ayudaron siempre con una sonrisa. A Victor Tribaldos, quien con su encomiable trabajo al frente del cluster me salvó más de una vez estando a miles de kilometros. Ramón, seguramente la persona que más se preocupa por los doctorandos, siempre presto a ayudarnos. A Pavlos Xanthopoulos, que hizo que mis estancias en Greifswald fuesen mucho más sencillas y fructíferas. Y a todo el personal de la Residencia de Universitaria Fernando Abril Martorell (mi casa estos años) que me han facilitado enormemente mis labores como Subdirector. En especial a María Durbán, la directora.

Obviamente no puedo olvidarme de la caterva del ergástulo (o Calcuta, como nos gusta llamarlo). El mundo de la ciencia esta plagado de rarezas, y gente de muy diversa naturaleza. Encontrar un grupo tan amplio de gente que merece la pena, con la que trabajar, discutir, salir y con la que compartir taras mentales no es habitual y es todo un honor.

Mención especial para Rubén del Campo, quien tuvo el valor de irse a un despacho conmigo y aguantarme todo este tiempo (lo cual no es nada fácil dadas mis excentricidades) y con quien he compartido probablemente los mejores y peores momentos de este tiempo estando siempre para apoyarme, reir o ir a por una cerveza a Eulogio cuando ha hecho falta. Nos quedan muchas por tomar.

Gracias a todos mis amigos de Sevilla y compañeros de la Facultad de Física de Sevilla. Especialmente al Clú (Nacho, Salva, Álvaro y Sergio) teneros como amigos y quedar con vosotros es lo que me mantiene cuerdamente loco. A Omar, Pepo y Coco por dar rienda suelta a mi lado mas freaky. A la que siempre será mi compañera de prácticas e inspiración Lucía, a Julia (la más boni) y Álvaro porque me hacéis sentir en casa cada vez que voy a Sevilla. A Javier Mendez, Luly, Carmen y Phoebe que llevan conmigo toda una vida. Ana K. y Manu, mi pequeña comunidad sureña en Madrid.

No quiero dejar pasar la ocasión de acordarme de las personas que hicieron que me interesase por la Ciencia. Profesores como Amparo de la Torre, Justo Jimenez, Javier Romero Landa, Javier Brey o Maria Jose Ruiz Montero sin los que a día de hoy no estaría dedicándome a la investigación.

Dejo para el final las personas a las que más tengo que agradecer en la vida. Como ya he indicado, no soy una persona en ocasiones fácil, pero una madre es una madre, y si hay alguien que me ha aguantado y animado siempre incondicionalmente ha sido ella. Mi padre, sinónimo de esfuerzo y dedicación que siempre está preocupado porque mi hermano y yo luchemos en la vida. Y mi hermano Álvaro, la mejor persona que conozco.

Poniéndolo en perspectiva, todo lo anteriormente dicho es sólo un pequeño grano de arena. El resto de la playa es Irene. Sin ti simplemente no habría nada. Gracias a todos.

Summary

Nuclear fusion is one of the most promising solutions to the long-term energy needs of the world. Nevertheless, bringing the source of energy of stars to Earth is not easy. From the different options explored to produce fusion, magnetic confinement is the most developed one and, probably, the first that will be available. Tokamaks and Stellarators are the two most important configuration concepts of this kind, both having a toroidal shape.

The main problem magnetic confinement fusion suffers is that all configurations have important losses of energy and particles along the radial direction that makes achieving the required conditions a challenge. Traditionally, those losses have been modelled using neoclassical and turbulent descriptions that assume the existence of an underlying transport of diffusive characteristics. As a result, effective transport coefficients (diffusivities, viscosities, conductivities, etc.) have been estimated to describe the transport processes inside the plasmas confined in these magnetic configurations. Recently, it has been however suggested that there are several important regimes in these devices in which such an assumption may be wrong. As a result, these diffusive-like models may importantly misrepresent the transport dynamics and compromise the performance predictions of larger devices.

Among the situations identified where the nature of the radial transport may be fundamentally non-diffusive, there are two particularly meaningful for magnetic confinement devices (see Ref. [1] for a review). The first one is the case of near-marginal transport, in which the plasma profiles (for pressure, temperature, etc) wander locally very close to the thresholds for the excitation of instabilities. In such cases, radial avalanching may become the dominant form of transport, instead of diffusion [2, 3]. In next-generation tokamaks, such as ITER [4], predictions have been made for an almost near-marginal operation in some profiles, due to the

fact that turbulent fluxes scale with a large power of the plasma temperature. Thus, at the much hotter plasmas expected in ITER, this might certainly be an issue to consider. Another example, closer to what we are going to study in this thesis, is the case of radial transport across strong, radially-sheared zonal flows, as shown recently in tokamaks [5, 6, 7].

The problem studied in this thesis, however, refers to transport in stellarators, not tokamaks. Stellarators have seen a recent revival by improving the confinement properties of neoclassical guiding centre orbits by endowing the confining magnetic field with a hidden symmetry usually referred to as quasi-symmetry. Several types of quasi-symmetries exist. The most important ones are quasi-poloidal, quasi-helical and quasi-axisymmetric. We will discuss them in detail in later chapters but, for now, it suffices with saying that quasi-symmetric configurations have a better neoclassical confinement compared to that of standard stellarators. Experimental results from the HSX (helically quasi-symmetric) stellarator [8] have already provided evidence supporting an improved neoclassical confinement [9]. They also have smaller viscosities in the direction of the symmetry, which should in principle facilitate an easier excitation of flows, either by the turbulence itself or externally. Experimental evidence supporting this reduction is also available from HSX [10]. In this context, it is therefore a natural question to ask whether the reduction of losses and better confinement in quasi-symmetric configurations are a mere reduction of turbulent transport levels, or whether there is something more fundamental being changed. The investigation of the latter is where this thesis is centered, focusing in particular on quasi-poloidal configurations.

The reduction of the neoclassical poloidal viscosity expected for poloidally quasi-symmetric configuration should facilitate the self-generation of poloidal zonal flows, which are particularly important in terms of affecting radial transport [11]. From the previously mentioned tokamak evidence, it is therefore expected that nondiffusive features of transport might appear more strongly in poloidal quasi-symmetric configurations. Thus, the present thesis investigates whether this is the case or not. Or, more precisely, we will quantify the changes in the nature of radial turbulent transport and attempt to establish whether these changes are (or not) correlated to the level of quasi-poloidal symmetry of the configuration. In order to do it, many gyrokinetic turbulent simulations have been carried out, in a selected configuration with quasi-poloidal symmetry, using the GENE [12] gyrokinetic code (see Chapter 2). The degree

of quasi-symmetry of the selected configuration varies, however, strongly with radius. We have used this to our advantage by carrying out local simulations around different radial locations of the same configuration, which has yielded the plethora of data with which the comparative study previously described has been carried out.

The characterization of the nature or turbulent transport has been done by means of a methodology that employs tracked particles. These particles may be massless (i.e., tracers) or possess mass and charge. Either way, these particles are tracked as they are advected by the underlying turbulence (previously calculated by GENE) and, if massive, the different magnetic and parallel drifts that might be present. The temporal dispersion of an initial population of these particles can be used to determine the nature of radial transport rather easily, as we discuss in Chapter 3. However, advecting tracked particles within the advance loop of modern Vlasov gyrokinetic codes is very inefficient and highly unpractical. Gyrokinetic codes have high complexity, strong parallelization and a extremely delicate internal balance. For that reason, we have developed a new and independent tracking code, TRACER, that we have used to carry out all the studies in this thesis. The inner details of this new code are discussed at length in Chapter 4.

The discussion of the results of the comparative study previously mentioned is fleshed out in Chapter 5. The main conclusion we have drawn is that there is indeed a correlation between the level of quasi-symmetry and the nature of radial transport, which becomes more subdiffusive the larger the level of quasi-symmetry is. The nature of this change is also shown to be connected with the larger ability of the quasi-symmetric plasma to excite poloidal flows with strong radial shear, which is very reminiscent of what is found in tokamaks [7]. We have carried out this study both for tracers and massive ions, and very similar results are found in the long-term limit, which makes us believe that the conclusions of this thesis are of importance for the confinement of the thermally confined plasma.

The main results of this thesis have been presented in several international conferences and workshops, and have also seen publication in the international journal *Physics of Plasmas*. A complete list of these publications and presentations can be found in Appendix C. As a last note it is worth saying that, throughout the document, most of the variables will be expressed in GENE units. A very few variables, mostly related with

the description of the QPS-configuration, will be however expressed in the International System of Units. The abbreviations used in the document are always introduced and they are part of the general terminology used by the fusion community.

Contents

List of Figures

List of Tables

Chapter 1

Fusion basics

The reality of the world where we live in and human needs convert energy into one of the basic goods of our life. Capitalism, the fast growth of the population and the vast technological development of the last two centuries have increased the energy consumption to very high levels, turning the efficient and responsible production of the energy into one of the most important problems of humanity[13]. The problem is not trivial because it is not only a matter of producing energy efficiently; the environmental impact and its sustainability are also critical issues that must be taken into account in order to solve the whole problem [14, 15].

All sources that can be used to produce energy have associated costs and different environmental impacts. For example, fossils (petrol, coal, gas, wood,...) are cheap but very inefficient producing energy [16]. They are limited and involve numerous environmental risks such as global warming, pollution, the impact of mineral extraction, oil spills and other environmental disasters. During the last few decades, renewable sources have increased their presence in the energy production schemes of the most important economies, in part due to the better technology that is becoming available. The spread-out nature of renewable sources is however a big problem [17]. In addition, the energy produced must be consumed as it is generated, since there is not a reliable way to store large amounts of energy. These sources also have an impact on nature. For example, on animal behaviour such as wind energy that changes bird migration routes, or solar energy that may affect the Earth albedo to enumerate just a few of them. Nuclear fission is probably the most efficient of the sources of energy currently in use. It produces a great amount of energy at very

competitive costs [18, 19]. However, fission produces toxic and long-lived radioactive residues. It also requires severe security precautions to avoid disasters. Although existing nuclear power plants are very safe, they need very qualified staff and constant supervision that is not affordable for all the countries. They also have a social stigma based on the disasters of the past [20, 21]. To sum up, it is clear that there is no perfect source of energy and because of that, the most optimal strategy is to combine them in an way that permits them to contribute efficiently to the overall energy production, while, at the same time, trying to reduce as much as possible the emissions and the environmental risks. Even when few will oppose the goodness of the concept of an energy production system that relies on various sources of energy, fossil combustion represents today 80% of the total energy produced by humans worldwide [16].

In this global and challenging picture, nuclear fusion could play an important role in solving many of the future world energy problems. Nuclear fusion is a natural process that produces large amounts of energy. It is the most efficient source of energy (in terms of amount of energy generated per kg of fuel), while having a very low environmental impact. It produces no greenhouse gas emissions and no long-lived radioactive residues. *First-generation fusion reactors* will only produce some radioactive residuals due to the neutron activation of the reactor walls but, even in that case, the residues will have a short half-life (< 100 years) which reduces the risk of radioactive contamination and facilitates its control and disposal. The fuel that fusion requires (Deuterium and Lithium, the latter needed to breed Tritium) is abundant. In second-generation fusion reactors, that might be based on fusing Deuterium with itself, the prospects could be even better since Deuterium can be directly extracted from ocean water.

The ITER[1] project will try to demonstrate the scientific and technical viability of fusion energy production [22]. The main objective of this international reactor of the tokamak class, currently under construction in Cadarache (France), is to demonstrate to the world that fusion energy generation is a possible solution to the energy problem, opening the way to a new commercial power plants production.

[1] **I**nternational **T**hermonuclear **E**xperiment **R**eactor

1.1 Thermonuclear Fusion

Nuclear Fusion is a natural process where two light nuclei are combined into a heavier one. The final nucleus is more stable than the previous ones. The fusion reaction is thus exothermic, liberating energy in the process [23]. The excess of energy liberated during the fusion of nuclei increases the kinetic energy of the final products. In nature, many different fusion reactions are possible but the easiest one to produce on Earth, (because its cross section reaches a maximum value at the lowest temperature) occurs between two isotopes of hydrogen: Deuterium (D) and Tritium (T).

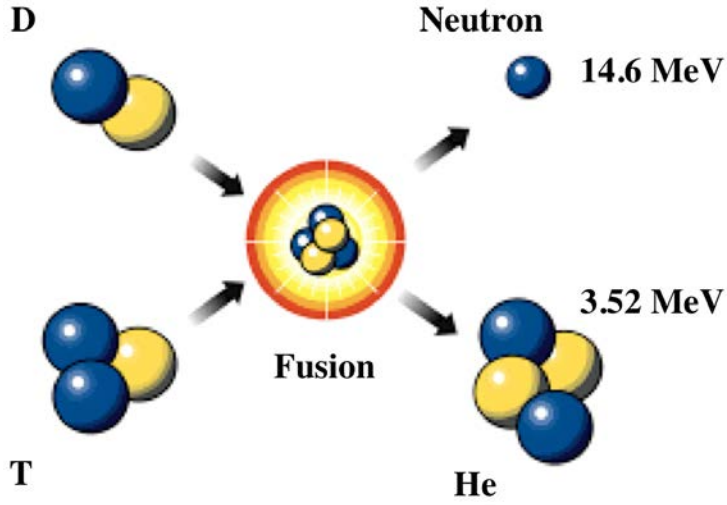

Figure 1.1: Deuterium-Tritium fusion reaction scheme. D represents Deuterium, T is Tritium and He refers to Helium (or α particles). Blue spheres represent neutrons and yellow spheres protons. The final kinetic energy of the resultant particles is expressed in MeV.

In the D-T reaction, most of the energy liberated is used to accelerate the neutron to a very high speed. The rest of the surplus energy increases the kinetic energy of the α-particle. The reactants, Deuterium and Tritium, are obtained in different manners. On one hand, Deuterium can be found anywhere where there is water, from which it can be ex-

tracted. Around 0.015% of the world water is heavy water (D_2O) which constitutes a large reserve of Deuterium [24]. On the other hand, Tritium is radioactive and has a short decaying life. Therefore, it does not exist on Earth and it needs to be manufactured in the laboratories. One interesting process for its obtention is to make the fast neutrons produced during the fusion reactions collide with Lithium to create Tritium. The relevant reactions of neutrons with the different isotopes of Lithium are:

$$\begin{aligned} {}^6Li + n &\rightarrow {}^4He + T + 4.8MeV \\ {}^7Li + n &\rightarrow {}^4He + T + n - 2.5MeV. \end{aligned} \tag{1.1}$$

In order to use these reactions, future fusion reactors would need to include some kind of external Lithium layer where the Tritium could be produced on-site. Fusion reactors will also take advantage of this Lithium layer to slow down the fast neutrons created inside of the reactor and to absorb the heat that could then be converted into electricity. The actual Lithium reserves are located within the Earth crust (92.5% corresponding to ${}^6Li$ and 7.5% to ${}^7Li$). They are as large as what is required to generate electricity for the whole world for some centuries.

It has been predicted by many that future fusion reactors will probably be developed into two different generations. As was previously said, the first generation would need to manufacture the Tritium that is used as fuel. The second generation of fusion reactors, however, will fuse just Deuterium nuclei. Efficient deuterium fusion requires much higher temperatures, which means that they will be technologically much more complicated. Their main advantage is that they do not need Tritium to be manufactured, and that the neutrons produced will have smaller energies (at least the majority of them, since some D-T fusion reactions will still take place due to the fact that Tritium is one of the products of one type of D-D reactions), which will in theory reduce the radioactive activation problems. The relevant Deuterium reactions are, in this case:

$$\begin{aligned} D + D &\rightarrow {}^3He(0.82MeV) + n\ (2.45MeV) \\ D + D &\rightarrow T\ (1.01MeV) + p\ (3.03MeV) \\ D + {}^3He &\rightarrow {}^4He\ (3.67MeV) + p(14.67MeV). \end{aligned} \tag{1.2}$$

From the environmental point of view, the by-products of fusion reactions are not toxic [24]. They do not cause greenhouse effects. First

generation reactors would use Tritium, that is radioactive but has a very short half-life ($\sim$ 12 years). The internal structure of the reactor will be activated due to the interaction with fast neutrons, but it will decay relatively quickly ($\sim$ 100 years), which permits it to be safely disposed of. In addition, the amount of fuel necessary for the reactions will be of the order of a few grams per discharge inside of the reactor, which will reduce the risk of any radioactive escapes.

1.2 Nuclear fusion conditions

Nuclei are positively charged and repel each other due to the Coulomb electric force. In order to produce a fusion reaction it is necessary to provide enough energy for the nuclei to overcome their mutual Coulombian repulsion. The optimal temperature for the reaction to take place is fixed essentially by the cross-section of this process. Once the reaction temperature is determined, a threshold value for the product of plasma density and energy confinement time must be overcome for net energy to be produced. Therefore, one can only vary either the density of the plasma, or the amount of time that the plasma must be confined at the conditions in which reactions can take place significantly.

1.2.1 Energy balance: break-even and ignition

The main objective of a fusion reactor is to produce net energy. This means that, at the end of the process, the total amount of energy used to achieve the confinement, to bring the plasma to the proper conditions and to produce the fuel, among others, must be less than the energy finally produced by the reactor.

Using the Equipartition Theorem [25], a plasma with density n and temperature T has a thermal energy density of $3nT$, half of it in the electrons, the other half in the ions. The main contributions to the energy losses are heat and particle transport along the radial direction plus the radiation losses (mostly, *bremsstrahlung*). It is traditional to define a characteristic time τ to quantify the energy confining time:

$$\tau = \frac{3nT}{P_{lost}}, \tag{1.3}$$

where the total losses are the sum of both contributions $P_{lost} = P_{hp} + P_B$. P_{lost} is the power density lost by all loss channels. In particular, heat and particle transport, P_{hp}, and radiation transport due to *bremsstrahlung*, P_B.

When the energy produced from fusion equals the energy losses, the reactor reaches an state of *break-even* that is defined by the balance equation:

$$P_{hp} + P_B = \eta(P_F + P_{hp} + P_B). \tag{1.4}$$

This expression is known as the Lawson criteria [26]. In it, P_F is the density of power generated by the fusion reaction. η represents the thermic to electric energy efficiency conversion ratio, that is typically $\sim 1/3$. Combining expressions (1.3) and (1.4) a criterion to go beyond *break-even* is obtained that only depends on temperature. Namely,

$$n\tau \geq f(T). \tag{1.5}$$

This function reaches a minimum value, for the *D-T* fusion reaction, at a temperature of around $T = 20keV$ (roughly, two hundred million degrees). Assuming a thermic-electric conversion ratio $\eta = 1/3$, the value of the product at that temperature is $n\tau \sim 4 \times 10^{19} m^{-3} s$.

The *break-even* state is however not the final objective to reach. It still requires external energy to keep the process going. In a real reactor, the majority of this energy should be provided by heating from the α-particles produced during the fusion reaction, that remain confined in the reactor. When the reactor is in that state, it is said to have reached *ignition*. The condition for the *ignition* state is:

$$P_{hp} + P_B = P_\alpha, \tag{1.6}$$

that is equivalent to the Lawson criteria when using $\eta = 0.136$ [27]. For the *D-T* reaction, the ignition condition at the optimal temperature ($T \sim 20keV$) is

$$n\tau_{ignition} \approx 5 n\tau_{Lawson} = 2 \times 10^{20} m^{-3} s. \tag{1.7}$$

The ignition condition is around five times the breakeven condition because only a 20% of the energy in the fusion reaction is given to the α particle that, being charged, can be maintained inside of the reactor. The rest, around 80% of the energy, is taken out of the reactor by the fleeing neutrons.

1.3 Fusion plasma confinement methods

As we already said, fusion is a natural reaction that happens when two light nuclei approach each other with sufficient energy as to overcome the Coulomb repulsion between them. As the magnitude of this repulsion is proportional to the product of the charges, achieving fusion becomes more difficult as the nuclei become heavier. That is why hydrogen isotopes will be used as fuel in the first fusion reactors on Earth. Fusion reactions often occur in nature, for example inside stars. In this case the huge mass of these celestial objects (the mass of our Sun is, for instance, $m \approx 10^{30} kg$) creates an enormous pressure at the center that is more than sufficient to create the conditions needed to fuse the hydrogen inside. On Earth, other strategies must be devised to overcome the Coulombian repulsion between the positive ions. There are two main routes being currently pursued to overcome the Lawson criterium once a plasma temperature of the order of one hundred million degrees has been achieved (see Eq. 1.4): i) small confinement times combined with high plasma densities or ii) moderate confinement times at low plasma densities. Both routes define the two main strategies developed and studied to produce fusion energy on Earth.

The first route, that considers very small confinement times ($\tau \sim 10^{-12} - 10^{-8} s$) and high densities ($n \sim 10^{28} - 10^{32}$particles/m^3), is the basic principle of inertial confinement, that works by firing hundreds of high-power lasers onto a small spherical pellet (*hohlraum*) filled with a mixture of Deuterium and Tritium. The implosion of the pellet is so violent that a very dense plasma is created inside, in which fusion reactions would take place [28].

The second option, moderate confinement times ($\tau \sim s$) and low densities ($n \sim 10^{20} - 10^{21}$particles/m^3), is the basis of magnetic confinement, where a strong magnetic field is used to isolate the plasma inside the reactor chamber. We discuss it in much more detail in the next section.

1.4 Magnetic confinement of nuclear fusion

From all of the different possibilities to confine fusion plasmas, one of the most promising is magnetic confinement. Fusion plasmas must be maintained at very high temperatures (millions of K) and it is thus necessary to isolate and concentrate the plasma (and heat) away from the material walls. Magnetic confinement fusion uses magnetic fields to confine the

plasma, taking the advantage of the fact that plasmas are constituted by charged particles. The type of configurations used in magnetic confinement fusion are often referred to as *magnetic bottles*.

The easiest manner to create a magnetic bottle is by using coils. Any magnetic field must satisfy $\nabla \cdot \mathbf{B} = 0$ which means that the magnetic field lines are either infinite, extending to infinity or ergodically filling a volume or surface, or finite but closing on themselves. This fact, together with the rest of Maxwell equations and other equilibrium and stability considerations imposes severe restrictions on the possible geometric configurations for the magnetic field. The most successful magnetic bottles are based on the combination of a toroidal magnetic field $\mathbf{B}_\phi$ and a poloidal magnetic field $\mathbf{B}_\theta$, the latter being needed to compensate radial particle drifts that might push the plasma out of the configuration [27].

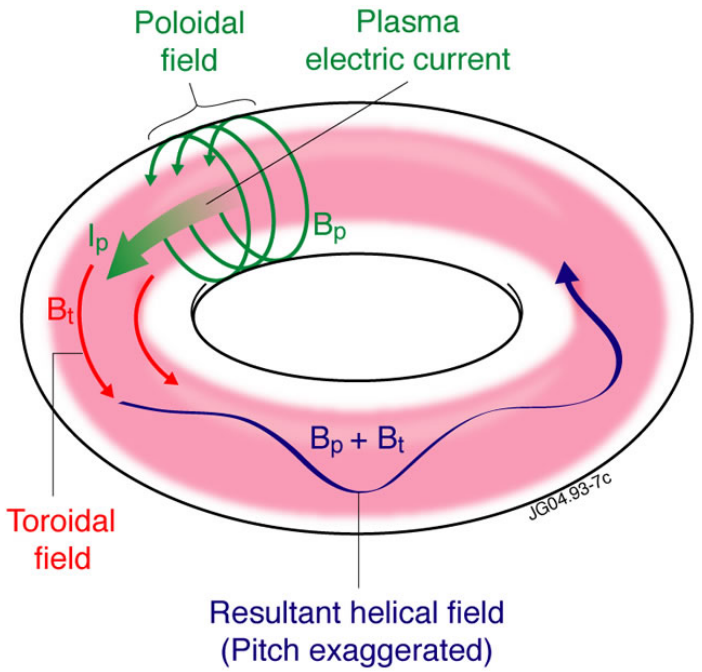

Figure 1.2: Magnetic field combination of poloidal B_p and toroidal B_t components in a toroidal reactor with the plasma coloured in pink. In this case, the poloidal field component B_p is generated with a toroidal electric current I_p.

Nevertheless, certain choices for the toroidal and poloidal mag-

netic field components have been demonstrated to be better in the art of confining a hot fusion plasma. In general, these configurations are formed by a system of nested toroidal magnetic field surfaces [27]. In the simplest case, the magnetic configuration is a family of nested tori with a common axis refereed to as the *magnetic axis*. These surfaces are defined by the magnetic field lines of the configuration, since each of them must be contained in a single magnetic surface. When lines close on themselves after a few toroidal turns, the surface that contains them is called a *rational surface*. If the line, on the other hand, fills the surface ergodically, it is an *irrational surface*. More complicated topologies are also possible, with individual field lines filling ergodically a volume inside the configuration, or giving rise to other structures such as *magnetic islands*. Each magnetic surface is usually labeled by a number (or *flux coordinate*). Not every quantity is useful for this task. It must be a *surface quantity*. That is, a quantity that is constant on the surface such as the toroidal or poloidal magnetic fluxes inside of the surface, to name a few. Another important surface quantity is the *rotational transform*. It is defined as the number of poloidal turns that a magnetic field line undergoes during one toroidal turn:

$$\iota = \frac{\text{Num. Poloidal turns}}{\text{Num. Toroidal turns}}. \tag{1.8}$$

Sometimes, the inverse of this magnitude $q = 1/\iota$ is used. It is called the *safety factor* because it plays an important role in ensuring the configuration stability.

There are two different toroidal configurations that look particularly promising as future magnetic confinement fusion reactors: *tokamaks* and *stellarators*. The most important difference between both concepts is how they create the poloidal magnetic field component $\mathbf{B}_\theta$. We discuss them separately next.

1.4.1 Tokamak

Originally developed in the URSS during the 50's, the Tokamak[2] concept is the most studied and developed of all toroidal magnetic confinement concepts [29]. In a tokamak, the toroidal magnetic field component is created by means of external coils but the poloidal component is created by inducing an internal toroidal current in the plasma of the order of

[2]Russian acronymous for toroidal chamber with magnetic coils.

several *MA*. The toroidal current is also used to heat the plasma (process known as Ohmic heating). The toroidal current is induced by making the plasma behave as the secondary of a large transformer, which makes the tokamak an intrinsically pulsed system, which is not optimal. On the other hand, it also makes the tokamak configuration toroidally symmetric to a large approximation, which has many advantages.

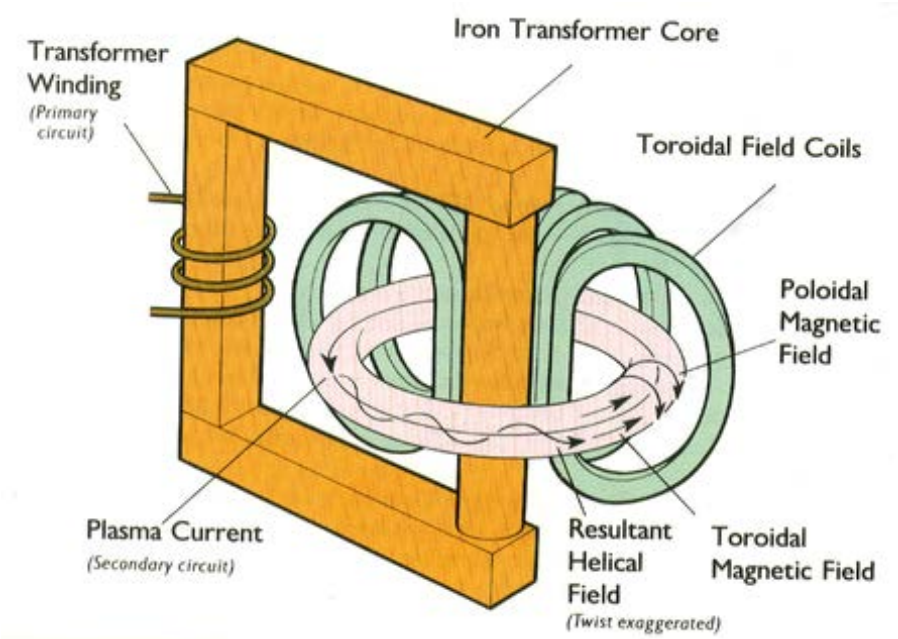

Figure 1.3: Basic Tokamak schedule with some of the external modular coils in green, and the iron transformer core, in orange, which induce the plasma current and change its polarity.

The pulsed operation is not the only inconvenience of the Tokamak configuration. The use of a large plasma current to create the poloidal component of the magnetic field provides a large source of free energy that can lead to the excitation of instabilities, some of which (know as disruptions) may destroy the configuration, if unchecked [29]. Disruptions are considered as one of the worst problems for tokamaks because they destroy the confinement but might also damage the walls of the reactor.

Nowadays, the most important tokamak in operation (in terms

of size, results and budget) is JET[3] in Culham, Oxfordshire (United Kingdom)[30]. This device has reached conditions close to breakeven, although using only a highly-diluted $D-T$ mixture used for safety reasons. Most of the experiments, up to this day, have been made instead just with Deuterium. These experiments set the basis for the ITER development [31]. By extrapolating the JET (and many other tokamaks) results to the size of ITER, the international reactor is expected to be able to be operated beyond the breakeven point. ITER will operate with a plasma formed by 50% of Deuterium and 50% of Tritium for the first time. Figure (1.4) shows the huge size of the machine. ITER is one of the biggest experiments in the world, and the third most expensive project of the humanity (behind Moon's landing and CERN).

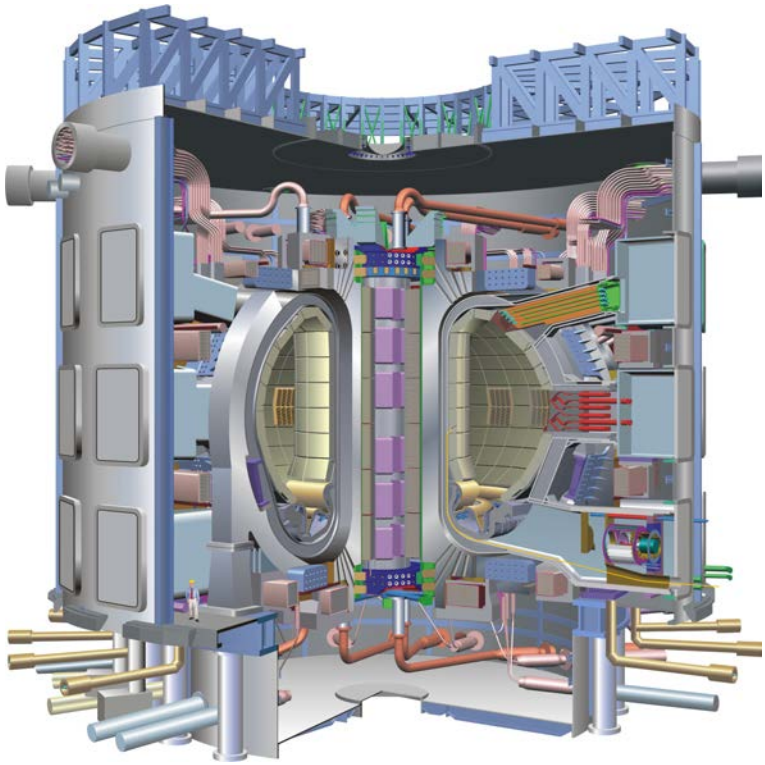

Figure 1.4: ITER reactor. Internal cross-section of the design with all the elements in different colours and in scale with human size.

[3] **J**oint **E**uropean **T**orus.

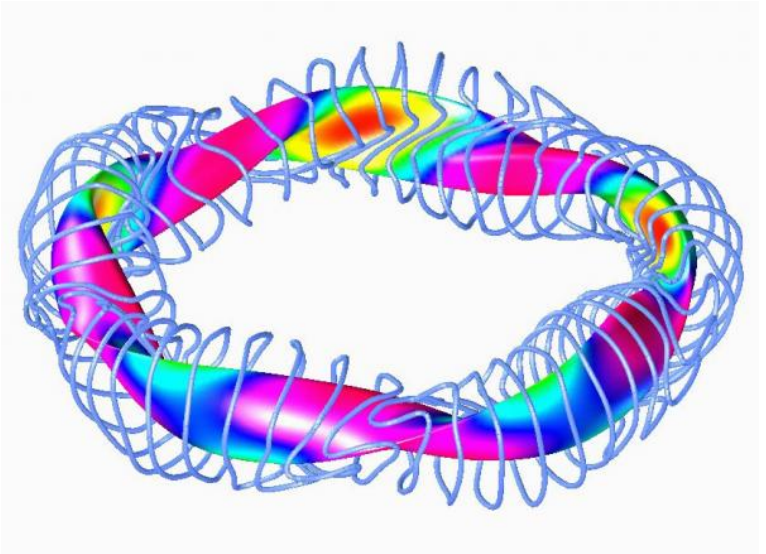

Figure 1.5: Illustration of the Wendelstein 7-X stellarator showing the set of twisted coils and the complicated plasma shape.

1.4.2 Stellarators

The second main toroidal magnetic configuration is the stellarator[4] [32]. It was first proposed by L. Spitzer in 1950 and built for the first time in the Princeton Laboratory of Plasma Physics (New Jersey, U.S.A)[33]. During the 50s and 60s, stellarators were very popular but tokamaks became more important after the 70s due to their much better performance and lower costs.

In stellarators, the poloidal component of the magnetic field is generated in the same way as the toroidal component of the magnetic field: with external coils. A consequence of this is that the magnetic field configuration becomes fully tridimensional. In order to have good properties, stellarators have external coils that may become very twisted and with a confined plasma with very complicated shapes (see Fig. 1.5). For the actual and next generation of stellarators, these coils will be made of superconductive materials which are very expensive and not easy to manipulate, even more for those complicated shapes. The topology of the resulting magnetic fields is more complicated than for tokamaks. In

[4]Combination of **Stella** which means star and gene**rator**.

addition, the lack of toroidal symmetry implies that particle motion is more complex and less easily confinable, which has often resulted in worse confinement properties as compared with tokamaks [32]. Stellarators also need external heating from the start, since they have no significant Ohmic heating created by internal currents. In contrast, tokamaks need external heating only after the plasma exceeds a minimum temperature beyond which Ohmic heating ceases to be efficient, due to the negative scaling of the plasma resistivity with temperature.

On the plus side, stellarators have a continuous operation regime, not pulsed as in tokamaks, which is more attractive for a future reactor. Stellarators do not have disruptions because of the absence of significant toroidal currents. Nowadays, tokamaks are at least one generation beyond stellarators. Nevertheless, stellarators have become more competitive in the last couple of decades due to the increasing availability of better supercomputers that have been used to design them and to optimize their properties before construction. In that sense, LHD[5] [34] in Nagoya (Japan), TJ-II in Madrid (Spain) [35] and the Wendelstein 7-X [36] in Greifswald (Germany) are the best examples.

1.4.3 Quasi-symmetries

Certain strategies have shown promising results that point in a clear direction in order to improve the confinement time of stellarator reactors. The resulting magnetic configurations have an internal hidden symmetry (or a partial symmetry) referred to as *quasi-symmetries* [37], although some of them require a small plasma current flowing in order to achieve them. Quasi-symmetries become apparent when the magnetic field is expressed using Boozer coordinates (s_B, θ_B, ϕ_B)[6] [39]. In that case, the motion of the ion guiding-centre (that is, the motion of the center of the helical trajectory of the ion in the magnetic field) becomes dependent on just the magnetic field magnitude $B = |\mathbf{B}|$ and its derivatives. Then, one takes advantage of the double periodicity of the toroidal geometry and expresses the magnetic field strength as a combination of poloidal and

[5] **L**arge **H**elical **D**evice.

[6] Boozer coordinates will be explained in detail in the Chapter 2. At this point it is sufficient to say that s_B is a radial coordinate, θ_B a poloidal coordinate and ϕ_B a toroidal coordinate.

toroidal modes in Fourier space:

$$B(s_B, \theta_B, \phi_B) = \sum_m \sum_n B_{m,n}(s_B) \cos\left(m\theta_B - n\phi_B\right). \tag{1.9}$$

A magnetic configuration is called *quasi-symmetric* if it is designed with an harmonic content of B with a specific dominant linear combination of poloidal and toroidal modes $M\theta_B - N\phi_B$. There are different combinations, but the most important can be classified in three different groups: *i) quasi-poloidal symmetry* if $M = 0$ and N is free, *ii) Quasi-axisymmetry* or *quasi-toroidal symmetry* if $N = 0$ and M free, and *iii) quasi-helical symmetry* when a certain pair of integers $M/N = m_h/n_h$ define the configuration. Examples of quasi-symmetric configurations are the HSX[7] [8] quasi-helical ($m_h = 1$, $n_h = 4$) stellarator currently in operation at the University of Wisconsin, the QPS[8] [38] and the NCSX[9] (quasi-axisymmetric) devices [41]. The latter two projects were regretfully cancelled. The different quasi-symmetries of the magnetic field are illustrated in Fig. 1.6, where the left column shows isocontours of the magnitude of the magnetic field on a selected magnetic surface for the HSX, QPS and NCSX devices, respectively. For comparison purposes, the first row of the figure also includes the same isocontours but for a generic, non-quasi-symmetric configuration (from the LHD device [34] in Japan). Clearly, the contours of constant magnetic field approximate follow vertical (for QPS), horizontal (for NCSX) and diagonal (for HSX) directions, whilst the generic stellarators does not have such a clear alignment.

It is thus clear that, in the three cases of quasi-symmetry, the magnitude of the magnetic field on any given surface only depends on one angular variable (θ, ϕ or a linear combination of them) instead of two, like in most other configurations[10]. The fact that the magnetic field amplitude loses one angular dependence improves the confinement of the guiding centre orbits due to the fact that there is an additional conserved quantity, associated to the new (approximated) symmetry [37]. Indeed, in the absence of the quasi-symmetry, the guiding-centre motion has only two constants of motion: the energy E and the magnetic moment μ.

[7] **H**elical **S**tellarator e**X**periment.

[8] **Q**uasi **P**oloidal **S**tellarator.

[9] **N**ational **C**ompact **S**tellarator e**X**periment.

[10] In general, the magnetic field vector **B** will still depend on the three coordinates.

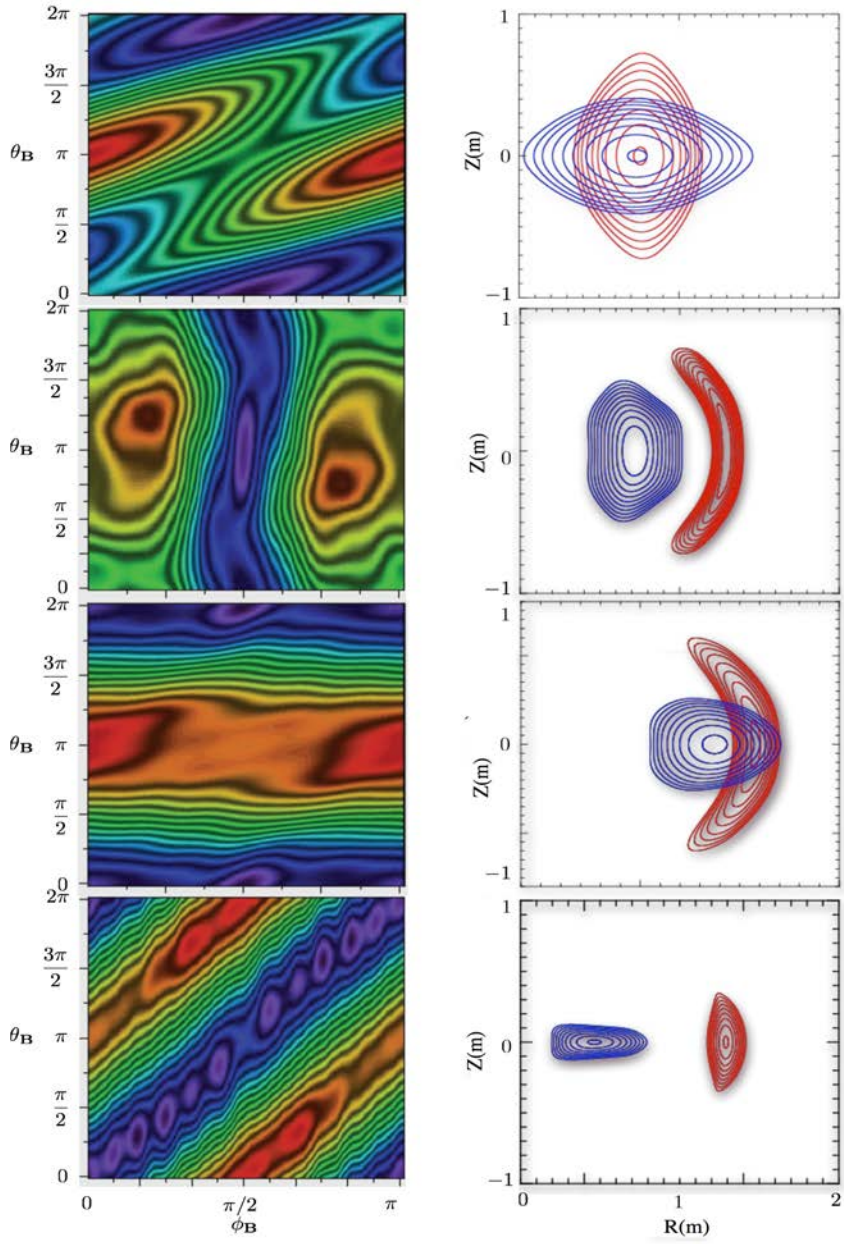

Figure 1.6: (Left) Isocontours for the magnitude of the magnetic field on a magnetic surface represented in Boozer angles; (Right) cross-sections of a set of selected magnetic surfaces at toroidal angles $\phi = 0$ and π/N_p, where N_p is the number of periods. From the top to the bottom, the devices are: LHD, QPS, NCSX, and HSX.

But the existence of one additional constant further constrains the orbits which improves their confinement. The canonical momentum associated with the quasi-symmetry plays that role. Then, Tamm' s theorem is sufficient to ensure that that particles will not displace themselves radially over too long distances [37].

However, real devices are never exactly quasi-symmetric. They have spatial regions where the level of quasi-symmetry is higher or lower depending on the coil distribution and the plasma current, among other things. Usually, the level of quasi-symmetry depends on the radial coordinate. In order to quantify this level we will use the *degree of quasi-symmetry* defined at each flux surface (s_0) by the ratio:

$$\sigma_{MN}(s_B) = \frac{\sum\sum_{MN} |B_{MN}(s_0)|}{\sum_m \sum_n |B_{mn}(s_0)|} \leq 1, \tag{1.10}$$

where the numerator is a sum only over the quasi-symmetric modes ($m = M, n = N$), whilst the denominator sum is over all Fourier modes. Therefore, perfect quasi-symmetry would require $\sigma_{MN} = 1$.

1.5 Transport in fusion plasmas

One of the main problems in magnetically confined plasmas is that energy and particles are lost too quickly across magnetic surfaces. Or, in other words, that particle and heat transport is very large along the radial direction. Therefore, the determination of the causes for these confinement losses, their characterization in terms of different parameters and the optimization of configurations to minimize them have become central problems in this field. The two main processes that drive transport radially out of magnetically confined fusion plasmas are collisions and turbulence.

1.5.1 Neoclassical transport: diffusion.

When ions and electrons in the plasma collide, they change the pitch of their velocity and, as a result, the location of their guiding center is displaced. Due to the nature of the process, this displacement can happen in any direction across magnetic surfaces. Since these displacements cancel each other out over time unless gradients exist across magnetic surfaces, collisions can only drive transport across magnetic surfaces if there is

a gradient across them for particle density, heat, pressure or any other quantity of interest. Regretfully, this is indeed the case of any fusion experiment, where huge radial gradients are established between the center and the plasma edge.

If one assumes that typical scales in length and time can be found, the simplest model to quantify these processes is then provided by the relation between fluxes and gradients of different quantities usually known as Fick's law [42] (or Fourier's law, for heat transport),

$$\Gamma = -D\nabla n \tag{1.11}$$

$$Q = -\kappa\nabla T, \tag{1.12}$$

where Γ represents the particle flux, Q the heat flux, D is the diffusivity coefficient and κ the thermal conductivity, that is related with the heat diffusivity coefficient through $\kappa = n\chi$. These effective transport coefficients must be determined either phenomenologically or from theoretical considerations. The simplest estimate can be done using a random walk (RW) model [43]. In this model, walkers make jumps of length Δr after waiting at rest for a lapse of time Δt. Walkers transport can then be modelled using Fick's law with a diffusivity D given by:

$$D \sim \frac{(\Delta r)^2}{\Delta t}. \tag{1.13}$$

In a fully-ionized plasma as those confined in a tokamak or stellarator, Coulombian collisions between particles are governed by the mean free path between collisions Δr, that is of the order of the Larmor radius orbit, and the inverse of the collision frequency between different particles $\Delta t = 1/\nu$, that sets the typical time scale.

Realistic estimates of collisional transport in magnetically confined plasmas must however consider the real and complicated geometry of the magnetic configurations. In that case, the mathematical formalism is known as *Neoclassical transport theory* [44, 45]. The complex geometry forces to consider two different types of particles: *passing particles* and *trapped particles*. Trapped particles appear because the magnetic field is not homogeneous, but depends on space. The reason is rather simple. When particles (ions or electrons) move along a field line, they must conserve their energy $E = (1/2)mv^2$ and magnetic momentum $\mu = mv_\perp^2/2B$. On the other hand, the total energy can be expressed as

$E = (1/2)mv_{\parallel}^2 + \mu B$, where $v_{\parallel}$ is the parallel velocity along the field line. The parallel velocity is thus given by $v_{\parallel} = \sqrt{2E/m - \mu B}$. Clearly, if the energy of particle is small enough, the particle may encounter, as it moves along the field line, locations where the magnetic field is sufficiently large as to make the argument of the square root that defines $v_{\parallel}$ vanish. At those locations, the particle must reverse its parallel velocity (otherwise, the parallel velocity would become an imaginary number!), and the particle is said to be trapped. The projection of a trapped orbit on any toroidal cross-section looks like a banana, which gives its popular name to trapped particle orbits: banana orbits (see Fig. 1.7).

A passing particle, on the other hand, has a sufficiently large energy as to be able to stay always moving in the same direction. Their projected orbits look more like circles. These two type of particles behave very different, in terms of transport, when a collision takes place. A passing particle, when it collides, may displace itself radially a length of the order of a Larmor radius; trapped particles, on the other hand, suffer radial displacements which are much larger, of the order of the banana radial width. Therefore, they must accounted for separately when estimating radial transport. In fact, banana orbits increase transport levels considerably compared to what one would obtain if only passing particles are considered [11].

Finally, it is essential to remark that, in neoclassical transport theory as in many other transport formalisms used in plasmas and elsewhere, effective transport coefficients are determined by implicitly assuming that typical scales (in space and time) for radial transport exist. Otherwise, a diffusive description of transport would fail to capture the underlying dynamics [1].

1.5.2 Turbulent transport

Regretfully, neoclassical transport theory cannot explain the full levels of radial transport observed in fusion plasmas. Real fusion experiments usually have much larger radial transport than the one predicted by neoclassical theory [46]. Traditionally these discrepancies have been hidden under the general term *anomalous transport*, mainly because it was not clear which the real process behind was. Nowadays, it is widely accepted

[11] The trapped/passing duality is in fact also responsible for many other important process, such as the excitation of bootstrap currents [44, 45].

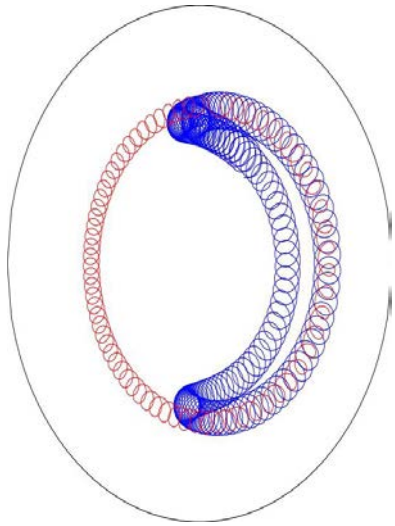

Figure 1.7: Different orbits of charged particles according to the neoclassical theory. In red, passing-particles. In blue, trapped particles.

that turbulence is the dominant mechanism of transport across magnetic surfaces controlling, in the last instance, the confinement time of the device. Turbulent fluctuations (in all plasma fields including electric and magnetic fields, density, temperature, etc) driven by various sources of free energy (gradients, currents, etc) are responsible for the majority of the observed radial transport. In particular, across the magnetic surfaces, the main contribution to the transport appears to be associated to the contribution of turbulence to the electrostatic $\mathbf{E}\times\mathbf{B}$ drift.

Traditionally, in the theory of plasma physics, effective coefficients of transport such as diffusivities or viscosities have also been used to describe turbulent transport. This has been the go-to strategy even when, sometimes, there is evidence supporting the fact that a diffusive description may fail to capture the nature of the transport dynamics. The process usually goes as follows. First, each variable is decomposed in two terms: an average value (either in a ensemble or temporal sense) and a fluctuation with zero-average. For instance, density would become:

$$n(x,t) = n_0(x) + \tilde{n}(x,t). \tag{1.14}$$

Using this decomposition, non-zero average turbulent fluxes are easily estimated. For instance, the electrostatic particle and heat fluxes are obtained

as:

$$\Gamma \sim \langle \tilde{n}\tilde{v}_r \rangle \,, \quad \text{and} \quad q \sim n_0 \left\langle \tilde{T}\tilde{v}_r \right\rangle + T_0 \langle \tilde{n}\tilde{v}_r \rangle \,, \quad \text{with} \quad \tilde{v}_r \propto \tilde{E}_r, \tag{1.15}$$

where Γ and q are the radial particle and heat (conductive and convective) turbulent fluxes, $\tilde{n}$ represents the fluctuation of the density, $\tilde{T}$ represents the fluctuation of the temperature, and $\tilde{v}_r$ the fluctuation of the radial component of the plasma velocity. This turbulent fluxes are clearly non-zero because they are quadratic in the fluctuations. The flux is ultimately proportional to the fluctuating radial electric field, due to the dominance of the $\mathbf{E}\times\mathbf{B}$ drift, which is determined by the fluctuations of the electrostatic potential $\tilde{\mathbf{E}} = \nabla\tilde{\phi}$. It is worth to say that the level of the turbulent fluxes depends not only on the magnitude of fluctuations, but also on the phase difference between them. Indeed, only when $\tilde{n}$ or $\tilde{T}$ are in phase with $\tilde{E}_r$ are in-phase (i.e., their relative phase difference is zero), significant transport ensues. If they are out of phase (i.e., relative phase difference of $\pi/2$), there is not net transport.

As previously mentioned, a diffusive effective description is often forced at this point by assuming the existence of effective transport coefficients. For instance, we would have, for the particle and conductive heat fluxes, that they become expressed as:

$$\Gamma \sim \langle \tilde{n}\tilde{v}_r \rangle \simeq -D_{\text{eff}} \nabla n_0, \quad \text{or} \quad q^{\text{conductive}} \sim n_0 \left\langle \tilde{T}\tilde{v}_r \right\rangle \simeq -\chi_{\text{eff}} n_0 \nabla T_0, \tag{1.16}$$

so that transport driven by turbulence becomes encapsulated within the effective (or *eddy*) diffusivity D_{eff}. There are instances in which such approach probably fails to capture the transport dynamics in fusion plasmas (see Ref. [1] for a review). Examples can be found, for instance, in cases where turbulence is near-marginal (that is, where the profiles that drive the turbulence wander around the local threshold values for unstable modes to be excited), and in the presence of strong radially-sheared poloidal flows.

1.5.3 Drift-wave turbulence

It is believed that the instabilities responsible for most of the electrostatic fluctuations are of the drift-wave type [47]. The mechanism behind drift waves is simple. When a three-dimensional density fluctuation with parallel wavenumber (with respect to the background magnetic field) $k_\parallel \neq 0$

appears in the presence of a density gradient ∇n, drift waves appear. The procedure is illustrated in the left frame of Fig. 1.8. Electrons ($-$) are faster than ions ($+$) and react first to the parallel density gradient ∇n. As they move against the density gradient they leave behind regions with a positive charge excess. These changes drive an electrostatic potential $\tilde{\phi}$ whose fluctuations generate turbulent $\mathbf{E}\times\mathbf{B}$ drifts that move the ions, causing the wave to advance in the poloidal (ion diamagnetic) direction. If the reaction of the electrons is very fast, almost instantaneous, the cross-phase between potential and density perturbations remains close to zero and the drift wave is stable. The net transport is then zero (since the difference in phase between $\tilde{n}$ and $\tilde{E}_r$ will be close to $\pi/2$). The approximation of instantaneous electrons is usually known as *adiabatic electrons*.

However, if there is a delay in the electron response, the response is then non-adiabatic, the cross-phase is no longer zero and the drift wave may become unstable. It may also happen that the ion $\mathbf{E}\times\mathbf{B}$ motion is strongly perturbed, yielding a non-zero cross-phase and causing the drift wave to become unstable. In either case, strong radial turbulent transport ensues. Usually, one refers to each case as one of *electron* or *ion drift wave turbulence* [47].

In toroidal fusion plasmas, there are three important types of drift-wave micro-instabilities: *i) the ion temperature gradient mode (ITG), ii) the electron temperature gradient mode (ETG) and iii) the trapped electron mode (TEM).* In each case, the radial transport driven by the instability is most important at different spatial scales. TEM and ITG driven transport preferentially takes place at the ion Larmor radius scale, whilst ETG dominates at the scale of the electron gyroradius.

The right frame of Fig. 1.8 shows these different scales for each instability. The linear growth rate γ of the instability is shown as a function of the perpendicular wavenumber k_y for a typical tokamak. The physics of each of them is different. For TEMs, it is the trapping of electrons as they move along the field line that perturbs the electron response, making the wave unstable. For ITGs, the ion perpendicular motion is distorted by toroidicity in the presence of a ion temperature gradient. ETGs are similar to ITGs, but for electrons. We discuss them separately in what follows.

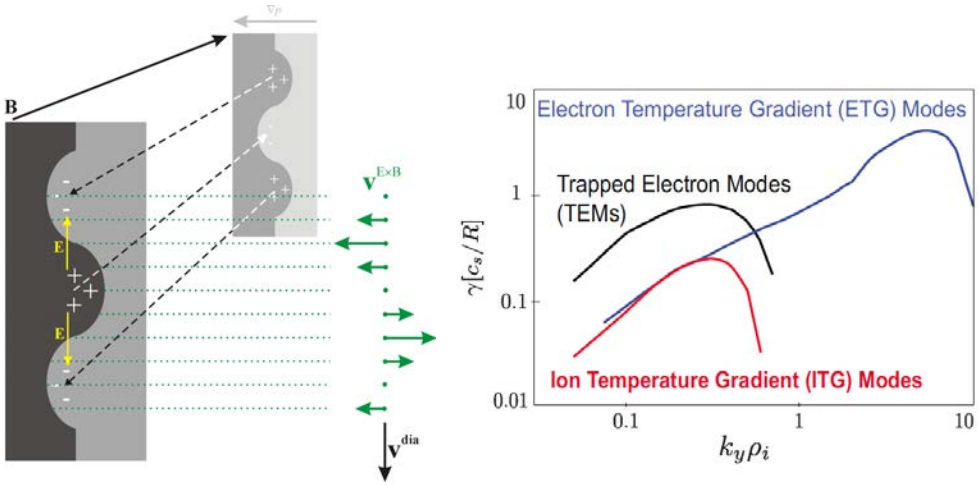

Figure 1.8: Left: sketch of the drift wave instability. The stability of the drift-wave depends on the electron reaction along the parallel direction, and on the $\mathbf{E}\times\mathbf{B}$ perpendicular motion of the ions. If any of them is perturbed, the drift wave can become unstable and yield net radial turbulent transport. Right: Linear growth rate γ as a function of the perpendicular wavenumber k_y for the three main types of drift-wave instabilities. Normalization parameters are the speed of sound $c_s = \sqrt{T_e/m_i}$ with T_e the electron temperature and m_i the mass of the ions, the major radius R and the ion Larmor radius ρ_i [48].

Ion temperature gradient mode (ITG)

The ITG mode is the drift-wave instability that is believed to be responsible for the majority of ion heat transport in toroidal fusion plasmas [49, 50]. The ITG mode is a purely toroidal mode that can become unstable when a temperature gradient exists that is parallel to the magnetic field amplitude gradient. This phenomenon is typical in the outer part of the toroidal device, where the magnetic field is lower (bad-curvature region). The right frame in Fig. 1.9 illustrates this mechanism. Given a temperature fluctuation, the presence of a gradient of the magnetic field amplitude ∇B results in a separation of charges with different signs. This charge separation creates an electric field and the associated $\mathbf{E}\times\mathbf{B}$-drift. The drift, in this case, amplifies the propagation of the perturbation increasing its magnitude and turning it unstable. In the inner part of the torus occurs just the contrary (left frame of the figure 1.9).

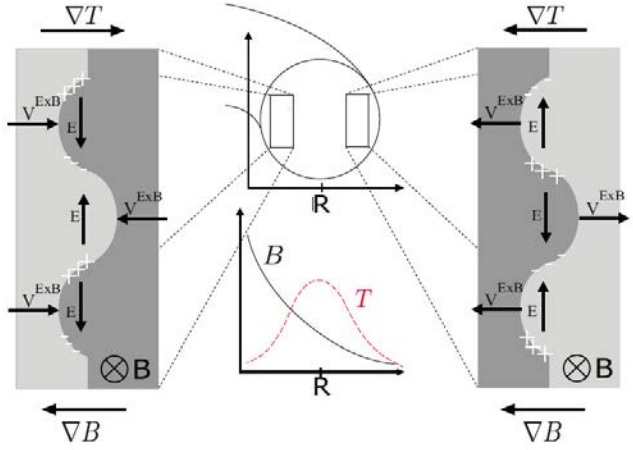

Figure 1.9: The Ion temperature gradient mode instability in a good-curvature region (left) and in a bad-curvature region (right). In the first case, the gradient of the magnetic field amplitude ∇B and the temperature ∇T are in opposite directions. In this case the emergent $\mathbf{E}\times\mathbf{B}$-drift mitigates the perturbation. In the second case, ∇B and ∇T are parallel and the $\mathbf{E}\times\mathbf{B}$-drift amplifies the perturbation [48].

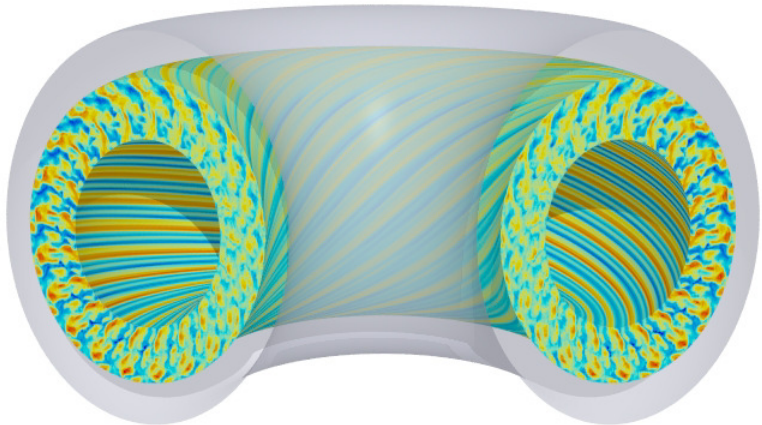

Figure 1.10: Gyrokinetic simulation performed with GENE code for the ITG mode in a Tokamak. Negative fluctuations are in blue and positive fluctuations in red [48].

The temperature gradient is opposite to the magnetic field amplitude gradient (good-curvature region). In the inner part of the configu-

ration, charge separation produces an $\mathbf{E}\times\mathbf{B}$-drift which reduces the initial temperature perturbation amplitude and stabilizes the perturbation. As a consequence, fluctuations at the bad-curvature region (unstable) will be larger than the fluctuations of the good-curvature region (stable). This result is reproduced routinely in current gyrokinetic simulations of ITG turbulence (see Fig. 1.10). It is also clear that structures are elongated along the field lines, the parallel direction, thus connecting the bad and good curvature regions, which facilitates the stabilization process.

Electron temperature gradient mode (ETG)

The instability known as the ETG mode is similar to the ITG, but with the electrons playing the role of the ions[51, 52]. The importance of its role in explaining electron heat transport is still a matter of active investigation. ETGs simulations are more complicated, though, because of the much smaller length scales that must be resolved, due to the different mass of ions and electrons.

Trapped electron mode (TEM)

It is also believed that trapped electron drift-wave instabilities play a role in both heat and particle transport in toroidal fusion plasmas [53, 54]. Parallel electron motion is impeded by the trapping of a fraction of the electron population due to the inhomogeneous magnetic field, which may drive drift waves unstable. Trapping also concentrates electrons in the bad curvature region, which enhances the instability.

1.6 Non-diffusive transport in magnetically confined, fusion toroidal plasmas

As it has already been mentioned in the previous section, most studies of turbulence and turbulent transport in fusion plasmas have had the final goal of capturing the overall effect of turbulence within some kind of effective transport coefficients of the diffusive type. In the last three decades, however, there has been a growing body of work that has shown that this type of description may be inadequate in some cases [1, 2, 3]. In particular, this might be the case of several regimes of relevance to confined plasmas such as near-marginal turbulence [2, 3] and transport

across radially-sheared poloidal flows [5]. We will discuss these two situations separately in this section, but it suffices to say at this point that ITER will be probably operated in a regime in which near-marginal conditions are expected, and that relies in radially-sheared poloidal flows to provide access to enhanced confinement regimes [31]. These observations make relevant any study that attempts to move the description of turbulent transport beyond the usual diffusive framework, searching for better models that could capture the underlying dynamics more properly. The work contained in this thesis must be looked at in this light in order to be properly understood.

1.6.1 Non-diffusive or fractional transport

The classical formulation of the Fick's law (i.e., Eq. 1.11) relies on the implicit assumption of an underlying locality in space and a lack of memory in time. That is, the flux at any given location is only a function of the value of fields (mostly, the gradient of the transported quantity) at the same location and at the same time. This locality in space and time is ultimately associated to the existence of well-defined characteristic scales for transport, both in time and in space. If these conditions are met, the local, memory-less approach behind Fick's law applies, at least when transport is considered at times and distances much longer and larger than the characteristic ones [55].

There are however cases in which characteristic scales for transport cannot be found due to the nature of the underlying process [1, 56, 57]. One such example is when transport is driven by avalanches whose size is only limited by the system size, and whose excitation heavily depends on the previous avalanching activity in the system. A non-fusion-related example of such a system is provided by earthquake dynamics [58], where the energy released is heavily conditioned by the size of previous earthquakes which, at the same time, also condition where the next tectonic relaxation will take place. In turbulent plasmas, a similar situation can happen in cases in which the plasma profiles are close to the local threshold values for the excitation of the different instabilities that drive transport [2, 3]. Other examples can be found in plasmas, particularly referred to transport in regions where magnetic stochastic fields are present [59, 60].

In any of these cases, any diffusive description of transport based on Fick's law will fail to capture the underlying dynamics [56]. One must

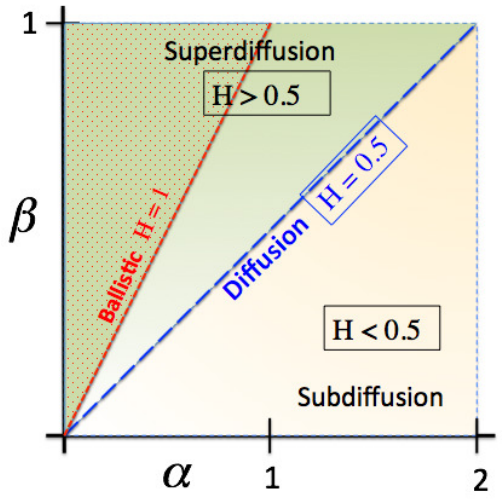

Figure 1.11: Transport behaviours captured by the fractional transport equation (Eq. 1.17) depending on the value of α, H and $\beta = \alpha H$.

thus move to more complicated mathematical frameworks. In particular, there are physical considerations that suggest to use instead transport equations that are based on fractional differential operators ($D_t^\beta, \partial^\alpha/\partial|x|^\alpha$) [61, 62] (see *Appendix B: Introduction to fractional derivatives and integrals*; see also the discussion around Eq. 3.6) such as [56]:

$$\frac{\partial n}{\partial t} = D_t^{1-\alpha H}\left[D_0 \frac{\partial^\alpha n}{\partial |x|^\alpha}\right] \tag{1.17}$$

where D_0 is a constant (in general, it is not diffusivity!), $\alpha \in (0, 2]$ is the spatial exponent and $H \in (0, \max(1, 1/\alpha)]$ is known as the Hurst exponent. Often, another exponent is introduced, defined as $\beta \equiv \alpha H \in (0, 1]$ that is known as the temporal exponent.

The actual values of these fractional exponents determine the nature of transport that the solution of the fractional transport equation will exhibit (see Fig. 1.11). For example, if $\alpha = 2$ the spatial transport dynamics are local. Fluxes at any given point depend only on the value of the gradients at the same location. If $\alpha < 2$, however, spatial transport is not local, and fluxes depend on values of the gradients at other locations as well. Similarly, if $\beta = 1$ (or, equivalently, if $H = 1/\alpha$) transport throughout the system lacks any memory effects. That is, fluxes only

depend on the values of the gradients at that same time. On the contrary, if $\beta < 1$, memory becomes important. In fact, the past history of the system becomes more relevant the smaller β becomes, since events further back in time will contribute more heavily to the evaluation of the fractional derivative at the current time. Clearly, for $\alpha = 2$ and $\beta = 1$ (i.e., $H = 1/2$), classical diffusive behaviour is recovered.

The Hurst exponent characterizes the nature of the transport captured by Eq. 1.17, whose range of dynamics is illustrated in Fig. 1.11. If $H = 1/2$ transport is called *diffusive*. The reason is that any initially-localised perturbation that advances in time according to classical diffusion spreads in time at a rate proportional to $t^{1/2}$ [55]. If the same perturbation is advanced instead according to the fractional transport equation, Eq. 1.17, it can be proved that it would spread out as t^H [56, 1]. Thus, $H = 1/2$ is referred to as a *diffusive* scaling, although it could be that the nature of transport is not diffusive in a classical sense, since H can still be $1/2$ for $\alpha \neq 2$ and $\beta \neq 1$, which means that transport is still non-local and dominated by memory effects. It is also customary to describe transport as *subdiffusive* if $H < 1/2$, and *superdiffusive* if $H > 1/2$. The reason is simple. The perturbation will spread out slower or faster than a perturbation spreading diffusively would.

1.6.2 Near-marginal turbulent transport

There are many experimental evidences that suggest that non-diffusive transport behaviour dominates radial turbulent transport in various regimes relevant to toroidal fusion plasmas (see Ref. [1] for a review). For example, it is believed that L-mode tokamak plasmas (and maybe the part of the plasma inside the edge pedestal in H-mode regimes) are in a state of near-marginal turbulence across most of the radius, that results in an effectively non-diffusive radial transport that is dominated by avalanches [63] and that exhibits long-term memory [64, 65, 66]. A near-marginal situation means that plasma profiles (such as pressure, temperature, etc.) wander around the local instability threshold which leads to the local excitation of turbulence. When the local threshold is exceeded at a certain location, turbulence appears and drives local transport to flatten the local gradient that drove it unstable. In the process, heat or particles (or both) are transported to neighbouring locations, whose local gradients then increase and that can become themselves unstable. Therefore, the whole

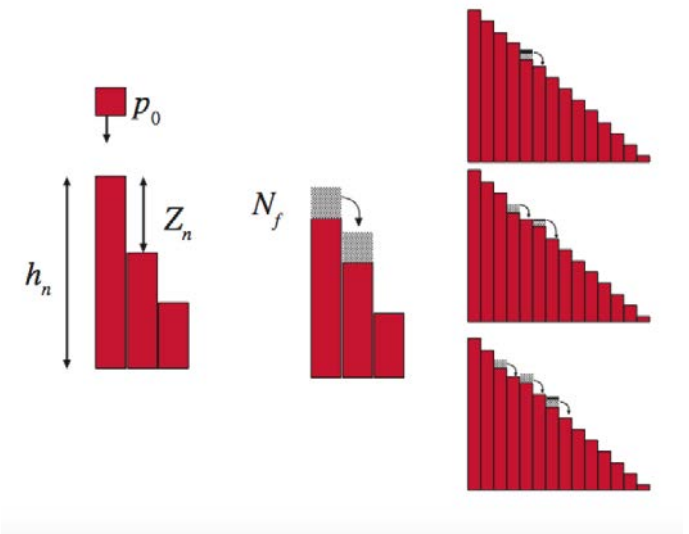

Figure 1.12: Sketch of a sandpile model and its avalanche process. Z_n represents the difference between the level of sand of two contiguous cells. A virtual perturbation of sand, in grey, shows the avalanche process.

process repeats itself again, with heat or particles being transported down the gradient and the perturbation in the profile propagating in avalanche-like form.

This behaviour is very reminiscent of one of the most studied models used to explain the Self-Organized Criticality (SOC) [67]: the sandpile model (see Fig. 1.12) [68]. In this analogy, the cells and the sand of the sandpile will respectively be the different radial positions of the device and the physical variable that drives the turbulence (temperature, density or pressure) [3]. There are certain situations, when most of the cells are very close to the threshold level of sand, where a small perturbation could induce a large cascade or avalanche, whose size is only limited by the sandpile size. Those regimes are usually referred to, as pointed out before, as *near-marginal* situations. In the presence of an external drive, if it is not too strong, the sandpile will always be pushed to stay close to a near-marginal regime. Similarly, some simulations suggest that the larger temperatures in ITER will be able to drive fluxes that will continuously push density/temperature profiles as to keep them close to near-marginal values across most of the tokamak (see Ref. [1] for a review).

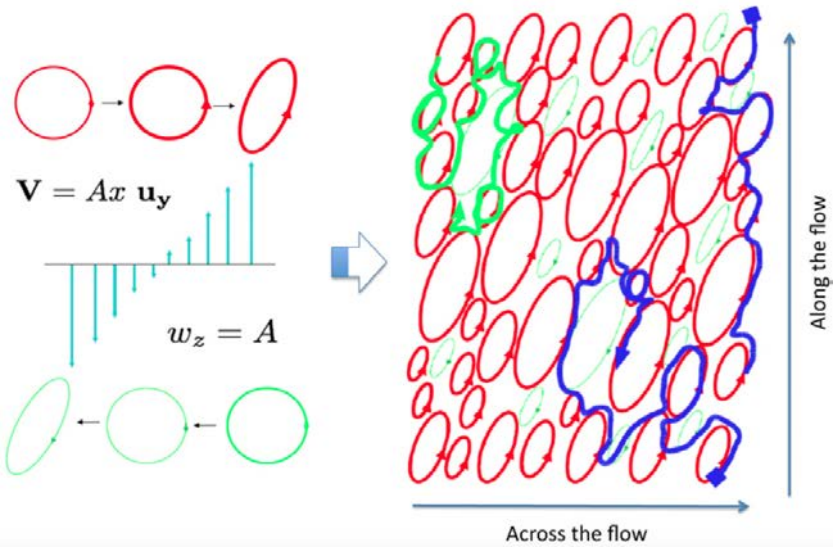

Figure 1.13: On the left, the eddy's deformation due to the stretching-elongation process created by the sheared zonal flow along the y direction (the vorticity of the eddies is in the z direction). On the right, there are three different trajectories over the turbulent map of distorted eddies. The intensity of the eddies is used to express the favoured or unfavoured eddies.

In the sandpile model, the positions where the avalanche is started have a lower probability of starting another avalanche in the next instants because their levels of *"sand"* are far from the threshold. On the contrary, the positions where the avalanche died have a larger probability of starting new avalanches in the following instants, because their levels of *sand* are probably very close to threshold. This is the mechanism through which memory is established in the system [68].

1.6.3 Sheared zonal flows and turbulent transport

There are other regimes relevant to fusion plasmas, apart from near-marginal conditions, where radial transport could behave non-diffusively. In particular, in the last decades, the turbulent radial transport across strong radially-sheared, poloidal zonal-flows has become one of the most important topics in fusion plasmas because these flows reduce radial losses and increase the confinement time by permitting the transition to enhance

confinement regimes such as the H-mode [11, 69]. There is evidence, however, that supports that these flows not only reduce radial turbulent transport, but that they could also alter the intrinsic nature of radial transport itself. Recent numerical studies do suggest that the effects of these radially-sheared poloidal zonal flows exceed the mere reduction of the radial transport of particles or heat, changing the nature of the radial transport itself, that becomes subdiffusive [5, 6].

To understand the physical mechanism that leads to subdiffusive radial transport across sheared flows [7], it is useful to consider the sketch shown in Fig. 1.13. There, the action of a sheared flow on a single eddy is illustrated. The sheared flow acts differently on eddies with different sign of vorticity. Vorticity is related to local rotation. In the case in which the vorticity is of the same sign as that associated to the shear flow, the eddy is distorted (i.e., its radial length reduced!) but its own vorticity (i.e., its local angular velocity) is enhanced at the same time. On the other hand, the vorticity inside eddies with a vorticity of different sign than that of the flow are weakened, and even eliminated. The results of this process are sketched in the right frame of the same figure: a vorticity landscape in which the sign determined by the shear flow dominates. If one now envisions how a particle, trapped in this vorticity field, advances perpendicularly to the flow, it is easy to see that every time the particle leaves an eddy it will be kicked back in the same direction that it came from. That is the essence of what subdiffusion is about.

It is clear that any effective description built in terms of effective diffusive coefficients will fail to capture the dynamics of the type of subdiffusive transport across sheared flows just discussed. Again, one would need to use fractional transport equations of the type of Eq. 1.17, with exponents with values chosen adequately in order to reproduce the underlying subdiffusive dynamics.

Chapter 2

Gyrokinetic simulations of turbulence in quasi-poloidally symmetric configurations

The physical processes that take place in magnetically confined fusion plasmas span a very wide range of scales. The ranges are so large – about 12 orders of magnitude in time, about 8 in space – that it is impossible to build a single code capable of simulating all these physical processes. For example, the spatial scales in these plasmas extend from the submillimeter range of the electron gyroradius to the several meters of correlations lengths along a magnetic field line. In the case of temporal scales, very fast dynamics such as the electron Larmor gyration ($\sim 10^{10}$Hz) coexist with much slower ones such as the energy confinement time, of the order of tens, even hundreds of seconds.

In the case of turbulent transport in tokamak and stellarator plasmas, turbulence is governed by instabilities with growth rates of the order of micro to a few milliseconds, but that can in some cases sustain strong correlations for much longer periods of time. Turbulence-induced modification of the plasma profiles takes place, however, in timescales of the order of hundreds of milliseconds or longer. It has been long believed that turbulent scales can be modelled, in these plasmas, by averaging out the faster scales (such as gyro-motion) and by assuming that the slower scales (i.e., profile modifications) remain basically unchanged during the amount of time that turbulence is simulated. Simulations done under these conditions are then routinely used to estimate effective transport

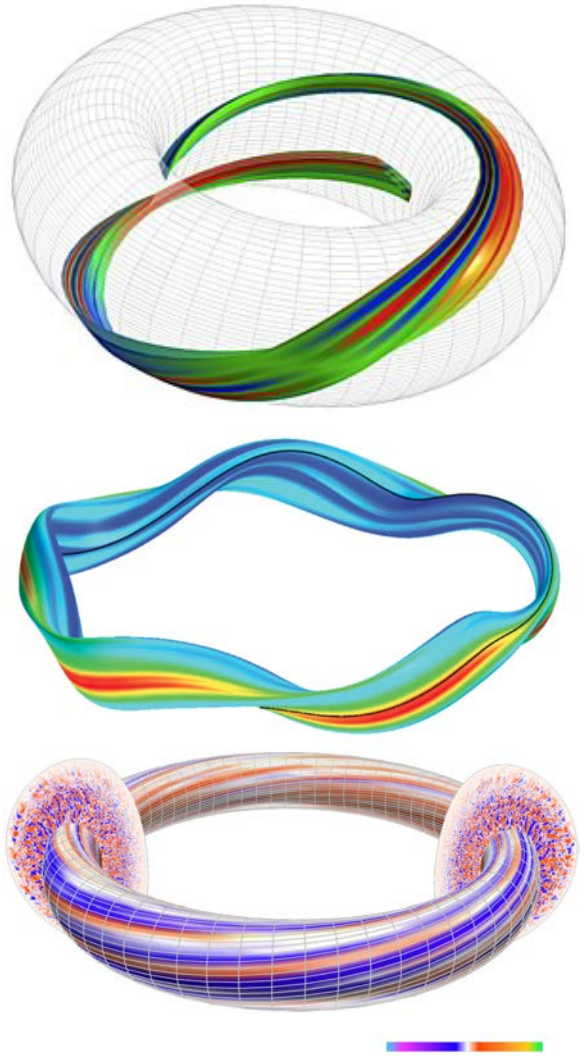

Figure 2.1: Examples of different domains for gyrokinetic simulations: tokamak flux-tube simulation (top); full-annulus simulation for W7-X [74] (middle); tokamak global simulation [75] (bottom).

coefficients. Although there are situations in which the latter assumption may fail (see, for instance, the discussion on near-marginal turbulence held at the end of Chapter 2), we will assume that this approximation is valid in this work.

In the conditions previously mentioned, the so-called *gyrokinetic* description is adequate [70, 71]. The gyrokinetic model describes the evo-

lution of each plasma species using kinetic equations averaged over the fast gyromotion around the magnetic field lines. Thus, the resulting equations describe the time evolution of the distribution function of each particle guiding centre. This averaging, together with some further simplifications (namely, the assumption of small fluctuations and strong anisotropy in the direction parallel to the magnetic field), reduces the high complexity of the full kinetic equations making them amenable of numerical solution [72].

Gyrokinetic codes are usually classified into two different types: *full-f* and δf. In the first case, the code considers the evolution of the full distribution function. In contrast, δf codes only evolve in time the deviation from a background Maxwellian distribution function, F_0. It is F_0 that contains all information about the radial profiles for plasma density, temperature, pressure or velocity, that remains constant. The fluctuating part of the distribution function, δf, is considered small compared to the stationary background part of the function F_0, which permits further simplifications.

Attending to the simulation domain, gyrokinetic codes are usually classified as *local* or *global*. On one hand, local codes simulate a very reduced portion of the plasma, usually a *flux-tube*. That is, a small domain that follows the magnetic field (see upper frame in Fig. 2.1). Flux-tube simulations usually assume periodic boundary conditions in all directions. Since the radial extension is minimal, being localised around some given magnetic surface, all background radial profiles (i.e., pressure, temperature, etc.) are represented by a single value that corresponds to the one of the profile at that magnetic surface. There are also local codes that consider instead the radial neighbourhood of a complete magnetic flux-surface. We will refer to these type of domains as *full-annulus* or *flux-surface*. In full-annulus simulations, all background quantities of interest, except for the magnetic field and its derivatives, are still represented by their (single) value at the magnetic surface. This means that most of them use the δf-approach. The magnetic field, however, does vary along the surface, although it is still considered to be independent of radius.

On the other hand, global codes consider the complete toroidal domain. All plasma quantities of interest are no longer assumed constant in radius, having instead a radial profile. Global codes may evolve or not the plasma background radial profiles. In the first case, that is known as a *flux-driven* setup, the average fluxes (of particles, heat, etc.) in steady-

state are set by introducing sources and sinks. Plasma profiles are then allow to vary to accommodate these fluxes. Clearly, in order to simulate a plasma in a flux-driven setup, full-f, global codes are required. On the other hand, *fixed-gradient* setups assume fixed background radial profiles that do not evolve with time. In this case, global gyrokinetic codes can also be run as δf codes, assuming that the time of the simulation is short enough so that δf remains small.

Finally, gyrokinetic codes can also be distinguished by the numerical approach used to solve the gyrokinetic equations. There are two main classes: *Eulerian* and *Lagrangian* (or PIC[1]) codes. Eulerian codes consider an Eulerian mesh with fixed nodes in gyrokinetic phase space. All variables and fields are evaluated at the nodes of the mesh. On the other hand, Lagrangian codes combine Eulerian and Lagrangian descriptions. The distribution function of all species is constructed by means of marker particles (gyro-averaged ions, and sometimes also electrons), that are advected in the presence of magnetic and electric fields. These fields, on the other hand, are advanced in time on a Eulerian mesh (if only the electric field varies in time, the code is known as *electrostatic*; if both the magnetic and the electric field are updated, as *electromagnetic*). A lot of information must thus be transferred between the Lagrangian and Eulerian representations by PIC codes. Each method has its advantages and disadvantages. PIC codes, on the one hand, are easier to parallelize, but are subject to particle noise. Eulerian codes, on the other hand, must use sophisticated methods such as domain decomposition to be run in parallel supercomputers, which makes them significantly more complex.

In this thesis, we will use the GENE gyrokinetic code [12, 73]. GENE is a well-established gyrokinetic code with a degree of sophistication close to the state-of-the-art in the subject. GENE is an Eulerian (Vlasov) code that can be run in general three-dimensional magnetic geometries. This is specially convenient for the study of turbulent transport in quasi-poloidally symmetric configurations that we carry out in this work (in fact, there are not many other codes of this kind than can deal with complex 3D geometries). GENE is also a δf code, which means that no evolution of plasma profiles can be done with it at the moment. Finally, we will always run GENE using a full-annulus setup and assuming electrostatic, ITG-dominated turbulence.

In this chapter we will first provide a brief description of GENE

[1] **P**article-**I**n-**C**ell

although we will not go into all the details, referring instead those interested readers to its reference manual [73]. Then, we will describe and discuss the turbulent simulations that we have carried out with GENE on the configuration of a quasi-poloidally symmetric stellarator that we will use to study the effect on turbulent transport of quasi-symmetries in the remainder of the thesis. In particular, we will characterize the main features of these quasi-poloidal configurations and describe the main characteristics of the turbulence and the turbulent transport obtained with GENE for them.

2.1 The GENE gyrokinetic code

GENE [2] is a code that has been developed for almost twenty-five years by a team of computer scientists and plasma physicists led by Prof. Frank Jenko at the Max Planck Institut für Plasmaphysik (Garching, Germany) [12, 48, 73, 76, 77, 78, 79, 80, 81, 82] . It is freely available and frequently updated and expanded. It is one of the gyrokinetic codes more widely used at the moment.

GENE solves the gyrokinetic-Maxwell system of equations using an Eulerian-Vlasov, local, δf approach on a fixed grid in a 5-dimensional phase space. Three of these dimensions are field-aligned spatial coordinates (x, y, z) and the other two are velocity coordinates $(v_\parallel, \mu)$, that correspond to the parallel component of the velocity with respect to the background magnetic field $v_\parallel$, and to the magnetic moment $\mu = mv_\perp^2/2B$. GENE was originally a tokamak flux-tube code that has been extended over the years and that is currently capable of carrying out full-annulus calculations in the neighbourhood of fully three-dimensional magnetic surfaces (such as those of a stellarator). Although GENE can be run in both electrostatic and electromagnetic modes, we will restrict our studies to electrostatic runs in which only the electrostatic potential is evolved in time. In addition, GENE can advance in time both ions and electrons, but we will however work under the assumption of adiabatic electrons, so that only the equation for the δf part of the ion distribution function is solved.

[2] **G**yrokinetic **E**lectromagnetic **N**umerical **C**ode

2.1.1 Gyrokinetic δf equation

The ion electrostatic gyrokinetic equation that GENE will solve for us, in this thesis, can be expressed as:

$$\frac{df_i}{dt} = \frac{\partial f_i}{\partial t} + \dot{\mathbf{X}} \cdot \frac{\partial f_i}{\partial \mathbf{X}} + \dot{v_\parallel} \frac{\partial f_i}{\partial v_\parallel} + \dot{\mu} \frac{\partial f_i}{\partial \mu} = 0 \tag{2.1}$$

where $\mathbf{X} = (x, y, z)$ represents the spatial position vector. The distribution function is expressed as $f_i = F_i^0 + \delta f_i$, with the Maxwellian

$$F_i^0 = \frac{n_i^0}{(\pi T_i^0)^{3/2}} \exp\left(-(v_\parallel^2 + \mu B_0)/T_i^0\right), \tag{2.2}$$

that contains all background profile information, that is kept fixed. At the lowest order in $\epsilon \sim \delta f / F^0$, the associated velocities are given by the expressions [73]:

$$\dot{\mathbf{X}} = v_\parallel \mathbf{b_0} + \frac{B_0}{B_{0\parallel}^*}(\mathbf{v_E} + \mathbf{v_{\nabla B}} + \mathbf{v_c}), \tag{2.3}$$

$$\dot{v_\parallel} = -\frac{1}{m_i v_\parallel} \dot{\mathbf{X}}(q_i \nabla \tilde{\Phi} + \mu \nabla B_0), \tag{2.4}$$

$$\dot{\mu} = 0. \tag{2.5}$$

In these expressions, several quantities appear. First, $\mathbf{v_E}$ is the $\mathbf{E}\times\mathbf{B}$-drift velocity ($\mathbf{B}_0$ is the background magnetic field),

$$\mathbf{v_E} = -\frac{\nabla \tilde{\Phi} \times \mathbf{B_0}}{B_0^2}, \tag{2.6}$$

through which the turbulent electric fields (i.e., $\tilde{\mathbf{E}} = -\nabla \tilde{\Phi}$) affect the ion motion. Secondly, $\mathbf{v_{\nabla B}}$ is the magnetic drift velocity:

$$\mathbf{v_{\nabla B}} = \frac{\mu}{m_i \Omega_i B_0} \mathbf{B_0} \times \nabla B_0, \tag{2.7}$$

where $\Omega_i = q_i B_0 / m_i$ is the ion gyrofrequency. Finally, v_c is the curvature drift velocity, defined as,

$$\mathbf{v_c} = \frac{v_\parallel^2}{\Omega_i} (\nabla \times \mathbf{b_0})_\perp = \frac{\mu_0 v_\parallel^2}{\Omega_i B_0^2} \mathbf{b_0} \times \nabla \left(p_0 + \frac{B_0^2}{2\mu_0} \right), \tag{2.8}$$

where the MHD force balance equation, $\nabla p_0 = \mathbf{J_0} \times \mathbf{B_0}$, and Ampere's law, $\nabla \times \mathbf{B_0} = \mu_0 \mathbf{J_0}$, have been used. Also, $\mathbf{b}_0 = \mathbf{B}_0/B_0$ is the unit vector parallel to the magnetic field. The effective magnetic field, $\mathbf{B_0^*}$, is defined as

$$\mathbf{B_0^*} = \mathbf{B_0} + \frac{m_i}{q_i} v_\parallel \nabla \times \mathbf{b_0}. \tag{2.9}$$

On the other hand, it is worth noting that the equation $\dot{\mu} = 0$ is a consequence of the gyro-averaging that leads to the gyrokinetic equation. In fact, the magnetic moment μ is the conserved quantity associated to the independence on the gyro-phase that follows from the procedure [70].

2.1.2 Gyro-averaged Poisson equation

In addition to the ion gyrokinetic equation, GENE must also solve a (gyro-averaged) Poisson equation to get the turbulent electrostatic potential. This equation is simply the gyro-average of:

$$-\nabla^2 \tilde{\Phi} = 4\pi \sum_j q_j \tilde{n}_j. \tag{2.10}$$

The expression of the equation, in GENE coordinates, that is solved to find the potential is rather involved. The expression, that approximates Poisson's equation via the quasi-neutrality equation, can be found in the literature [73]. It is worth noting that, in the approximation of adiabatic electrons that we will use in this work, only the ion fluctuating density is obtained by integration of the solution of Eq. 2.1, whilst the fluctuating electron density is given by:

$$\tilde{n}_e \simeq \frac{e n_e^0}{T_e^0} \left(\tilde{\Phi} - < \tilde{\Phi} > \right), \tag{2.11}$$

where the brackets stand for flux-surface averaging.

2.1.3 Geometry and coordinate system

GENE is very efficient thanks to the use of a field aligned coordinate system. The starting point is provided by the magnetic equilibrium information, which is usually expressed in Boozer coordinates.

Boozer coordinates

Boozer coordinates form a particularly useful system of flux coordinates to describe toroidal fields [39]. It is composed of a radial coordinate $s_B \in [0,1]$ that identifies the magnetic surface (usually $s_B := \psi/\psi_{\text{edge}}$, with ψ being the toroidal magnetic flux through that magnetic surface, as it is illustrated in the left frame of Fig. 2.2; we will always assume this choice in what follows), and two angle-like coordinates, θ_B and ϕ_B that go around the magnetic surface with a period of 2π. These angles do not usually coincide with the geometric poloidal and toroidal angles, though.

Many flux coordinate systems exist. The importance of the Boozer one comes from the fact that, when expressed in Boozer coordinates, all magnetic field lines (and also current lines) become straight [39]. A magnetic field line in Boozer coordinates is defined as $\alpha := \theta_B + \iota(s_B)\phi_B = \alpha_0$, where $\iota(s_B)$ is the rotational transform (see Eq. 1.8) and α_0 is a constant. α is known as a line label. For this reason, it is very convenient to describe the equilibrium and stability properties of general magnetic configurations in Boozer coordinates. It is also the system in which any quasi-symmetry that might be hidden in a configuration can be made explicit. The reason is because, in fact, quasi-symmetries are defined as the symmetries of B when expressed in Boozer coordinates [37, 39].

The magnetic field of any three-dimensional configuration, in Boozer coordinates, has two representations. First, the *contravariant* one given by:

$$\mathbf{B} = B^{\theta}\mathbf{e}_{\theta_\mathbf{B}} + B^{\phi}\mathbf{e}_{\phi_\mathbf{B}}. \tag{2.12}$$

Here, the covariant basis vectors are defined as $\mathbf{e}_\xi := \partial\mathbf{r}/\partial\xi$ (with $\xi = s_B, \theta_B$ or ϕ_B), being the vector associated to any coordinate tangent to the intersection of the isosurfaces of the other two coordinates. It is worth noting that $B^{s_B} = 0$ since $s_B = s_0$ is a magnetic surface for any s_0, and the field must be tangent to it. The contravariant components are themselves given by [39]:

$$B^{s_B} = \frac{\psi_{\text{edge}}}{2\pi\sqrt{g_B}}, \qquad B^{\theta_B} = \frac{\psi_{\text{edge}}}{2\pi\sqrt{g_B}}\iota(s_B), \tag{2.13}$$

where $\iota(s_B)$ is the rotational transform, and $\sqrt{g_B}$ is the jacobian of the transformation to Boozer coordinates, that must be found numerically. The rotational transform, that gives the pitch of the magnetic field at each

magnetic surface (see Eq. 1.8), becomes $\iota(s_B) = B^{\theta_B}/B^{\phi_B}$. Its inverse, $q(s_B) = 1/\iota(s_B)$ is the *safety factor*.

There is also a *covariant* representation of the magnetic field in Boozer coordinates. It is given by:

$$\mathbf{B} = B_{s_B}\mathbf{e}^{\mathbf{s_B}} + B_{\phi_B}\mathbf{e}^{\phi_\mathbf{B}} + B_{\theta_B}\mathbf{e}^{\theta_\mathbf{B}} \tag{2.14}$$

Here, the contravariant basis vectors are defined as $\mathbf{e}^{\xi} := \nabla\xi$ (with $\xi = s_B, \theta_B$ or ϕ_B), being each one perpendicular to the $\xi = \xi_0$ surface. The covariant components of the magnetic field are then given by [39]:

$$B_{\theta_B} = \frac{I_{pol}(s_B)}{2\pi}, \quad B_{\phi_B} = \frac{I_{tor}(s_B)}{2\pi}, \tag{2.15}$$

with I_{tor} and I_{pol} the toroidal and poloidal currents flowing inside the magnetic surface s_B. The other component, B_{s_B} is a double periodic function (in θ_B and ϕ_B) with zero surface average, that depends on the configuration at hand, and that must be found numerically in each case.

Gene coordinates

The field-aligned system of coordinates used by GENE (x, y, z) takes advantage of the fact that turbulence varies very differently along the magnetic field lines in comparison to perpendicularly to them. Thus, GENE tries to define a coordinate z that runs along the local magnetic field, in which the resolution required to properly represent the turbulence is decoupled from that needed in other directions, thus greatly enhancing numerical efficiency. For flux-tube and full-annulus runs, the local GENE coordinates are defined around a selected magnetic surface $s_B = s_0$. The expression of GENE internal coordinates, in terms of the Boozer Coordinates that define the magnetic field of the configuration, is (see also right frame of Fig. 2.2) [73]:

$$x = \rho_{ref}(\sqrt{s_B} - \sqrt{s_0}), \quad y = C_y\left[q(x)\theta_B - \phi_B\right], \quad z = \theta_B. \tag{2.16}$$

Here, $q(x)$ is the safety factor of the configuration. That is, the inverse of the rotational transform previously introduced, $q = 1/\iota$. In the local representation, it is assumed to be given by $q(x) = q_0 + q_0' x$ with $q_0 = q(s_0)$. C_y and ρ_{ref}, on the other hand, are normalization constants of GENE [73] (explained in more detail later in this section).

The field-aligned character of these choices comes from the fact that, if z is varied while keeping x and y fixed, one just moves along a single magnetic line (at least approximately, as we will explain later). The value of x gives the radial distance to the reference magnetic surface. On the other hand, the value of y fixes on a specific magnetic field line. This is made apparent by looking at the contravariant expression of the magnetic field in GENE coordinates, that is:

$$\mathbf{B} = C(x)\nabla x \times \nabla y = \frac{C(x)}{\sqrt{g_B}}\mathbf{e_z}, \tag{2.17}$$

with $C(x) = C_y\sqrt{g_B}B_{\theta_B}$. Clearly, the magnetic field is parallel to the unit covariant vector associated to the z coordinate, as advertised.

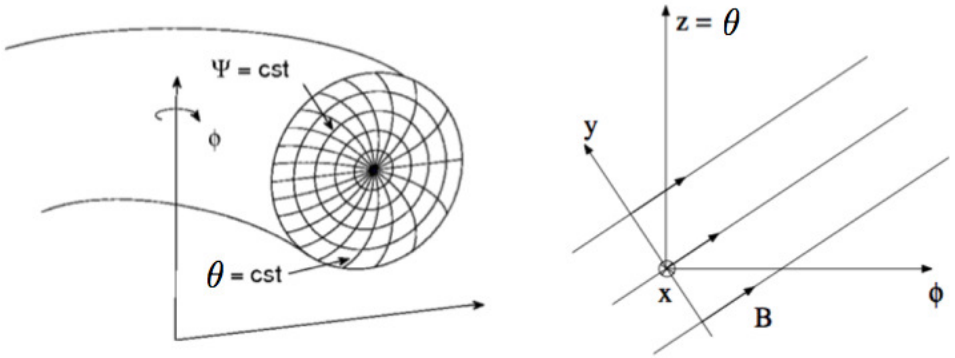

Figure 2.2: **Left:** Parametric surfaces in Boozer coordinates with the definition of fluxes. **Right:** Relation between Boozer and GENE angular coordinates and the magnetic field lines.

The numerical domain of GENE is defined by the intervals $x \in [-L_x/2, L_x/2]$, $y \in [0, L_y]$ and $z \in [-\pi, \pi]$. GENE estimates L_x in order to have a box large enough to include all relevant physics. It is often around $L_x \approx 100\rho^*$ with $\rho^* = \rho_{ref}/a$, ρ_{ref} being a longitude of reference and a the minor radius. L_y, is estimated in a similar way but considering instead the binormal direction. GENE also exploits the symmetry of the device and takes into account just one complete period of the machine (usually defined through the line label, $\alpha := q\theta_B - \phi_B \in [-\pi/n_0, \pi/n_0]$ where n_0 denotes the periodicity of the machine)

2.1.4 GIST interface

In stellarators, the VMEC equilibrium code [83] is the tool most commonly used to calculate the equilibrium magnetic field of stellarator configurations for a given plasma pressure profile. VMEC, however, uses its own internal flux coordinate system, that is different from the Boozer one just discussed. Thus, an additional interface called GIST [3] is used to calculate, transform and collect all the information necessary to run GENE in stellarator geometries [84]. GIST can also be used to transform equilibrium information for GENE from tokamak equilibrium codes, such as the EFIT equilibrium code [85]. In particular, GIST transforms all geometrical information to GENE internal coordinates, including the metric tensor and curvature coefficients. It also provides the derivatives of the magnetic field and many other quantities such as local pressure, safety factor, shear of the safety factor, etc.

2.1.5 Gene normalization

We conclude this introduction to GENE by clarifying some of its internal normalization. Normalization is often ignored while discussing physical results, since it is often (and rightly) considered a purely internal matter. In our case, however, we have needed this information to build the TRACER code, that will be used to advance tracer particles in the electrostatic turbulence that GENE computes, and that will be discussed at length in Chapter 4.

GENE uses a normalization based in either average or equilibrium values in order to deal only with dimensionless quantities and avoid any "extremal" values (very large or very small) while solving the gyrokinetic equation. The reference values of the plasma parameters are those at the magnetic axis of the configuration [48]. The axis values then define the reference mass, m_{ref}, the reference temperature, T_{ref}, the reference density, n_{ref}, or the reference magnetic field strength, B_{ref}. Internal variables used by GENE then are, for example:

$$\hat{m} = m/m_{ref}, \quad \hat{T} = T/T_{ref} \quad \hat{n} = n/n_{ref}, \quad \hat{B} = B/B_{ref}. \tag{2.18}$$

Variables with hat denote dimensionless variables. GENE then

[3] **G**yrokinetic **I**nterface for **S**tellarators and **T**okamaks.

uses these reference values to build other normalization factors used for other derived quantities. For instance,

$$c_{ref} = \sqrt{\frac{T_{ref}}{m_{ref}}}, \quad \Omega_{ref} = \frac{eB_{ref}}{m_{ref}c_{ref}}, \quad \rho_{ref} = \frac{c_{ref}}{\Omega_{ref}}, \tag{2.19}$$

$$p_{ref} = n_{ref}T_{ref}, \quad \Phi_{ref} = \frac{\rho_{ref}T_{ref}}{B_{ref}}. \tag{2.20}$$

Here, c_{ref} is the reference velocity value, ρ_{ref} the reference lengthscale, Φ_{ref} the reference electrostatic potential value and p_{ref} the reference pressure value.

The reference timescale that GENE uses is not provided by Ω_{ref}^{-1}, though. Instead, it is defined in terms of the macroscopic length of the system, L_{ref}, that is usually taken to be the major radius R_0 of the configuration. It is defined as:

$$t_{ref} = \frac{L_{ref}}{c_{ref}}. \tag{2.21}$$

Since the turbulent dynamics along and across the magnetic field are very different, GENE does not normalize its internal coordinates uniformly. Coordinates perpendicular to the magnetic field are normalized to ρ_{ref}. The parallel direction is not normalized, though. That is,

$$\hat{x} = x/\rho_{ref}, \quad \hat{y} = y/\rho_{ref}, \quad \hat{z} = z. \tag{2.22}$$

Regarding the velocity coordinates, they are normalized according to

$$v_\parallel = c_{ref}\hat{v}_T\hat{v}_\parallel, \quad \mu = \frac{T_{ref}}{B_{ref}}T_0\hat{\mu} \tag{2.23}$$

with the thermal velocity v_T defined as:

$$v_T = \sqrt{\frac{2T_0}{m}} = \sqrt{\frac{T_{ref}}{m_{ref}}}\hat{v}_T = c_{ref}\hat{v}_T \tag{2.24}$$

The Jacobian of the transformation to GENE internal coordinates is normalized to L_{ref}. The density and temperature gradients scale length, important since they set the instability threshold for the turbulence, are respectively normalized as,

$$\omega_T = -\frac{L_{ref}}{T}\frac{dT}{dx}, \quad \omega_n = -\frac{L_{ref}}{n}\frac{dn}{dx}. \tag{2.25}$$

2.2 The Quasi Poloidal Stellarator configuration: general properties

The studies carried out in this thesis to investigate the effects of quasi-symmetries on the nature of turbulent transport have been done using a quasi-poloidally symmetric configuration that is known as the QPS stellarator [38]. The QPS was to be a compact stellarator with low aspect ratio $A = R_0/a = 2.6 < 4$ (where R_0 and a are the major and minor radius respectively). It was to be built at the Oak Ridge National Laboratory (ORNL, Tennessee, U.S.A), but it was finally cancelled due to budget cuts by the US Department of Energy. QPS was a non-axisymmetric, fully three-dimensional device. But it was designed to be near poloidally quasi-symmetric.

For the present study, a two-period configuration has been selected that belongs to a set of cases explored during the design phase of the QPS project (see Fig. 2.3). We settled on this configuration because, as it will be shown soon, it exhibits a relatively strong variation of the degree of quasi-poloidal symmetry along the radial direction. The configuration corresponds to a two period machine and has an average $\beta = \langle 2\mu_0 p/B^2 \rangle \sim 2.5\%$. It has a toroidal current $I \sim 40kA$, which somewhat moves it away from traditional currentless stellarators, and a magnetic field with an amplitude on axis of $B_0 \simeq 0.9T$ (see Fig. 2.7). Endowing this configuration with quasi-poloidal symmetry does not come easy. A price must be paid in terms of the complexity of the coils needed to generate it. As can be seen, the coil set necessary for the magnetic configuration is very complicated and the shape of the plasma becomes very twisted, as illustrated in Fig. 2.3.

2.2.1 VMEC equilibrium solution

The equilibrium magnetic field for the QPS configuration used in this thesis has been calculated using the VMEC code [83]. Cross-sections at different toroidal angles of the set of magnetic surfaces provided by VMEC are shown in Fig. 2.6. VMEC is an spectral code that represents all quantities of interest (magnetic field, pressure, etc) as a double Fourier series in its internal poloidal and toroidal angles, with the magnitude of the harmonics being a function of the magnetic surface level. In the VMEC runs used to calculate the equilibrium for the case, poloidal modes

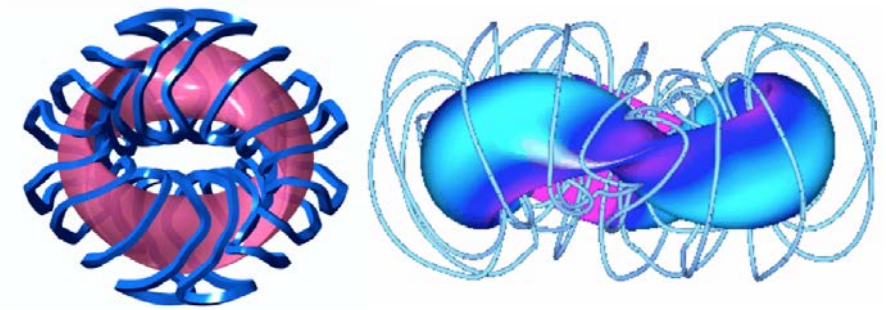

Figure 2.3: Stellarator QPS design. Set of twisted coils and the plasma shape. On the left, an upper point of view is shown (coils in blue and plasma in pink). On the right, a lateral view.

with wavenumbers running from $m = 0$ up to $m = M$, with $M = 8$ have been included. The toroidal modes used are labeled by $|n| \leq N$, with $N = 7$. Across magnetic surfaces, though, VMEC uses a finite-differences representation.

The safety factor of the configuration, $q(s) = 1/\iota(s)$, is shown in Fig. 2.4. As it will be remembered, the safety factor measures the pitch of the magnetic field. The larger q, the more toroidal turns the line undergoes per poloidal transit. For the QPS configuration, $q(s)$ is very large close to the magnetic axis, where $q(0) \sim 8$, and then decreases monotonously until an edge value of $q(a) \sim 4$. This dependence is very different from what is usual for tokamaks, where q increases with radius from an axis value satisfying $q(0) > 1$, for stability considerations [29]. The different dependence is due to the much larger plasma current that flows in a tokamak, of the order of several MAs, and that is responsible for most of the poloidal component of the field. The pressure and (surface-averaged) parallel current radial profiles are also shown in Fig. 2.5. The first one is rather standard. The second shows that most of the current , of the order of tens to hundreds of kAs, flows in the intermediate region, for $0.2 < s < 0.8$.

The four different cross-sections of the configuration nested magnetic surfaces shown in Fig. 2.6 at toroidal positions $\phi = 0, \pi/2, \pi, 3\pi/2$ demonstrate that the magnetic axis of the configuration is not located at a fixed R and Z value. Therefore, the configuration has a helical magnetic axis. It also shows that the shape of the plasma changes greatly with the toroidal angle, being thus fully three-dimensional, very different from the

situation in a tokamak. As a result, B is a function not just of the poloidal angle, as in tokamaks, but of the toroidal angle as well.

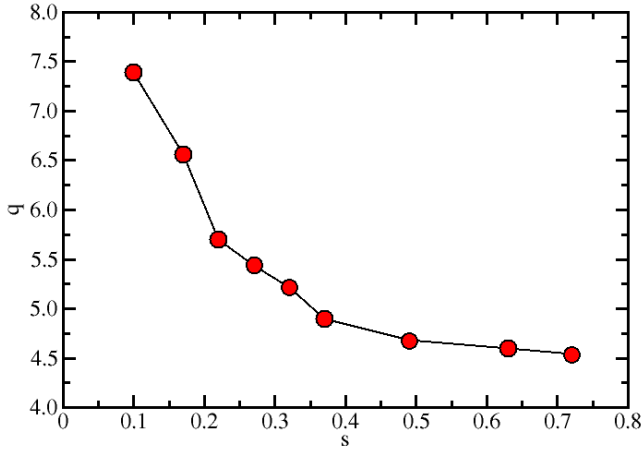

Figure 2.4: Safety factor q radial profile evaluated in the magnetic flux-surfaces of interest for the two-period QPS configuration used in the study.

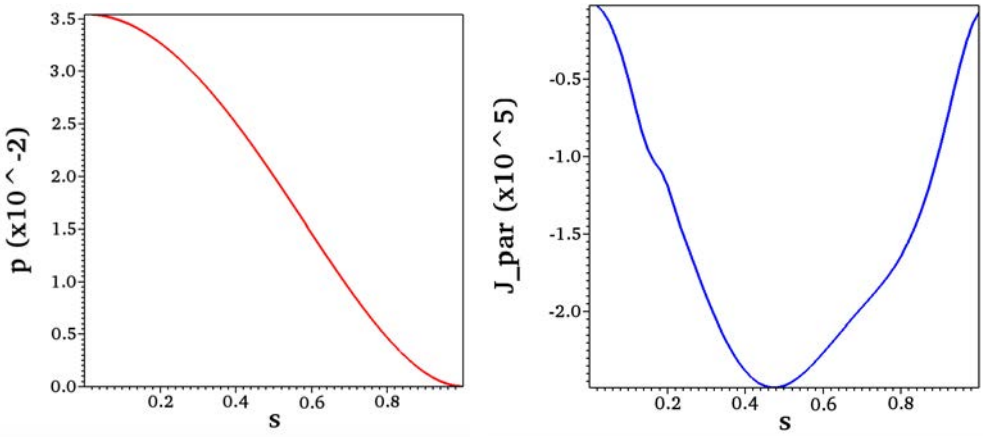

Figure 2.5: Pressure (left) and parallel current (right) radial profiles for the two-period QPS configuration used in the study.

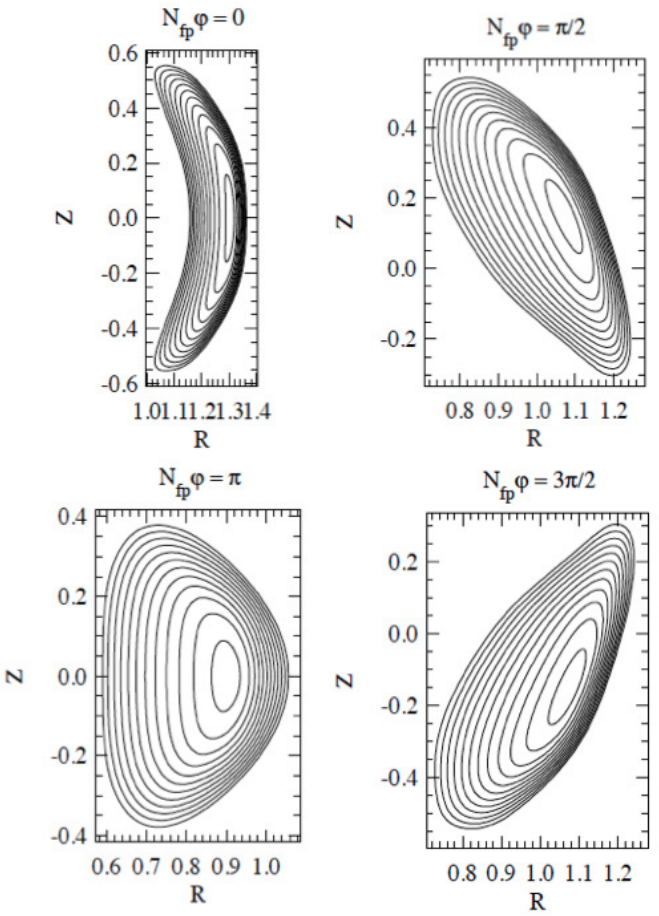

Figure 2.6: Cross-sections at four different toroidal angles of the set of equilibrium magnetic surfaces computed by VMEC for the quasi-poloidal configuration selected for the GENE simulations. $N_{fp} = 2$ is the number of periods.

2.2.2 Quasi-poloidal symmetry

Quasi-symmetries are, as we mentioned previously, symmetries of the magnitude of the magnetic field, B, when expressed in Boozer coordinates [37, 39]. Therefore, they are not always evident when represented in real space. In the case of the two-period QPS configuration analysed in this thesis, the level of quasi-poloidal symmetry is however sufficiently large as to be detectable by direct inspection even in cartesian coordinates. In-

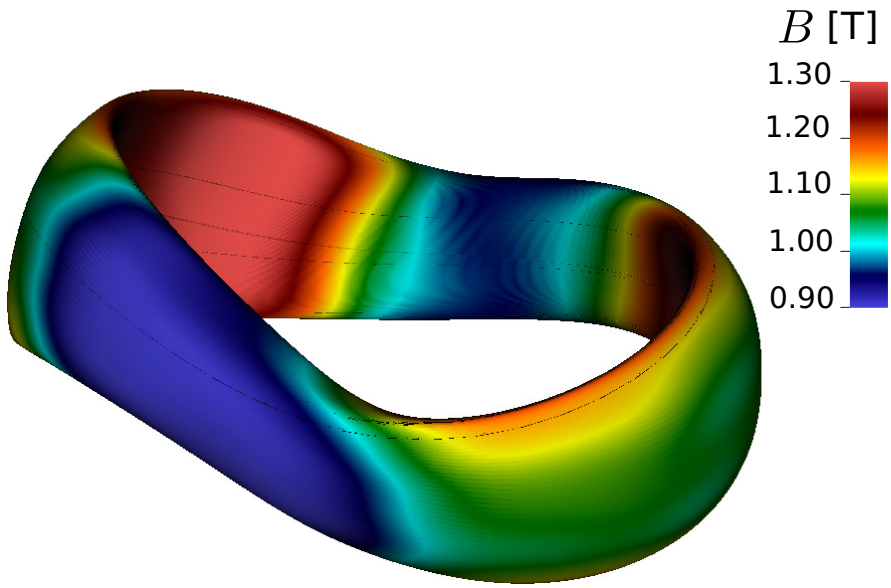

Figure 2.7: Isocontours of the magnetic field strength B of the QPS configuration under study in real space. The magnetic field is shown at the magnetic surface $s_0 = 0.49$.

deed, Fig. 2.7 shows a color plot of the isocontours of B in real space on a selected magnetic surface ($s_0 = 0.49$). It is apparent that the isocontours of B appear to be aligned vertically rather neatly, thus being rather independent of the poloidal direction, as one would expect from a quasi-poloidally symmetric case.

We have quantified the level of quasi-poloidal symmetry by means of the degree of quasi-poloidal symmetry ratio that was introduced in Chapter 1 (see Eq. 1.10). In this case, $M = 0$ and the sum in the numerator must be taken over all $m = 0$ modes. A new code, QSYM, has been specifically written for this purpose [40]. The result of the calculation is shown in Fig. 2.8 as a function of the Boozer radial coordinate. As it can be seen, the value of the ratio varies significantly, from almost perfect quasi-symmetry close to the axis ($\sigma(0) \sim 0.95$) to a smaller, but still significant value at the edge ($\sigma(1) \sim 0.65$). This kind of variation is rather usual in real configurations, since it is almost impossible to maintain a perfect level of quasi-symmetry throughout the whole device. It is usually better close to the axis and deteriorates as one moves to the edge (although this is not always the case!), where effects such as the discreteness

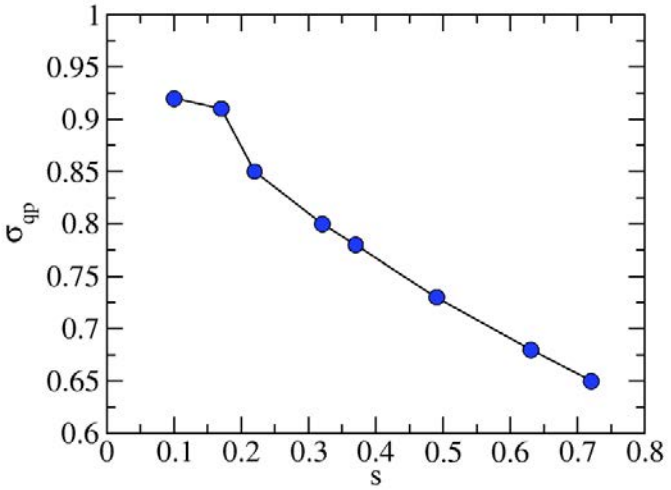

Figure 2.8: Degree of quasi-poloidal symmetry ratio σ_{qp} as a function of the magnetic surface for the QPS configuration examined. The selected surfaces at which GENE simulations will be carried out are marked by blue dots.

of the coils are felt more strongly.

In fact, we have taken advantage of the variability of the σ_{qp} ratio in the selected QPS configuration to facilitate our investigation of the effects of quasi-symmetries on the nature of radial turbulent transport, carrying out all the required full-annulus GENE simulations at various magnetic surfaces of the same QPS configuration. The selected locations are marked with blue dots in Fig. 2.8. The specific values for σ_{qp} and other quantities of interest at those locations have been collected in Table 2.1, that can be found at the end of the chapter.

2.2.3 Neoclassical transport in poloidally quasi symmetric configurations

In Chapter 1, we discussed the different types of particle orbits that must be considered within the neoclassical description of transport. In particular, we discussed the difference between trapped-particles and passing particles. In stellarators, as it is the case of the QPS configuration un-

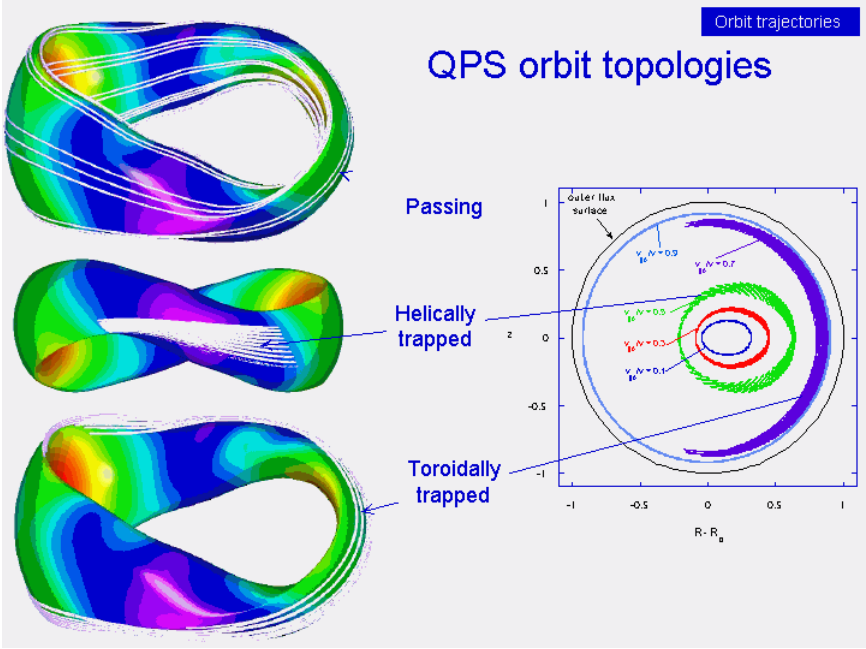

Figure 2.9: Different types of neoclassical orbits in quasi-poloidal stellarators: passing particles (light blue, in the toroidal projection on the right), helically trapped particles (green and red orbits) and toroidally trapped particles (purple orbit).

der study, trapped particles can be of two different types: *toroidal* and *helical* [32]. The former are similar to the tokamak trapped particles, in which the particle parallel velocity must change as it moves towards the high-field side of the toroidal configuration, whose strength must always decay as $B \propto 1/R$ according to Maxwell equations. In stellarators, however, particles can also be trapped inside the local wells that the magnetic field might have, since it is no longer independent of the toroidal angle. In poloidally quasi-symmetric magnetic fields, however, the fact that B is almost independent of the poloidal angle makes that helical trapped orbits are directed almost completely along the toroidal direction (see Fig. 2.9), which drastically reduces the width of the helically trapped bananas, leading to a better confinement than in non-quasi-symmetric configurations.

Another interesting prediction of neoclassical theory for poloidally quasi-symmetric configurations has to do with the neoclassical poloidal viscosity [38]. It is accepted that, at least in tokamaks, the neoclassical

estimate for the poloidal viscosity seems to be very close to what can be inferred experimentally, being the main mechanism that damps poloidal flows. Viscosities are estimated, in the neoclassical theory, by balancing the different contributions associated to each type of orbits [45]. The modifications in the relative importance of the contributions of these orbits introduced by quasi-symmetries result in a reduction of the neoclassical viscosity along the direction of quasi-symmetry with respect to non-quasi-symmetric configurations. This has been partially confirmed in experiments, at least for quasi-helical configurations [9]. As such, it is expected that neoclassical poloidal viscosity be significantly reduced in poloidally quasi-symmetric stellarators [10]. If this is the case, it should be much easier for turbulence-driven poloidal flows to be excited and also to saturate al larger levels, which should have a large impact in the suppression of turbulence and turbulent transport [11].

2.3 Gyrokinetic simulations of turbulence in the QPS configuration

We proceed now to discuss the various GENE simulations performed on the selected QPS configuration just described. The turbulent fields obtained will be used to carry out the investigation on the nature of transport that is the core of this thesis, and that is detailed in Chapter 5. The spatial domain used in all simulations is a full-annulus centered at a selected reference surface s_0. The various surfaces of the configuration at which simulations have been done are shown with blue dots in Fig. 2.8. The radial size of the computational domain used is $L_x \approx 140\rho^*$, with $\rho^* = \rho_{ref}/a = 0.004$. The box-length along the y-direction is calculated by GENE to be $L_y = \pi x_0/q_0$, thus including all line labels in the range $\alpha \in [-\pi/2, \pi/2]$. In all GENE simulations we have also assumed that there is no magnetic shear (that is, $q_0' = 0$) in order to avoid reconnection problems in the trajectories that will be calculated later by the TRACER code (see discussion in Chapter 4). As we also mentioned at the beginning of this chapter, periodic boundary conditions are assumed in all spatial directions. All equilibrium quantities are assumed constant and equal to their value at s_0, except for the magnetic field vector that depends on y and z as dictated by the VMEC equilibrium solution for the configuration.

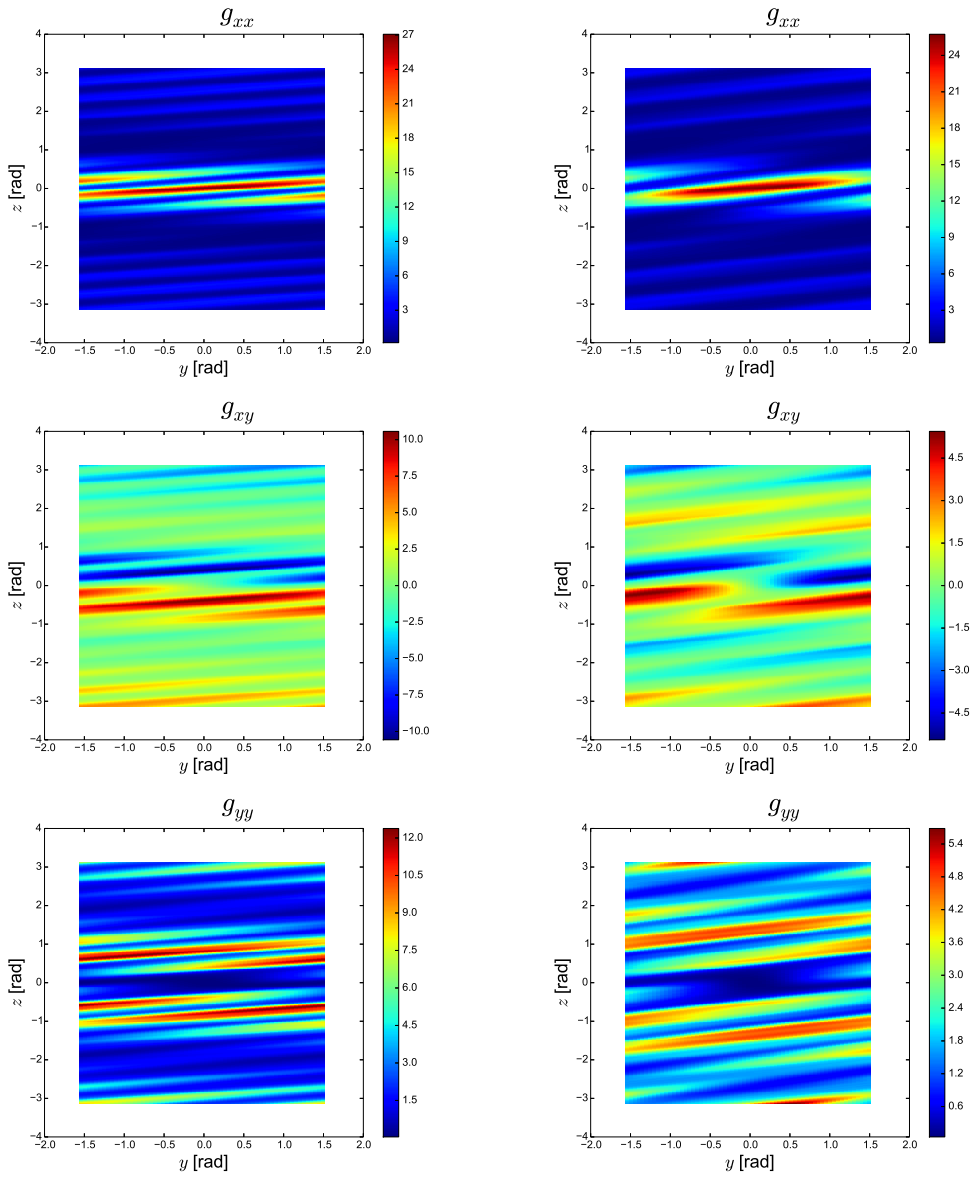

Figure 2.10: Three different elements of the metric tensor g_{ij} in GENE coordinates (y, z) generated by GIST at two different radial positions $s_0 = 0.10$ (left) and $s_0 = 0.63$ (right). From top to bottom, the elements shown are g_{xx}, g_{xy} and g_{yy}.

Finally, all gyrokinetic simulations carried out assume that the dominant instability is the electrostatic ITG mode. In them, the adiabatic

electron approximation is always assumed, so that no evolution of the electron distribution function is required. In addition, the magnetic field is not evolved, being equal to the equilibrium one during the simulation. This is believed to be a sufficiently good approximation for the low-β plasmas ($\beta = 2\mu_0 p/B^2$, measures the ratio between plasma and magnetic energy) that will be considered in this thesis, that have $\beta \sim 2\%$.

2.3.1 GIST processing of VMEC data

The GIST code [84] has been used to process the information about the three-dimensional equilibrium magnetic field provided by the VMEC code and to transform it to the form needed by GENE in its own internal coordinate system. The type of output GIST produces is illustrated in several figures. First, Figure 2.10 shows three of the most important elements from the metric tensor of the transformation to GENE internal coordinate system, $\hat{g}_{ij}$, for two different radial positions. On the left column, isocontours for the selected components of the metric tensor are shown for the more internal position, $s_0 = 0.10$, whilst on the right column, the same metric elements are shown for a more external one, $s_0 = 0.63$.

As it can be appreciated, very similar structures are observed at both radial positions. These structures are more elongated (thinner in the z-direction and longer in the y-direction) in the internal simulation than in the external one, which is related with the radially decreasing safety factor q (number of toroidal turns per a single poloidal turn) of QPS. In both cases, for the internal and external surfaces, the bad curvature region effects are visible around $z = 0$ ($\theta_B = 0$), the central region of each plot, particularly for the g_{xx} metric element.

The Jacobian of the transformation to the internal GENE coordinates and the strength of the magnetic field estimated by GIST from the equilibrium fields computed by VMEC for the QPS configuration are shown in Fig. 2.11, also for the same internal and external magnetic surfaces for which Fig. 2.10 was prepared.

The upper frames of the figure show a colour map of the isocontours of the magnetic field strength, B; the lower frames shown the isocontours for the Jacobian $\sqrt{g}$. Similar comments to those already made while discussing the metric tensor $\hat{g}$ about the elongated nature of the isocontours could be made here. The reasons are very similar to the ones given previously. It is also apparent that the larger number of distinct iso-

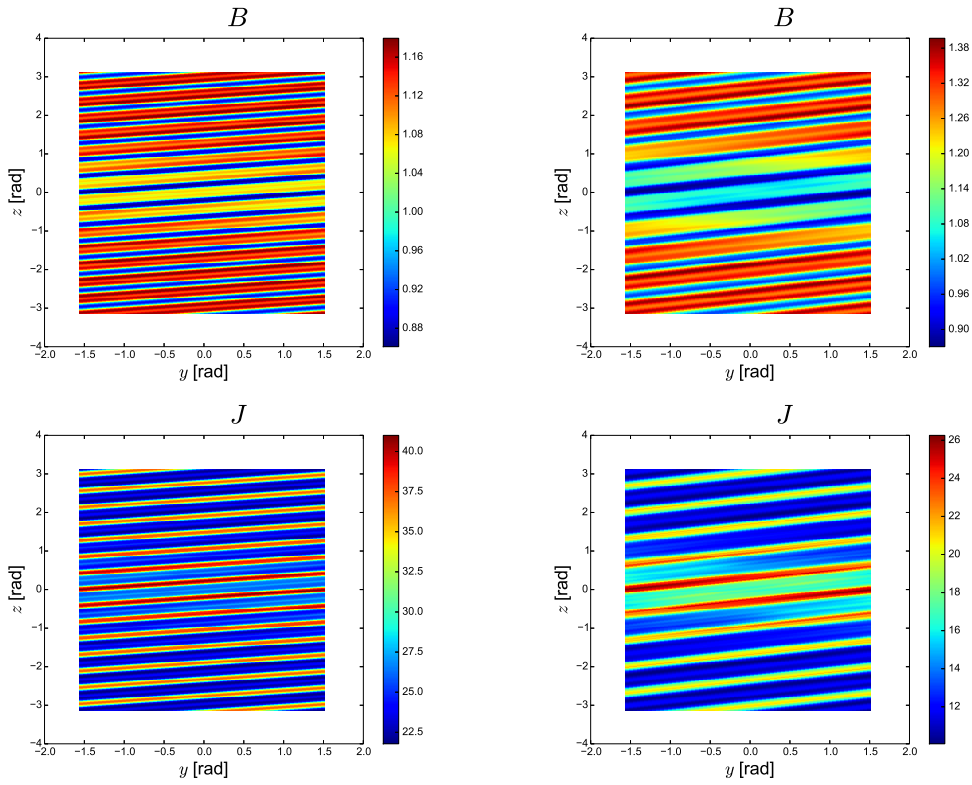

Figure 2.11: Magnetic field strength (above) and Jacobian (below) generated by GIST for the QPS configuration under study at surfaces $s_0 = 0.10$ (left) and $s_0 = 0.63$ (right). All plots are in GENE internal coordinates, (y, z).

surfaces that appear at the more interior surface is related with the higher value of the safety factor as compared with the more exterior surface. The effects of the bad-curvature region are again visible around $z = 0$ in both cases, but are stronger in the external case.

2.3.2 Numerical mesh

As it was mentioned at the beginning of the chapter, GENE purposely chooses field-aligned spatial coordinates to decouple the parallel resolution requirements of the turbulent simulations from other directions, taking thus advantage of the strong asymmetry that exists in the direction

parallel to the magnetic field compared with the perpendicular dynamics.

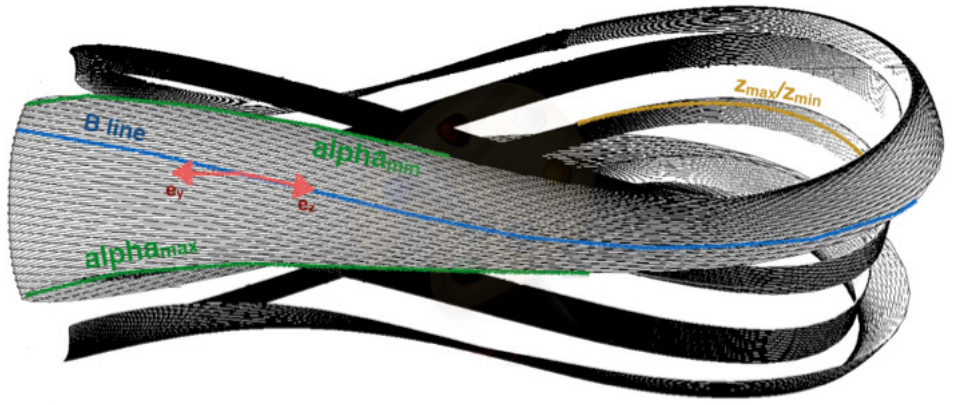

Figure 2.12: GENE spatial mesh shown for a selected surface ($s_0 = 0.10$) of the QPS configuration studied. A magnetic field line is also shown, in blue, together with some of the director vectors: $\mathbf{e_y}$ and $\mathbf{e_z}$.

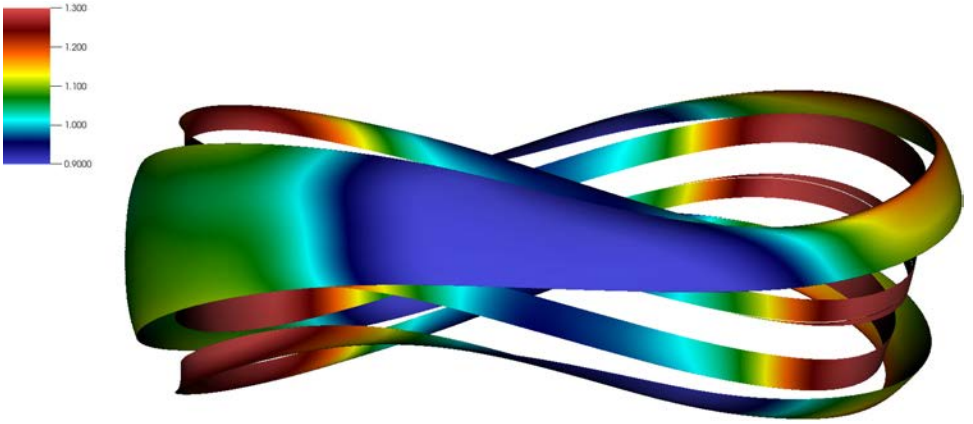

Figure 2.13: Isocontours of the magnetic field strength B in real space on the same selected surface as Fig. 2.12.

In local (flux-tube and full-annulus) simulations, periodicity in all directions is further imposed to help reduce the computational time even more by means of efficient Fast Fourier Transform (FFT) libraries. However, all these choices, together with the up-down symmetry and periodicity of the stellarator configuration, lead to a spatial mesh that, when looked at in real space, is not just a simple annulus around the reference magnetic surface. Instead, it is actually much more complicated than it

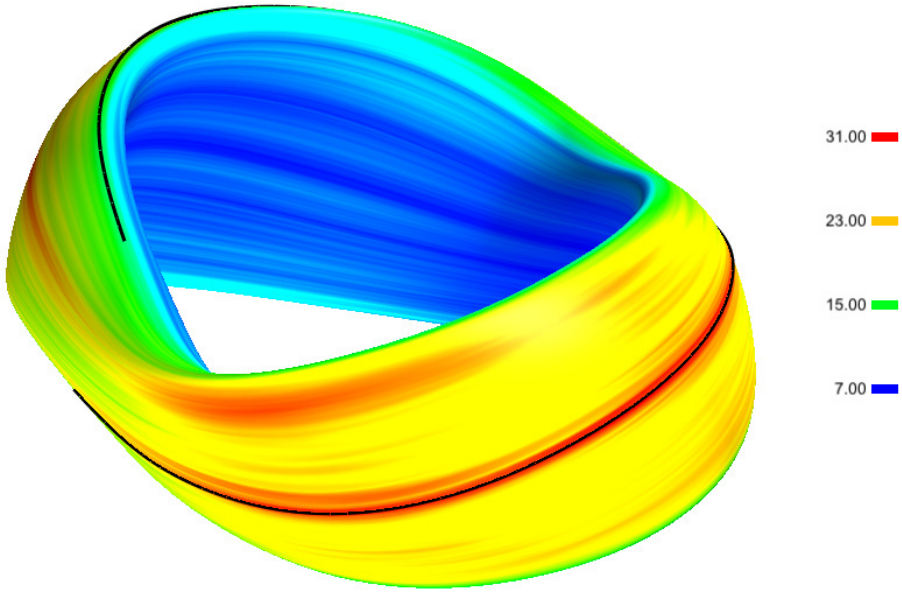

Figure 2.14: Electrostatic turbulent potential Φ of the QPS configuration of study in cartesian coordinates with the real shape and geometry of the plasma. The potential is estimated around the magnetic surface $s_0 = 0.49$ (s being the Boozer radial coordinate).

might seem.

Fig. 2.12 shows the spatial mesh used by GENE in real space for one of the simulations carried out for the QPS configuration. The limiting values for the line label α in green, as α_{min} and α_{max}, and a magnetic field line in blue with the covariant unitary vectors $\mathbf{e_y}$ and $\mathbf{e_z}$ are also shown. We have also included a figure in which a color map for the magnitude of the magnetic field, B, is represented in the mesh in real space (see Fig. 2.13). The poloidal quasi-symmetric nature of the magnitude of the magnetic field is still apparent in real space, with the isocontours of constant magnitude of B being almost vertical.

It must be remembered that, although GENE solves (an approximation to) the (gyroaveraged) Poisson equation (Eq. 2.10) to obtain the turbulent electrostatic potential in the spatial mesh, (x, y, z), the ion gyrokinetic equation is not solved in real space, but in phase space, that spans the coordinates $(x, y, z, v_\parallel, \mu)$. The numerical resolution of the phase space mesh has been set, in all the simulations that compose this study,

to $(126 \times 64 \times 256 \times 32 \times 8)$ nodes. This choice may not be the optimal one for all magnetic surfaces, but it is a very reasonable one for all of them. To ensure that this is indeed the case, we have made a very careful and complete systematic linear and nonlinear convergence study for each surfaces. In these studies, we monitored the saturation levels of various physical variables such as the ion heat flux and the parallel and perpendicular ion temperatures, among others. We describe some of the convergence tests in the following section.

Convergence tests

The typical aspect of the turbulent electrostatic potential $\tilde{\Phi}$, for the QPS simulations discussed in this thesis, is shown in real space in Fig. 2.14. It can be easily appreciated that the turbulent, saturated structure, once the linear growth phase has been left behind, exhibits a clear anisotropy, with structures being strongly aligned along the field lines as expected.

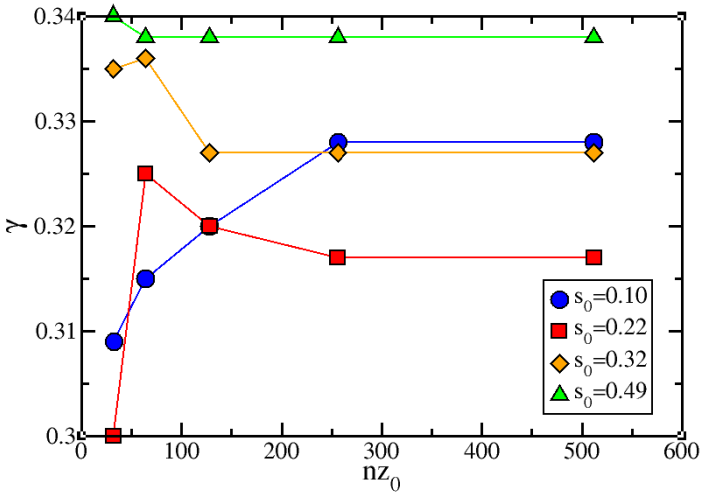

Figure 2.15: Study of the n_z dependence of the growth rate γ for linear flux-tube simulations of GENE in different radial positions of interest of the QPS equilibrium.

However, it is important to ensure that this solution is well converged with respect to the various parameters that establish the resolution along each of the 5 directions in phase space.

The first thing to consider is that in stellarators, where the magnetic field varies its magnitude toroidally and poloidally, the z-direction is one of the most important to resolve. For that reason, we have determined the minimum admissible value for n_z, the number of points consider along the z direction, by testing for good convergence in the z direction using in linear and non-linear flux tube simulations. To do this, we have performed simulations in which all parameters are identical except for the number of points along the z-direction.

We have started by calculating the growth rate of linear, flux-tube ITG simulations at the selected radial positions of interest as a function of the number of points included in the z-direction. The results of several of these runs are shown in Fig. 2.15. From the figure, it is clear that $n_z = 256$ seems to be the minimum resolution admissible in order to achieve good convergence for all surfaces of the selected QPS configuration. From the plots, it is also clear that the innermost surfaces require a higher resolution than the outer ones. This fact is related with the larger value of the safety factor $q(s)$, that increases considerably as one moves towards the center of the device. Indeed, $q(0) \sim 9$, whilst $q(a) \sim 4.5$ (see Fig. 2.4).

Ensuring linear convergence is however not sufficient, since our interest lies in investigating the nature of radial turbulent transport in the long-term, non-linearly saturated regime (see Chapter 5). To determine the minimum n_z admissible for nonlinear convergence of the results, we have also estimated the saturated levels of the turbulent ion radial heat flux, $\tilde{Q}_i$, reached by non-linear, flux-tube simulations carried out at the same locations as a function of n_z. The ion heat fluxes have been averaged over the whole computational volume. The results are shown in Fig. 2.16, confirming that $n_z = 256$, the linear result, is also sufficiently good in the non-linear regime.

Curiously, the value of the safety factor does not seem to have such a strong impact on non-linear convergence as it for linear convergence, probably because the nonlinear interaction is less affected by the magnetic topology than the spatial structure of the linear mode.

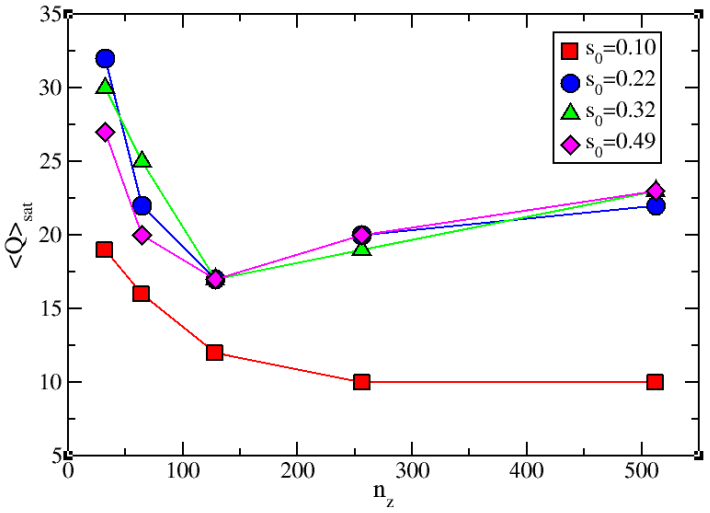

Figure 2.16: Saturated level of volume averaged radial heat flux $< \tilde{Q}_i >$ as a function of n_z for different radial positions in the QPS-equilibrium.

Next, we discuss the convergence studies to determine the minimum admissible value for n_y, that gives the resolution along the y direction. After fixing $n_z = 256$, the procedure to investigate the n_y-convergence is almost identical to what was done for n_z. But in this case we use full-annulus simulations instead of flux-tube ones. The reason for this change (that leads to an increase in complexity and computational time) is that the field variation on the magnetic surface, but perpendicular to the field line, plays an important role in the perpendicular transport dynamics and must therefore be included.

We have investigated first the variation of the growth rate value γ obtained from linear simulations with different values for n_y. The results are shown in Fig. 2.17, although only for one interior and one exterior radial position (full-annulus simulations are computationally very expensive, so available resources only allowed for two simulations). From the figure, it seems clear that one needs to use at least $n_y = 64$ to guarantee good linear convergence along the y direction.

Next, similarly to what we did to determine the minimum acceptable value for n_z, we proceed to look for the minimum value for n_y that guarantees non-linear convergence.

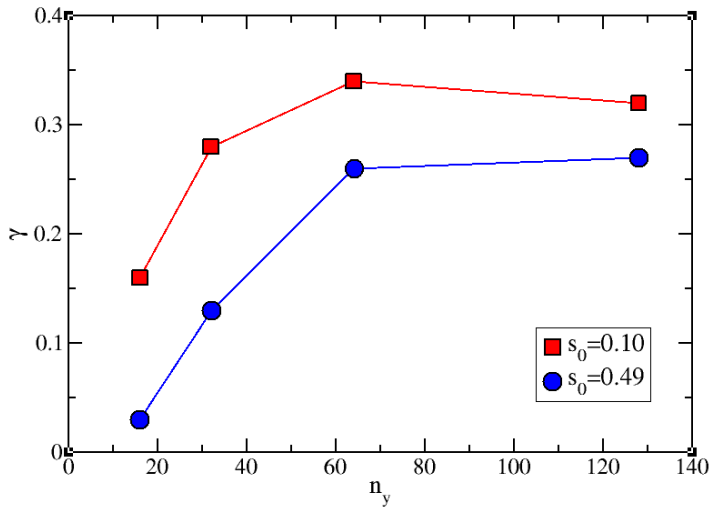

Figure 2.17: Study of the n_y dependence of the growth rate γ for linear full-anullus simulations at different radial positions of interest of the QPS configuration.

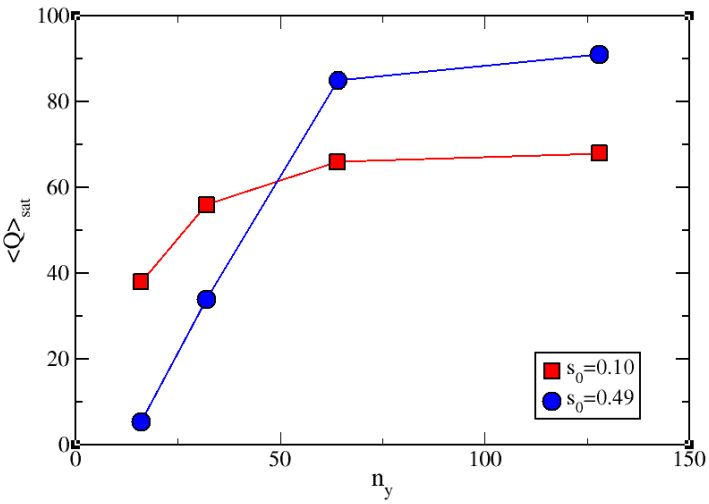

Figure 2.18: Saturated level value of volume averaged radial heat flux $< Q >$ as a function of n_y for different radial positions in the QPS-equilibrium.

Again, we have calculated the volume-averaged radial ion heat flux as a function of n_y for the two full-annulus simulations completed after they reach saturation. The results, shown in Fig. 2.18, also points to $n_y = 64$ as the minimum admissible resolution along the y direction that can provide sufficient convergence both linearly and nonlinearly at all surfaces in the selected QPS configuration.

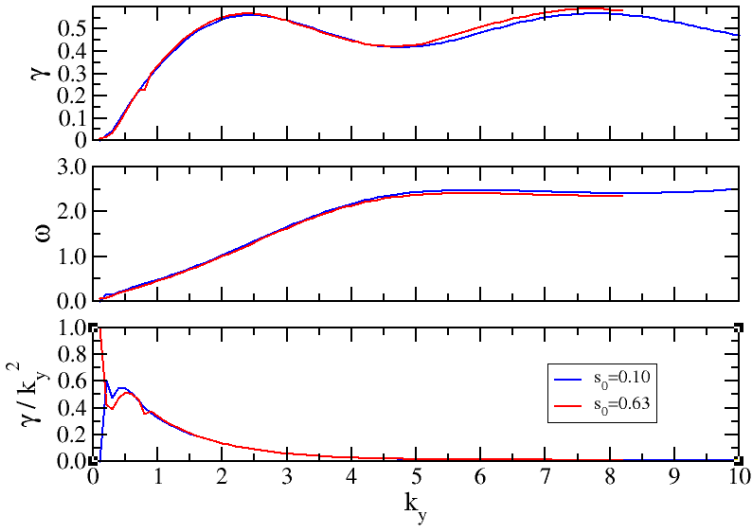

Figure 2.19: Top: Growth rate γ study as a function of the k_y. Middle: Real part of the growth rate ω. Bottom: Effective diffusivity at each wavenumber $D_k := \gamma/k_y^2$.

It must be made clear, however, that the fact that a simulation is well converged with respect to the spatial resolution does not necessarily guarantee that all the relevant physics are included. In the case of the y-direction, the dynamics of interest are those important for the ITG mode. To ensure that $n_y = 64$ includes all the relevant ITG physics, we have also calculated the linear growth rate for different wavenumbers along y, k_y. The results are shown in the upper frame of Fig. 2.19. Interestingly, as it is typical in most stellarators, the growth rate does not go to zero as k_y increases. The relevant quantity to look at here is, however, the level of transport associated to the ITG mode. Using a mixing-length estimate that assumes diffusive transport dynamics, the contribution to the overal radial transport of each wavenumber can be roughly estimated as $D_{k_y} \sim$

γ/k_y^2. This "effective diffusivity at scale $1/k_y$" is plotted, as a function of k_y, in the lower frame of Fig. 2.19. The plot clearly shows that the impact on transport is reduced greatly for $k_y > 3.5-4$. This result coincides with the rough estimation that GENE does for the size of the computational box along y that, for $n_y = 64$, is $L_y \sim 115$. Using it, a maximum meaningful k_y number can be estimated via $k_{ymax} = n_y 2\pi/L_y \simeq 3.5$.

The last spatial resolution number to determine is n_x, the size of the computational box along the x. To find its minimum admissible value, we have fixed $n_z = 256$ and $n_y = 64$ and proceeded to carry out a convergence study for n_x. In full-annulus simulations, GENE however requires as input the maximum number of distinct wavenumbers included along the x-direction, n_{kx}, instead of the number of points in the real mesh. Therefore, it is n_{kx} that has been varied in the last set of non-linear, full-annulus simulations performed. The results are shown in Fig. 2.20, that shows the volume-averaged radial ion heat flux as a function of n_{kx}. From the plot, it seems clear that the minimum acceptable value is around $n_{kx} = 64$, that translates into $n_x = 126$ in the real mesh.

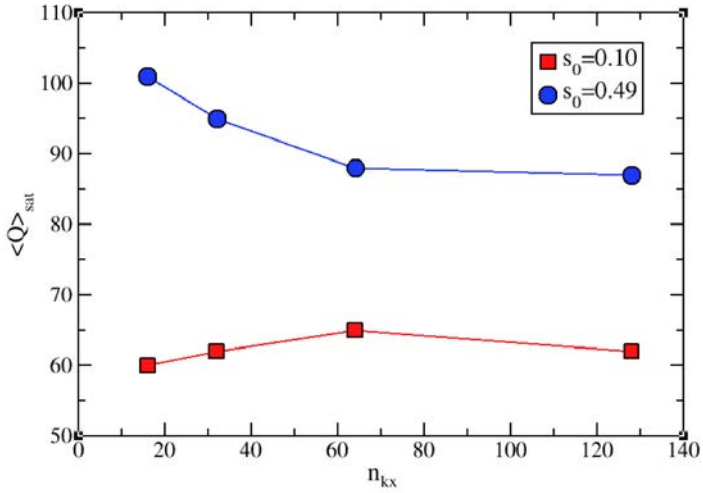

Figure 2.20: Saturated level value of volume averaged radial heat flux $< Q >$ as a function of the number of wavenumbers along x, n_{kx}, for different radial positions in the selected QPS-equilibrium.

Regarding the resolution used along the two velocity directions, $v_\parallel$ and μ, that complete the phase space in which the ion distribution func-

tion is defined, similar convergence studies have been done. To avoid repeating ourselves too much, we simply provide here the resulting minimum admissible resolutions, that were estimated to be $n_v = 32$ and $n_\mu = 8$ by using the same methodology. These minimum resolution values are rather similar to those obtained for other gyrokinetic simulations of ITG electrostatic turbulence carried out in stellarator geometries with other types of quasi-symmetries (quasi-helical [86] and quasi-axisymmetric [87, 88]) by members of the GENE team as well as other independent users of the code.

2.3.3 Temporal length of the gyrokinetic simulations used in this study

The studiesthat will be carried out in Chapter 5 to determine the nature of radial transport must be done over the nonlinearly saturated regime of the turbulence. More precisely, the determination of the long-term nature of transport, which is the goal of this work, requires that turbulence be advanced for several tens, if not hundreds, of turbulence decorrelation times.

As a general rule, one can roughly estimate the decorrelation time as the inverse of the linear growth rate of the dominant instability that, in this case, is the ITG mode. Fig. 2.21 shows the time-trace of the (volume-averaged) ion radial heat flux as a function of time that was obtained with GENE for two of the full-annulus, nonlinear simulations that we have carried out in the selected QPS configuration. At the beginning of each run, the exponential growth phase associated to the linear growth rate of the dominant ITG mode can be easily identified. Its growth leads to an estimate of the decorrelation time of the order of $\tau_{dc} \approx 20 - 40\ a/c_s$, depending on the magnetic surface examined. From this estimate, we have inferred that the minimum admissible length of the simulations, for the type of studies we are interested in, correspond to around $50 - 100$ decorrelation times.

2.3.4 Ion Temperature Gradient threshold value

The dominant instability in all the GENE simulations we have carried out for the QPS configuration is the electrostatic ITG mode. Since the density gradient has been purposely set to zero (that is, the characteristic length

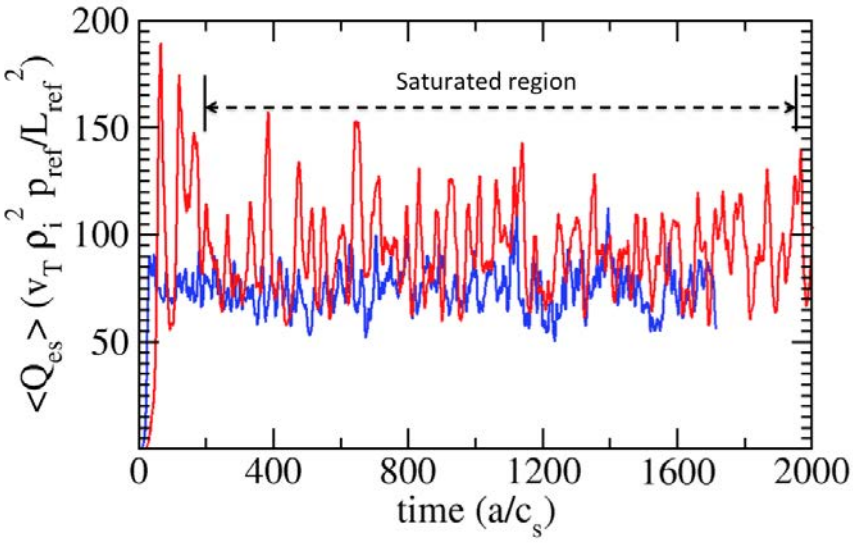

Figure 2.21: Time evolution of the (volume averaged) radial heat flux along for two different nonlinear simulations realized at the magnetic surfaces located at $s_0 = 0.17$ (blue) and $s_0 = 0.49$ (red).

of the ion density (see Eq. 2.25), $\omega_n = 0$), the ion temperature gradient becomes the quantity that sets the threshold for the onset of the ITG instability. In order to select an adequate temperature gradient value, ω_T (see Eq. 2.25), we have performed an study of the dependence of the linear growth rate on the value of ω_T using non-linear, full-annulus runs at different radial positions.

Fig. 2.22 shows the results of the study at three different radial positions. The threshold value obtained in these runs for the onset of the instability is roughly around $\omega_T^{\text{threshold}} \simeq 2$ on all surfaces. In view of this result, we have settled with a value $\omega_T = 4$ for all the nonlinear simulations that will be used for the investigation described in Chapter 5. With this choice, we ensure that all simulations remain well above the marginal point, where the nonlinear saturation of the turbulence would take place more slowly, thus requiring much longer runs and larger resources that

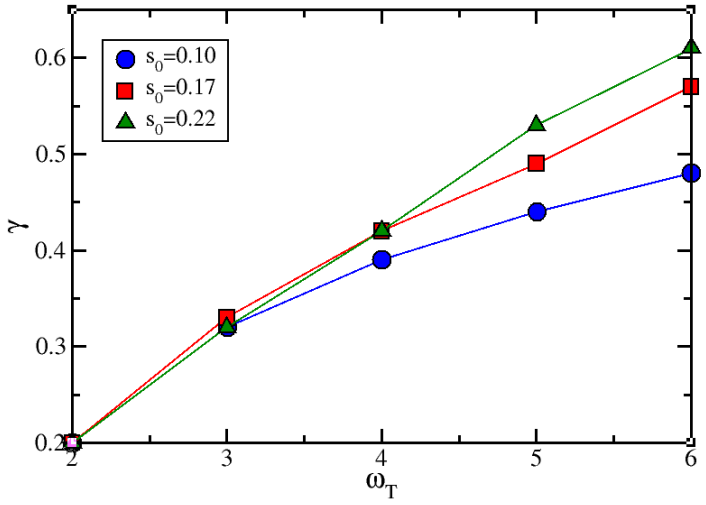

Figure 2.22: Growth rate γ variation with the temperature gradient ω_T for three different radial position of the QPS equilibrium. .

what was at our disposal, and where, even more importantly, some of the underlying ordering assumptions of gyrokinetic theory might be less well justified [70, 71].

2.3.5 Standard characterization of radial turbulent transport for the QPS nonlinear simulations

Once the resolution, main parameters and surfaces for the simulations have been determined and selected, we proceed to describe next the main transport properties of the runs carried out with the GENE code. The analysis presented in this section follows the standard approach to this kind of studies, very common in the literature [71], but that is rather different from the analysis that we will carry out in the remainder of this thesis, but that is still valuable for comparison purposes with the work of other authors in other quasi-symmetric configurations [86, 87, 88].

The saturated value of the (volume-averaged) ion heat radial flux $< \tilde{Q}_i >_{Sat}$, time-averaged over the saturated regime, is one of the most used diagnostics among GENE users (see Fig. 2.21). In the traditional analysis, that assumes that turbulent transport can be modelled via an effective diffusion operator as previously discussed, an effective thermal

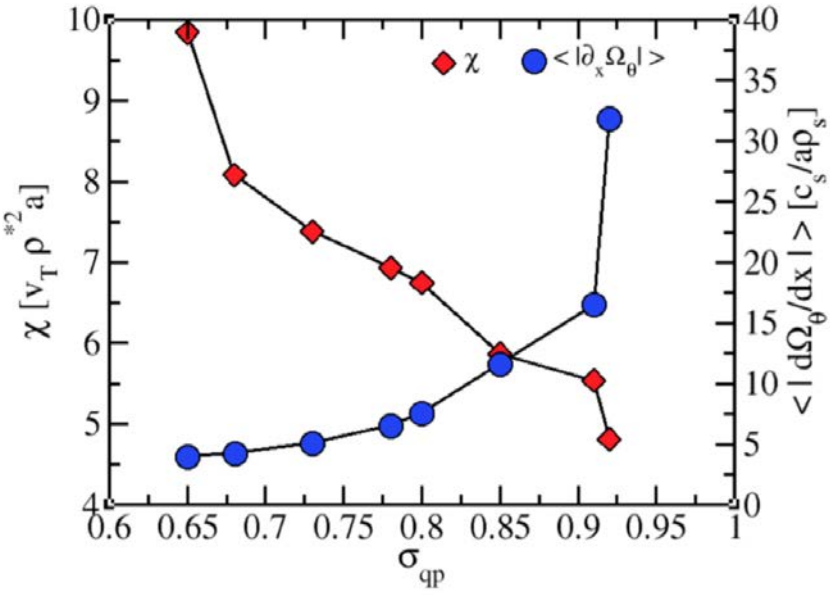

Figure 2.23: Ion thermal conductivity χ_i (left, in red) and radial shearing strength of the plasma poloidal flow (right, in blue) as a function of the degree of quasi-poloidal symmetry $\sigma_{qp}(s)$.

ion conductivity χ_i is estimated from the ratio,

$$\chi_{i_{eff}} = \left\langle \frac{-\tilde{Q}_i}{\nabla T_i} \right\rangle_V \approx -\frac{< \tilde{Q}_i >_{Sat}}{\nabla T_i} \tag{2.26}$$

In our study, however, since the temperature gradient is fixed (i.e., $\omega_T = 4$), the effective conductivity behaves essentially as a surrogate of the ion heat flux.

The influence of quasi-symmetry on radial transport can be investigated by plotting the value of the effective thermal conductivity at each surface (see also Table 2.1 at the end of the chapter) in terms of the value of the degree of quasi-poloidal symmetry, σ_{qp} (Eq. 1.10). The result is shown in Fig. 2.23 [40]. Clearly, the ion thermal conductivity is negatively correlated with the degree of quasi-poloidal symmetry. The resulting reduction in radial transport is consistent with the results obtained, by other authors, in non-linear gyrokinetic simulations carried out in quasi-helically symmetric [86] and quasi-axisymmetric [87] devices, where the

radial ion heat transport was also found to decrease as the magnetic field strength became endowed with larger degrees of quasi-symmetry.

We have also tested the hypothesis of whether the observed reduction in radial transport is correlated to the larger ability of the plasma to generate poloidal flows with strong radial shear, that would follow from the reduced neoclassical poloidal viscosity expected in regions of high levels of quasi-poloidal symmetry [38]. To do it, we have chosen as a figure-of-merit for the shearing power of the flow the volume-average of the x-derivative of the local angular poloidal velocity, Ω_θ. This quantity, in GENE internal coordinates, can be computed as [40]:

$$\Omega_\theta = \frac{(v_z + C_y q_0 v_y)/\sqrt{g}}{g_{zz} + C_y^2 q_0^2 g_{yy} + 2 C_y q_0 g_{yz}}, \tag{2.27}$$

where q_0 is the safety factor at the surface where the simulation is centered, v_z and v_y are the covariant components of the $\mathbf{E}\times\mathbf{B}$ drift velocity, and g_{zz}, g_{yy} and g_{yz} are the proper covariant metric elements. The reason to choose Ω_θ is because it is intrinsically related to the part of the poloidal angular turbulent velocity which is tangent to the magnetic surface $s = s_0$. As clearly seen in Fig. 2.23 (see also Table 2.1), there is indeed an important positive correlation between the radial shearing strength of the poloidal flow and the degree of quasi-poloidal symmetry, as previously theorized [38].

However, it is worth noting that, from the fact that a finite effective conductivity can be computed in this (or any other) case (using, for instance, Eq. 2.26), it does not necessarily follow that the nature of radial heat transport is diffusive in the system. Such a conclusion has been forced into the description adopted here, not derived from the analysis. In fact, in any finite system where transport is non-diffusive over a certain range of scales, effective coefficients can be computed but they will be unable to properly capture the dynamics over those scales. The analysis of the advection of massless tracer (and also massive) particles that we will describe in the remainder of this thesis, and that is discussed at length in Chapter 5, will further prove the truth of this statement, since it will yield non-diffusive values for the transport exponents (α and H, introduced in Chapters 2 and 3). Therefore, the analysis suggests that radial transport of an increasingly non-diffusive nature sets in as the degree of quasi-symmetry increases. Although, strictly speaking, our advection analysis refers only to radial particle transport (and not to heat conductive

s_0	σ_{qp}	q	$\chi_T\,[v_T\rho^{*2}a]$	$\langle Q_i\rangle_V\,[Q_{ref}]$	$\langle\lvert d\Omega_\theta/dx\rvert\rangle_V\,[\xi_{ref}]$
0.10	0.92	7.42	4.81	62.67	31.87
0.17	0.91	6.56	5.54	74.38	16.52
0.22	0.85	5.75	5.87	77.85	11.65
0.32	0.80	5.44	6.75	87.41	7.59
0.37	0.78	5.22	6.93	88.68	6.55
0.49	0.73	4.90	7.38	92.42	5.12
0.63	0.68	4.68	8.08	99.20	4.27
0.72	0.65	4.60	9.84	100.52	4.02

Table 2.1: Values, at the various surfaces of the QPS configurations where GENE simulations have been carried out, for the quasi-poloidal symmetry ratio σ_{qp}, the safety factor q, the effective ion thermal conductivity χ_T, the (volume-averaged) ion heat flux $\langle Q\rangle$ (with $Q_{ref} = v_T\rho^{*2}p^0_{ref}/L^2_{ref}$) and the radial shearing capability of the poloidal flow $\langle\lvert\,\mathrm{d}\Omega_\theta/\,\mathrm{d}x\rvert\rangle$.

transport), these results do still suggest that a description of heat transport in terms of usual conductivities might not be the most appropriate either.

Chapter 3

Diagnostics to characterize the nature of transport in numerical simulations of turbulence

The main objective of the present thesis is to answer the question of whether the nature of the turbulent transport along the radial direction (i.e. along x, in GENE internal coordinates) changes, in a quasi-poloidal stellarator, as the level of quasi-symmetry is varied. We have at our disposal, to investigate this question, a set of full-annulus gyrokinetic simulations of electrostatic ITG turbulence, carried out with the GENE code, in the neighbourhood of different magnetic surfaces of a selected configuration of the QPS device. The degree of quasi-poloidal symmetry varies from one surface to another, so that we need a methodology to examine them in a way in which the nature of radial transport can be made apparent.

Two independent methods will be used in this thesis to characterize the nature of radial transport. This duality will allow us to compare and better validate the results. The first method relies on the determination of *propagators* and the analysis of their (fractional) standard deviation growth. Both the propagator and the (fractional) standard deviation are determined numerically by advancing in time an initially peaked distribution of tracked particles as they are affected by the turbulence. On the other hand, the second technique is based on the determination of the statistical and correlation properties of the Lagrangian velocities of the

tracked particles, also as they are advected by the background turbulence.

We introduce the basics of both techniques in this Chapter. Since both methods characterize the nature of transport by comparing the properties of the motion of the tracked particles with those of fractional Lévy motion (fLm), we will start by discussing this model. The fLm is a stochastic model that generalizes the popular Langevin equation from which classical diffusion (i.e., Eq. 3.3) is often derived. As a result, fLm is a good model to describe non-diffusive transport.

3.1 Fractional Lévy motion

The traditional Langevin equation gives the position of a single particle moving in one dimension as [55]:

$$x(t) = x_0 + \int_0^t \mathrm{d}t' \xi_2(t'), \tag{3.1}$$

where $\xi_2(t)$ is a Gaussian, uncorrelated noise with a correlation function given by $\langle \xi_2(t)\xi_2(t')\rangle = D\delta(t-t')$ and D its diffusivity. The connection between the Langevin equation and the usual diffusive transport can be easily established, for example, by computing the propagator of Eq. (3.1). The *propagator* is the probability of finding the particle at any position x at time $t > 0$ starting at x_0 for $t_0 = 0$. In the case of the Langevin equation, its propagator is [55]:

$$P_{\mathrm{LE}}(x,t|x_0) = \frac{1}{\sqrt{2\pi Dt}} \exp\left(-\frac{(x-x_0)^2}{2Dt}\right). \tag{3.2}$$

That is, the propagator has the form of a Gaussian distribution with a standard variation that grows with time as $\sigma_{\mathrm{LE}} = (Dt)^{1/2}$.

In the case of particle diffusive motion, the equation of transport is well known and given by,

$$\frac{\partial n}{\partial t} = D\frac{\partial^2 n}{\partial x^2}. \tag{3.3}$$

It turns out that the propagator and (the standard deviation) of the diffusive equation is also given by Eq. 3.2. Because of that, the Langevin equation is often used as a model of the "microscopic dynamics" of systems that exhibit macroscopic diffusive transport [55].

In a natural turbulent system, however, the role of the noise would be played by the Lagrangian velocity of the particle being transported, whose correlation function is often modelled as,

$$\langle v(t)v(t')\rangle \sim v_c^2 \exp\left(-\frac{|t-t'|}{\tau_c}\right). \tag{3.4}$$

With this choice, the long-term, long-distance limit of transport is also well described by the classical diffusive equation with diffusivity $D \sim v_c^2\tau_c$.

Therefore, one can conclude that the long-term dominance of diffusive transport is ultimately related to the existence of finite characteristic scales, in space as in time, associated to the transport process. Those scales, for the turbulent system just discussed, are $l_c \sim v_c\tau_c$ and τ_c respectively. The characteristic velocity, v_c, is related to the (square root of the) variance of the distribution of Lagrangian velocities; τ_c, on the other hand, determines for how long memory is maintained (in its velocity) as the particle advances along its (Lagrangian) trajectory.

3.1.1 Fractional Langevin equation

However, there are situations, where characteristic transport scales do not exist. In those situations Eq. 3.1 is not an appropriate model to capture the transport dynamics. These instances are often referred to under the general name of *non-diffusive transport* [56]. In those cases, a more suitable generalization than the Lagevin equation is provided by the stochastic equation [89, 90]:

$$x(t) = x_0 + \frac{1}{\Gamma(H-\frac{1}{\alpha}+1)}\int_0^t \mathrm{d}t'(t-t')^{H-\frac{1}{\alpha}}\xi_\alpha(t'), \tag{3.5}$$

where $\Gamma(x)$ represents the Euler's gamma function. Here, $\xi_\alpha(t)$ is again noise, but distributed in this case according to an uncorrelated, symmetric Lévy distribution [90], (see *Appendix A: Lévy distributions*, for a brief introduction to these pdfs) with a tail exponent $\alpha \in (0, 2]$ instead of a Gaussian distribution. In fact, the Gaussian distribution is just a particular case of symmetric Lévy distribution with $\alpha = 2$. For $\alpha < 2$, Lévy distributions have a fat power-law tail, $L_\alpha(x) \propto |x|^{-(1+\alpha)}$, and lack a finite variance (in fact, all moments of order α or larger are infinite [90]). Clearly, ξ_α can no longer be a surrogate of the Lagrangian velocity. The

latter is obtained by differentiating (with some care) Eq. 3.5. The exponent $H \in (0, \max(1, 1/\alpha)]$, on the other hand, is referred to as the *Hurst exponent* [91]. Its range of possible values is limited to ensure that the propagator of Eq. 3.5 remains well-behaved [90].

It can be shown that the fractional Langevin equation asymptotically tends, for $\alpha < 2$ and in the fluid limit ($x, t \to \infty$), to the fractional differential equation [92]:

$$\frac{\partial n}{\partial t} = -{}_0D_t^{1-\alpha H}\left[D\frac{\partial^\alpha n}{\partial |x|^\alpha}\right], \tag{3.6}$$

where ${}_0D_t^{1-\alpha H}$ (known as a *Riemann-Liouville time derivative*) and $\partial^\alpha/\partial|x|^\alpha$ (a *spatial Riesz derivative*) are two integro-differential operators, known under the general name of *fractional operator* (see *Appendix B: Fractional derivatives and integrals* for a quick introduction to these operators), that respectively integrate over the past history of the system and the whole spatial domain [61, 62]. This extended integration domains are a reflection of the lack of characteristic scales in time and/or in space.

We conclude this subsection with two comments relative to Eq. 3.6. First, it is traditional to introduce an additional (temporal) fractional exponent β, defined via the relation:

$$\beta = \alpha H. \tag{3.7}$$

We will discuss its significance soon. Secondly, the relation between local particle fluxes (i.e., Γ) and density gradients (i.e., ∇n) in Eq. 3.6 is no longer given by the classical Fick's law (see Eq. 1.11). Instead, much more complicated relations that involve a fractional integro-differential kernel appear [93]. Thus, effective diffusivities cease to have a clear physical meaning in this context, even if they can still be estimated as the ratio of these two quantities.

3.1.2 Fractional Brownian motion

Several famous stochastic models are contained, as particular cases, inside Eq. (3.5). For instance, the usual Langevin equation is recovered by making the choice of exponents: $\alpha = 2$ and $H = 1/2$. On the other hand, if $\alpha = 2$ but H is not fixed, Eq. (3.5) reduces to the famous *fractional Brownian motion (fBm)* introduced by Mandelbrot in the 60's. The propagator

of fBm is still a Gaussian distribution but with a standard deviation that grows in time like [91]:

$$\sigma^{\text{fBm}} \propto \frac{(Dt)^H}{(2H)^{1/2}\Gamma\left(H+\frac{1}{2}\right)}. \tag{3.8}$$

Clearly, the fBm propagator only scales diffusively if $H = 1/2$. Otherwise, fBm transport is either *subdiffusive* ($H < 0.5$) or *superdiffusive* ($H > 0.5$).

One can also study the properties of fBm transport from the ordered sequence of its velocities (obtained by direct differentiation of Eq. 3.5). It turns out that, although the variance of the pdf of these velocities (that sets the velocity scale, v_c, as was previously discussed) is well defined, a finite timescale (i.e., τ_c) is lacking whenever $H \neq 1/2$. This means that memory (i.e., long-term temporal correlations) is being maintained for infinitely long times along the Lagrangian trajectory, a consequence of the power-law kernel in Eq. (3.5). As a result, the long-term, long-distance limit of transport no longer corresponds to classical diffusion.

3.1.3 Fractional Lévy motion

Another famous model contained by the fractional Langevin equation is fractional Lévy motion (fLm) [89]. fLm corresponds to the choice of exponent $\alpha < 2$. In that case, the propagator of Eq. 3.5 takes the form of a symmetric Lévy distribution [94]:

$$P^{\text{fLm}}(x,t|x_0) = t^{-H} L_{\alpha,\sigma^{\text{fLm}}}\left(\frac{x-x_0}{t^H}\right) \tag{3.9}$$

with scale factor σ^{fLm} defined as

$$\sigma^{\text{fLm}} = \sigma_{\xi_\alpha}\left[(\alpha H)^{1/\alpha}\Gamma\left(H+1-\frac{1}{\alpha}\right)\right]^{-1}, \tag{3.10}$$

being σ_{ξ_α} the scale factor of the noise Lévy distribution. Since all moments of order α or larger are now infinite, a characteristic length for transport is no longer present. However, any moment of order $\mu < \alpha$ is still finite, scaling as

$$\langle (x-x_0)^\mu \rangle \propto t^{\mu H}, \tag{3.11}$$

where μ need not be integer. Following fBm conventions, the scaling $H = 1/2$ is still referred to as a diffusive scaling, although dynamics are neither Markovian nor Gaussian since $\alpha < 2$. It is also customary to keep using the term subdiffusion if $H < 0.5$ and superdiffusion if $H > 0.5$.

It turns out that the dynamics of fLm are Markovian only if $H = 1/\alpha$ (i.e., $\beta = 1$), since the temporal derivative in Eq. 3.6 disappears and the evolution of the particle would then only depend on the information of the local history. In this case τ_c is finite but v_c cannot be defined because the velocities are distributed according to Lévy statistics with tail-index α, that lack a finite variance. If $H \neq 1/\alpha$, on the other hand, the process is not Markovian and future motion of the particle depends on their previous history. This is in fact the more general case of fLm, in which neither a finite v_c nor a finite τ_c can be defined.

3.2 Characterization of the nature of transport in turbulent simulations using propagators.

It is possible to use the properties of fLm to characterize the nature of radial transport in our GENE simulations. The idea is to estimate the fractional exponents α and H that best describe the features of the radial transport driven by turbulence. The first method we will use relies on the use of the propagators just discussed. There are various ways to do this that have been discussed in the literature [1, 95, 96]. But in our case, based on what was described in the previous section, we will use the tails of a numerical estimation of the propagator of the process to get α, and the rate at which the finite moments (i.e., those of order less than α) of the numerical propagator grow over time to provide an estimate for the exponent H.

In order to use this method, we need to build a numerical approximation of the propagator of the transport process. To do this, we need a code capable of advecting and tracking particles in the presence of the turbulence. That is, a code that integrates the trajectories of individual particles as they are advected by the turbulence and, possibly, any other relevant process that affect their motion. The code that we have developed to carry out this task, TRACER, will be described in Chapter

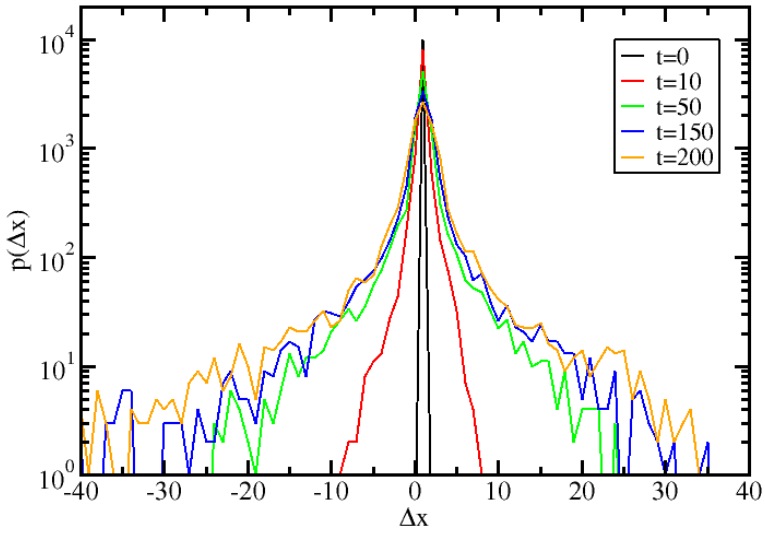

Figure 3.1: Snapshots of the numerical propagator, shown in log-lin scale, obtained by tracking 10^4 particles as they are advected by the turbulence generated by GENE at the radial position $s_0 = 0.10$ of the selected QPS configuration.

4. Assuming that such a code is available, a numerical approximation of the propagator could be easily obtained if one initially distributes a collection of particles randomly in all directions except along the direction of study (the radial direction in our case), in which particles are concentrated instead at the same position. The temporal evolution of this population will provide estimates of the propagator of the process at later times. In order to be able to extend the particle trajectories as long as possible, the particles are located at the centre of the (radial) domain. It is also evident that, in order to approximate the initial delta-function condition as much as possible and keep a good resolution during the temporal evolution, as many particles as possible should be used. In our runs, we have always tracked populations of at least $10^4 - 10^5$ particles.

The process is illustrated in Figure 3.1 for one of the GENE simulations of the QPS configuration selected for this thesis. After the initial-

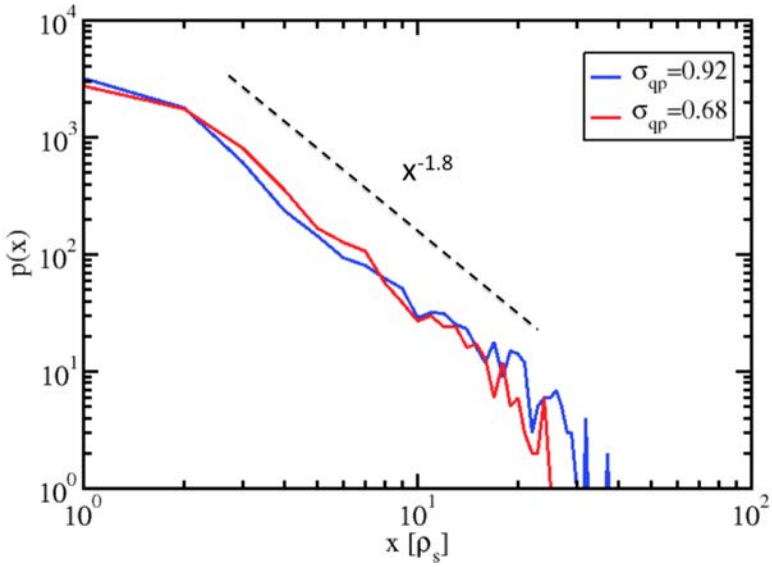

Figure 3.2: Positive tail of the estimated radial propagator (log-log scale) calculated in the neighbourhood of the magnetic surfaces located at $s_0 = 0.10$ and $s_0 = 0.63$. The propagator tail scales as $P(\Delta x) \sim |\Delta x|^{-(1+\alpha)}$, from which $\alpha \sim 0.8$ is inferred.

ization phase, all tracked particles are advected by the velocity field calculated from GENE 's turbulent fields. This advection causes the spreading of the propagator across the (radial) domain, as shown in the figure. It is also seen that the central peak gets lower and flatter and the propagator develops long fat tails reminiscent of those of Lévy distributions.

If non-diffusive transport is indeed at work, it is expected that the tails of the numerical propagator should behave like $P(\Delta x) \propto |\Delta x|^{-(1+\alpha)}$ at sufficient long times. Then, it is very easy to estimate α just by fitting the tail of the distribution to a power law. Fig. 3.2 illustrates the method for two different QPS simulations. Both of them yield similar values for the exponent, that is $\alpha \sim 0.8$. The picture also shows the typical shape of the propagators in log-log scale. There are often (at least) three distinct regions. A first one where the propagator is almost flat, at the smallest values of the argument; a second region, where the power law we are interested in (if it exists) is clearly manifested. And, finally, a third region, at the largest values of the argument, where the statistics get very poor and the tail is often truncated. Regretfully, the extend of the second region

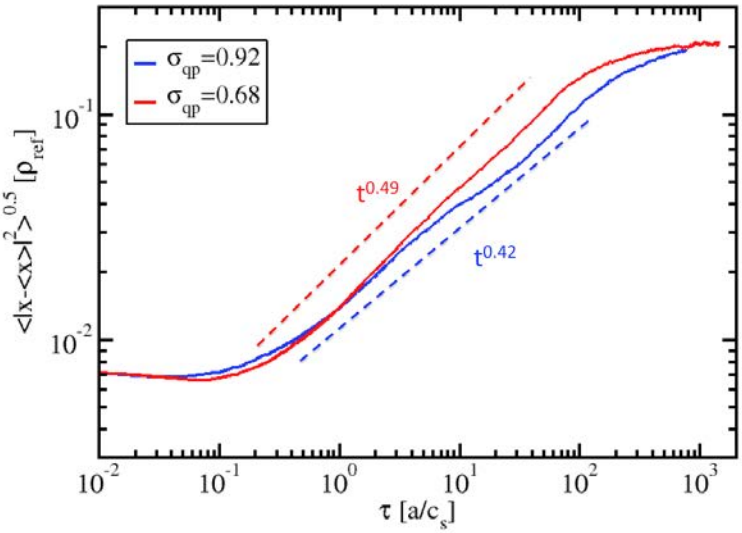

Figure 3.3: Fractional standard deviation as a function of time (in log-log scale) for two different QPS simulations. In red, results are shown for the simulation run around the magnetic surface $s_0 = 0.63$; in blue, around $s_0 = 0.10$.

is less than a decade in the example shown in Fig. 3.2, which is a tad too short to reliably determining α. This is also the case in the majority of our GENE simulations. We will discuss the reasons and consequences of this fact in detail in Chapter 5.

In order to estimate the Hurst exponent using the numerically estimated propagators, a fractional version of the standard deviation is calculated [1]. At any finite time, the fractional standard deviation is then defined as:

$$\sigma(t) = \left[\int |x - x_0|^{\mu} P(x,t) dx \right]^{1/\mu}, \quad \mu < \alpha, \tag{3.12}$$

where it is assumed that the propagator is symmetric. By comparing this fractional standard deviation growth with Eq. 3.11, one can estimate the exponent H simply by fitting $\sigma(t)$ to the power law t^H. This is illustrated in Fig. 3.3 for the same simulations used in Fig. 3.2. Again, Fig. 3.3 also

serves to illustrate the (at least) three regions that typically appear in these curves. First, a flat region at the smallest time lags (of the order of a few turbulence decorrelation times), followed by a power-law region (if it exists) that is the one relevant for the current analysis. At much longer time lags, the scaling is again usually lost, in most cases due to finite-size effects or lack of statistics.

3.3 Characterization of the nature of transport in turbulent simulations using Lagrangian velocities.

The second method that is used in this thesis is based on the characterization of the statistics and the correlations of the component of the (Lagrangian) velocity of tracked particles along the direction of interest [97, 98]. By comparing the results with what is expected for fLm, one can easily estimate both α and H.

Again, we will need a particle tracking code such as TRACER. The particles to be tracked must now be uniformly initizalized in all directions throughout the computational box. The radial (Lagrangian) velocity of the tracked particles, in GENE internal coordinates, is computed at any given time as:

$$v^r = \frac{v^x}{|\mathbf{e}^{\mathbf{x}}|} = \frac{v^x}{\sqrt{g^{xx}}}. \tag{3.13}$$

The reason why one needs to use this expression is that the velocity that GENE outputs, v^x, is the radial contravariant component of the particle velocity. Since the coordinate system GENE uses is not orthonormal, the x-component must be divided by the length of the proper contravariant basis vector, $|\mathbf{e}^{\mathbf{x}}| = \sqrt{g^{xx}}$ to yield the actual radial velocity.

The procedure to follow to estimate the exponents, in this case, goes like this. If radial transport does lack any characteristic scale, the probability density function (pdf) for the radial velocities of the tracked particles should then follow a symmetrical Lévy distribution. Therefore, the fractional exponent α can be estimated from the tail-index of the pdf of the component of the velocity along the radial direction on the limit of $v \to \infty$. Or, in other words, by quantifying whether the pdf of these velocities decays (or not) as a power law $p(v) \sim |v|^{-(1+\alpha)}$ for large

values of $|v|$. Taking into account that each tracked particle is statistically independent of any other, the results are greatly improved by calculating a normalized histogram that includes the velocity components of all tracked particles at many different times.

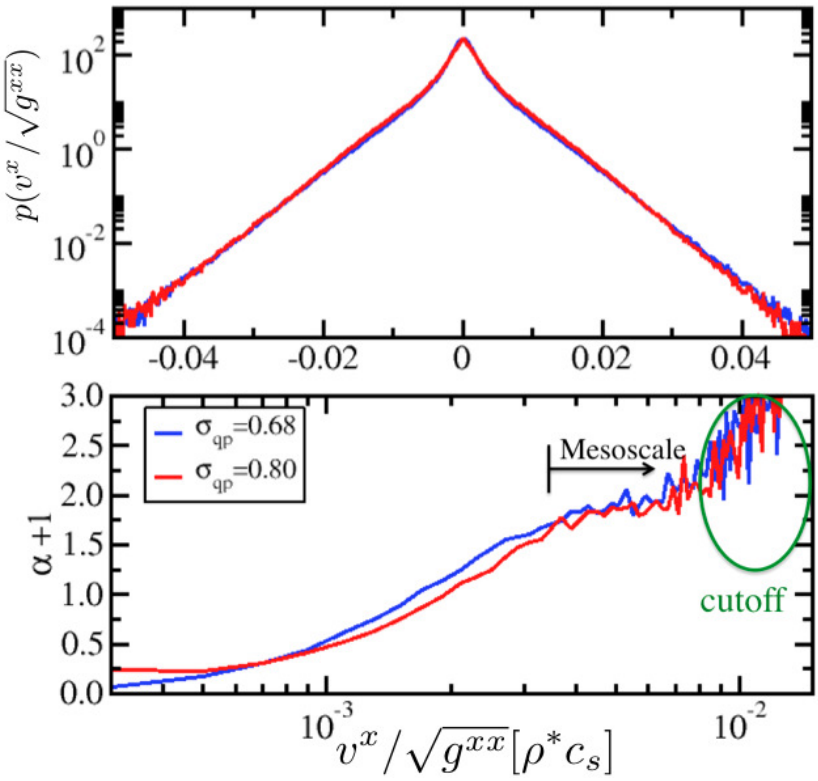

Figure 3.4: Above: pdfs of the Lagrangian radial velocities (in log-lin scale); the blue curve corresponds to 10^4 tracked particles advanced in the turbulence calculated around the surface $s_0 = 0.32$, where the quasi-poloidal symmetry ratio is $\sigma_{qp} = 0.80$; the red one, to tracked particles advanced around the surface $s_0 = 0.63$, where $\sigma_{qp} = 0.68$. Below: instantaneous tail exponent (see Eq. 3.14) for the two pdfs. The start of the mesoscale range is marked with a vertical line and an arrow.

The procedure is illustrated in Fig. 3.4 using 10^4 tracked particles advanced in the same turbulence used for Figs. 3.2 and 3.3. In the upper frame, the pdfs of the radial velocities are presented in log-lin scale.

In order to better estimate α, we also calculate their instantaneous tail exponent, that is defined as,

$$\alpha(v) = -\left(1 + \frac{v}{p(v)}\frac{\mathrm{d}p}{\mathrm{d}v}\right), \tag{3.14}$$

and that is shown in the lower frame of the same figure. The mesoscale region, over which $\alpha(v)$ is roughly constant, is used to determine the value and range of validity of the exponent. Regretfully, as it is apparent from the figure, an exponential cutoff appears for the simulated data at the larger values of v which limits significantly the mesorange. All the simulations done with GENE exhibit a similar behaviour. The origin of the cut-off is still not well understood. The implications of its existence will be discussed in Chapter 5.

To estimate the Hurst exponent, on the other hand, we use a simple variation of the popular rescaled-range analysis or [R/S] method, introduced by H.E. Hurst in the 50s to quantify memory in Gaussian-distributed time series [99]. The [R/S] analysis is a statistical measure which quantifies the type of correlation present in a long series of data at different timescales by comparing its properties to fBm (or in our case fLm). Assuming a time series V_k, $k = 1, 2, \cdots N$, Hurst's original prescription required the computation of the rescaled range:

$$[R/S](\tau) := \frac{\max\limits_{1\le k\le\tau} W(k,\tau) - \min\limits_{1\le k\le\tau} W(k,\tau)}{\sqrt{\langle V^2\rangle_\tau - \langle V\rangle_\tau^2}}, \tag{3.15}$$

with

$$W(k,\tau) := \sum_{i=1}^{k} V_i - k\,\langle V\rangle_\tau\,. \tag{3.16}$$

Here, $\langle\cdot\rangle_\tau$ represents the temporal average up to time τ. When the signal resembles fBm, then $[R/S] \sim \tau^H$, with H being the Hurst exponent. The prescription must however be slightly modified [97, 98] to deal with fLm, due to the divergent nature of its variance. In those cases, the denominator of the rescaled-range is replaced by the fractional standard deviation. It is useful to introduce the instantaneous Hurst exponent as a function of the [R/S],

$$H(\tau) := -\frac{\tau}{[R/S](\tau)}\cdot\frac{\mathrm{d}[R/S]}{\mathrm{d}\tau}(\tau) = -\tau\cdot\frac{\mathrm{d}\ln[R/S]}{\mathrm{d}\tau}(\tau), \tag{3.17}$$

that is used to determine the range of scales where H is well defined. They will appear as flat regions in the instantaneous Hurst exponent.

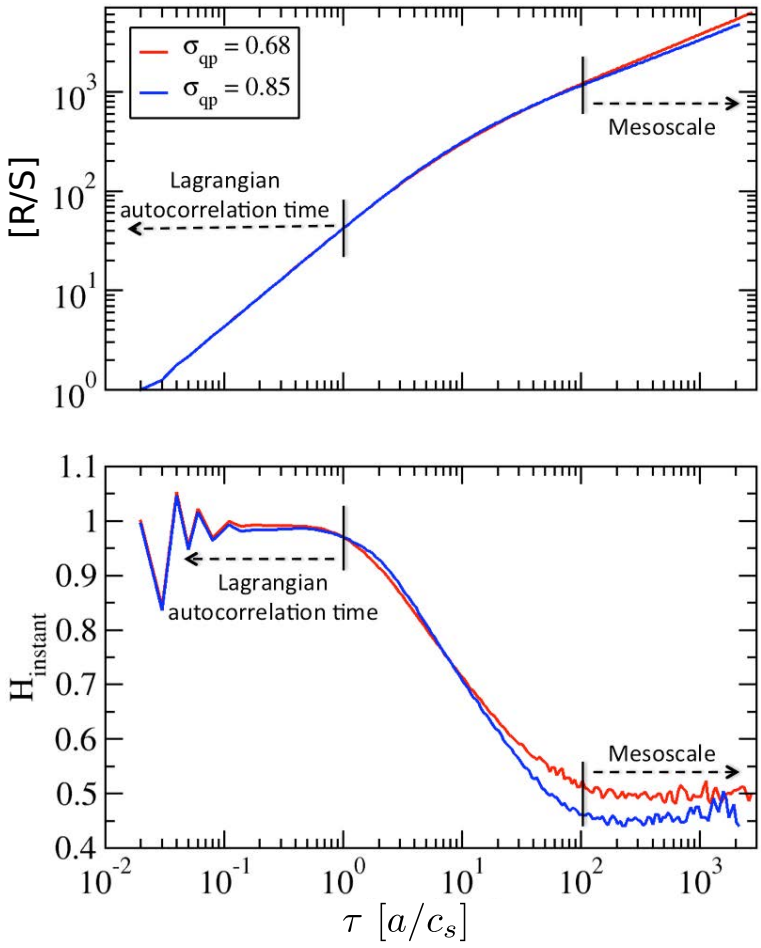

Figure 3.5: Above: rescaled range (i.e., $[R/S]$) as a function of time delay for two time series of radial Lagrangian velocities; the blue one comes from a tracked particle advected by the turbulence computed by GENE around $s_0 = 0.22$ where the quasi-poloidal symmetry ratio is $\sigma_{qp} = 0.85$; the red one, from a tracked particle advected in the turbulence calculated around $s_0 = 0.63$, where $\sigma_{qp} = 0.68$. Below: instantaneous Hurst exponent (Eq. 3.17) for the same two series. The auto-correlation and mesoscale ranges are marked with vertical lines and arrows.

As a final remark, it is worth saying that we remove any dependence on the initialization of the tracked particle from H by averaging the rescaled range function over all tracked particles. The procedure is illustrated in the Figure 3.5, where the results of performing the [R/S] analysis on time series of the Lagrangian radial velocity for the same two QPS simulations are shown. The shape of the $[R/S]$ function in this figure is rather typical. With a first range at the lowest time lags in which $[R/S] \sim \tau$ (ballistic regime) that gives a rough estimate of the Lagrangian auto-correlation time. For the cases shown, it is roughly $\tau_L \sim 10\ a/c_s$. At longer scales, about $\tau > 10^2 a/c_s$, is where the mesorange dynamics appear in the form of a second power-law range. It is the exponent, in this second region, the one which corresponds to the Hurst exponent. The figure shows two different cases, one for a tracer advanced in the turbulence calculated at $s_0 = 0.63$ ($\sigma_{\mathbf{qp}} = 0.68$) in which $[R/S] \sim \tau^{0.49}$, mildly subdiffusive (in particular, since R/S is known to somewhat overestimate H, yielding $H \approx 0.55$ for a random signal [100]), and a second one advanced at $s_0 = 0.22$ ($\sigma_{\mathbf{qp}} = 0.85$) where $[R/S] \sim \tau^{0.45}$, that is distinctly subdiffusive.

Chapter 4

The TRACER code

The two techniques that we have used in this thesis to characterize the nature of transport, discussed at length in Chapter 3, both require the detailed knowledge of the trajectories that individual particles follow as they are advected by the turbulence. Regretfully, advecting particles within modern Vlasov gyrokinetic codes is not a trivial task due to their large computational cost and their sophisticated but fragile parallel optimization [101]. As a result, the most straightforward way to carry out this type of studies –namely, to include the tracked particle evolution within the normal Vlasov-Poisson time-stepping– is not very practical. Nonlinear gyrokinetic simulations are highly parallel, with a lot of communication, and are very expensive to run. Including particle tracking inside a code like GENE would require a major overhaul of the code in order to maintain its internal balance for optimal parallelization and performance. In addition, every time that a different tracked particle initialization is needed, the whole gyrokinetic simulation would have to be rerun, thus incurring in a huge waste of computational resources. This last fact becomes even worse when considering that it is often convenient to use different tracked particle initializations with the same background turbulence. For all these reasons, we have developed our own external particle tracking code, TRACER, that is able to advance massless and massive particles in the turbulence that GENE calculates, once all necessary information has been read from the files generated by the gyrokinetic code. The main features of TRACER are described in this chapter.

4.1 Equations of motion for tracked particles

The TRACER code we have developed can integrate in time the trajectories of two types of particles: i) massless, neutral tracer particles and 2) massive, charged particles. The user will be prompted at run-time about the type of particle to be considered and TRACER will choose the proper equations to integrate accordingly. We discuss briefly these equations next.

4.1.1 Equations of motion in vector form

The equation that is integrated in time, for each particle tracked, is the one that expresses the Lagrangian velocity of the particle as:

$$\dot{\mathbf{r}} = \mathbf{v}_{E\times B} + \mathbf{v}_{Magn} + v_{\parallel}\frac{\mathbf{B}}{B}. \tag{4.1}$$

That is, it includes all the important drifts that need to be considered in a magnetically confined plasma. In particular, the $\mathbf{E}\times\mathbf{B}$ turbulent drift, the magnetic drift and the parallel motion [27, 29]. The $\mathbf{E}\times\mathbf{B}$ turbulent drift is obtained, at every point, as:

$$\mathbf{v}_{E\times B} = -\frac{\nabla\tilde{\phi}\times\mathbf{B}}{B^2}, \tag{4.2}$$

where the fluctuating potential $\tilde{\phi}$ is the one computed by GENE and that must be read from previously existent files. The magnetic field $\mathbf{B}$ corresponds to the background field of the configuration of interest and is provided by the VMEC code, and then transformed by GIST as explained in Chapter 2.

When TRACER is pushing massive, charged particles, the magnetic drift velocity is given by the usual formula [27]:

$$\mathbf{v}_{Magn.} = \frac{mv^2}{2qB^3}\left(1+\frac{v_{\parallel}^2}{v^2}\right)\mathbf{B}\times\nabla B, \tag{4.3}$$

Parallel motion is also included by coupling to the parallel equation of motion,

$$\dot{v}_{\parallel} = -\frac{\mu}{m}\frac{\mathbf{B}\cdot\nabla B}{B}, \qquad \dot{\mu} = 0. \tag{4.4}$$

The parallel dynamics thus include a mirror term, opening up the possibility of causing particle trapping in the magnetic field, if the conditions are adequate (i.e., non-homogeneous magnetic field plus sufficiently low particle energy).

If TRACER is pushing instead massless, neutral tracers, the magnetic drift velocity vanishes and $\dot{v}_\parallel = 0$. Thus, no real parallel dynamics are included for massless particles. Or, in other words, $v_\parallel$ is kept constant and equal to its initial value for all tracers. Therefore, tracers simply follow the trajectory dictated by the local $\mathbf{E} \times \mathbf{B}$ turbulent drift, in addition to their steady parallel motion. In fact, the characteristics of the $\mathbf{E} \times \mathbf{B}$ flow can be calculated by using massless tracers with $v_\parallel = 0$.

4.1.2 Equations of motion in GENE internal coordinates

The general equations of motion given in the previous section must, however, be made explicit in GENE internal coordinate system in order to be usable by TRACER. That is, we need to express them in the (x, y, z) field-aligned coordinates that were described in Chapter 2. We will not go through the long, but straightforward, algebra required for their derivation. Instead, we provide the final result, together with an explanation of their meaning.

After neglecting terms of order ρ^* and higher (which is consistent with how the gyrokinetic equation is derived within GENE), the vectorial Eq. 4.1 reduces to three equations, given by[1]:

$$\frac{d\hat{x}}{d\hat{t}} = \hat{v}^x_{E\times B} + \hat{v}^x_{\nabla B} + \hat{v}^x_c \tag{4.5}$$

$$\frac{d\hat{y}}{d\hat{t}} = \hat{v}^y_{E\times B} + \hat{v}^y_{\nabla B} + \hat{v}^y_c \tag{4.6}$$

$$\frac{d\hat{z}}{d\hat{t}} = \hat{v}_{T_j}(x_0)\hat{v}_\parallel \hat{b}^z \tag{4.7}$$

$$\frac{d\hat{v}_\parallel}{d\hat{t}} = -\frac{\hat{\mu}\hat{v}_{T_j}(x_0)}{2}\hat{b}^z \frac{\partial \hat{B}_0}{\partial \hat{z}} \tag{4.8}$$

These are the equations implemented within the TRACER code. We will start by discussing the parallel (i.e., z) equation. As previously

[1]Here, hats are introduced to remind that all quantities are normalized (see Chapter 2).

said, the evolution equation for the parallel velocity is only used if tracked particles possess mass. In the opposite case, the magnetic $\hat{\mu} = 0$ and $\hat{v}_{\parallel}$ is a constant, set by its initial value. Another important aspect to be noted is that $\hat{b}^z$ is the z component of the $\mathbf{b} = \mathbf{B_0}/B_0$ unit vector. If the GENE coordinate system was perfectly aligned, b^z would be one, since the direction of the field would be along z. However, as we discussed in Chapter 2, the fact that GENE forces the z direction to be periodic implies that the safety factor of the equilibrium field, $\mathbf{B}_0$, is not identical to that of the coordinate system. Then must be consistent with the number of points in the mesh, that must be connected to other points of the same mesh after z increases by 2π. As a result $\hat{\mathbf{b}}$ is not perfectly aligned with the z direction, and a $b^z < 1$ must be retained.

Regarding the equations along the directions perpendicular to the magnetic field, x and y, Eqs. 4.5 and 4.6 include first the turbulent $\mathbf{E} \times \mathbf{B}$ drifts, whose contravariant components in GENE coordinates are given by,

$$\hat{v}^x_{E\times B} = \frac{-1}{\hat{C}(x)}\frac{\partial \hat{\phi}}{\partial \hat{y}}; \quad \hat{v}^y_{E\times B} = \frac{1}{\hat{C}(x)}\frac{\partial \hat{\phi}}{\partial \hat{x}}. \tag{4.9}$$

Secondly, they also include the magnetic drift, that has been split in its two traditional contributions. A first one, associated to ∇B_0, is given by,

$$\hat{v}^x_{\nabla B} = \frac{\hat{\mu}\hat{T}_{0j}(x_0)}{\hat{q}_j\hat{C}(x)}\left(-\frac{\partial \hat{B}_0}{\partial \hat{y}_{eq}} - \frac{\hat{\gamma}_2}{\hat{\gamma}_1}\frac{\partial \hat{B}_0}{\partial \hat{z}}\right) \tag{4.10}$$

$$\hat{v}^y_{\nabla B} = \frac{\hat{\mu}\hat{T}_{0j}(x_0)}{\hat{q}_j\hat{C}(x)}\left(\frac{\partial \hat{B}_0}{\partial \hat{x}_{eq}} - \frac{\hat{\gamma}_3}{\hat{\gamma}_1}\frac{\partial \hat{B}_0}{\partial \hat{z}}\right). \tag{4.11}$$

whilst the second one, associated to the curvature of the field becomes:

$$\hat{v}^x_c = \frac{2\hat{v}^2_{\parallel}\hat{T}_{0j}(x_0)}{\hat{q}_j\hat{B}_0\hat{C}(x)}\left(-\frac{\partial \hat{B}_0}{\partial \hat{y}_{eq}} - \frac{\hat{\gamma}_2}{\hat{\gamma}_1}\frac{\partial \hat{B}_0}{\partial \hat{z}}\right) \tag{4.12}$$

$$\hat{v}^y_c = \frac{2\hat{v}^2_{\parallel}\hat{T}_{0j}(x_0)}{\hat{q}_j\hat{B}_0\hat{C}(x)}\left(\frac{\partial \hat{B}_0}{\partial \hat{x}_{eq}} - \frac{\hat{\gamma}_3}{\hat{\gamma}_1}\frac{\partial \hat{B}_0}{\partial \hat{z}} + \frac{\beta_{ref}}{2\hat{B}_0}\frac{\partial \hat{p}_0}{\partial \hat{x}_{eq}}\right) \tag{4.13}$$

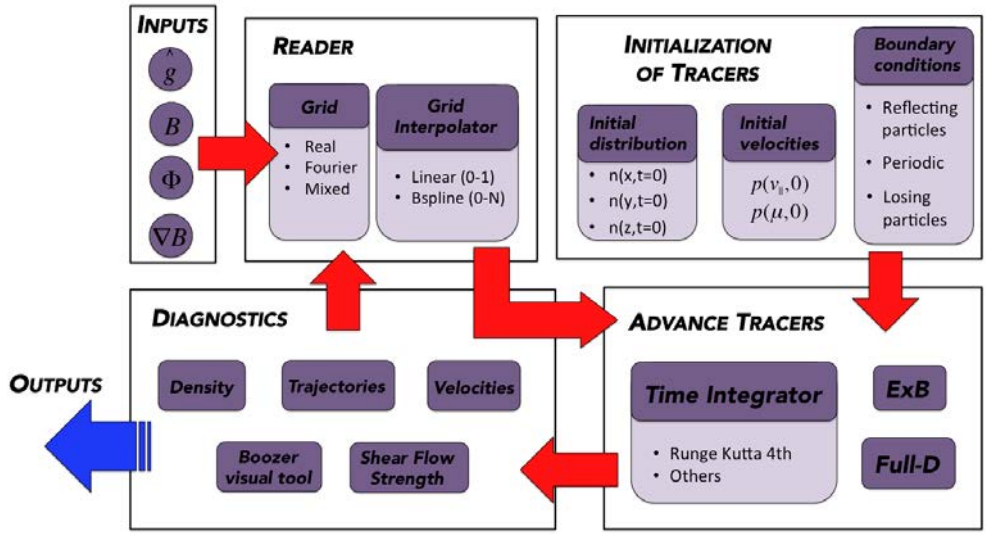

Figure 4.1: Scheme of the main modules of TRACER. Red arrows follow a typical iteration inside the code.

These equations must be completed with the definitions of some additional quantities, related to the metric elements and defined as:

$$\hat{\gamma}_1 = \hat{g}^{xx} g^{yy} - g^{xy} g^{yx}; \tag{4.14}$$

$$\hat{\gamma}_2 = \hat{g}^{xx} g^{yz} - g^{xy} g^{xz};$$

$$\hat{\gamma}_3 = \hat{g}^{xy} g^{yz} - g^{yy} g^{xz}. \tag{4.15}$$

Finally, the constant $\hat{C} = \hat{B}_0/\hat{\gamma}_1$ has also been introduced.

4.2 TRACER workflow

The workflow of a typical TRACER run is shown in Fig. 4.1. It comprises an initial phase where spatial and temporal fields are read from preexistent files (generated either by GENE or GIST); a second phase where the number and type of the particles to be tracked are selected and their positions and velocities initialized; a third phase where the temporal advance of all particles takes place; and a final phase where several diagnostics are used to monitor the run.

4.2.1 Interpolation of spatial fields

TRACER reads all the input information needed from files that GENE (or GIST) produces. Namely, the background magnetic field of the configuration of interest, the metric elements of the transformation to GENE internal coordinate system, and the temporal variation of the turbulent electrostatic potential field. All the field information on file is however given on GENE 's spatial (and temporal, in the case of the electrostatic potential) grid. The integration of the tracked particle trajectories requires that those fields are known along the particle trajectory, instead. To provide it, TRACER interpolates at any desired location by using either a linear or a B-spline scheme. Interpolation through B-splines has more accuracy but increase the time necessary for a simple iteration in a factor between $10 - 100$. In the case of non-varying-in-time quantities (such as the metric, or the magnetic field), all interpolation coefficients needed are calculated at the beginning of the run. The case of the turbulent electrostatic potential, that varies as time advances, must be handled differently.

4.2.2 Particle initialization

The various analysis methods discussed in Chapter 3 to characterize radial transport in this thesis (i.e., propagators, Lagrangian velocities, etc.) require different particle initializations, particularly along the x direction. For that reason, the TRACER code includes several possible initialization schemes. The two most used initializations are: i) uniformly distribution in x, y and z; and ii) localised around $x = x_0$, but uniform in y and z. The former initialization is the one needed for the application of the Lagrangian method. The latter, for the calculation of radial propagators.

Regarding the initialization of $v_\parallel$ and μ, it also depends on the problem being solved. In all the runs included in this thesis, we have always set $\mu = 1$. The initialization for $v_\parallel$ is done according to a Maxwellian distribution, $p(v_\parallel) \propto \exp(-m_i v_T^2 / 2k_B T)$, where the thermal velocity and temperature are set to those of the background plasma considered in the GENE simulation. In that sense, the motion of the tracked particles is brought closer to that of the thermal ions that would be confined in the magnetic configuration, in order to make the results of our analysis relevant for understanding their dynamics.

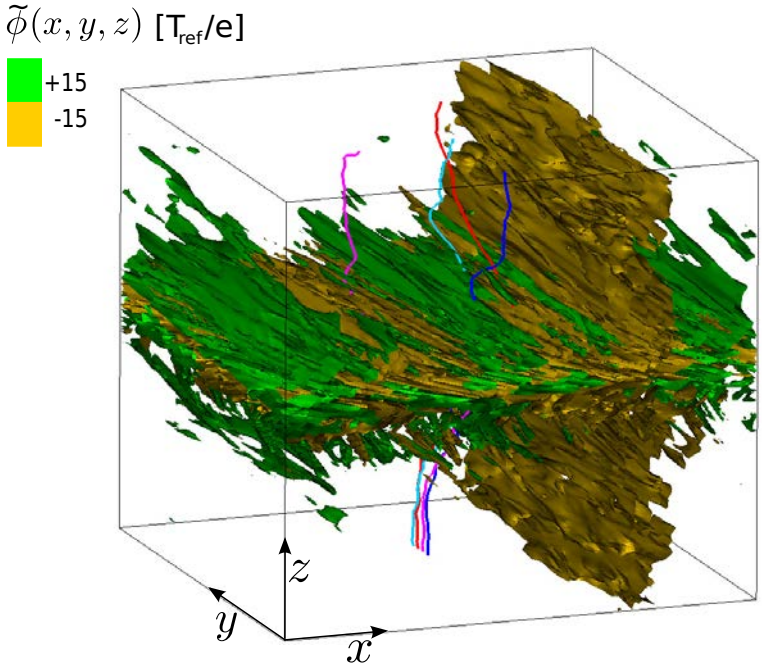

Figure 4.2: Trajectories of four different tracer particles (blue, red pink and dark-blue lines along z-direction) in the turbulent electrostatic field generated by GENE . The turbulent electric potential is also included by means of two of its isovolumes, one for a positive value (in green) and other negative (in yellow). The plot is presented in GENE internal coordinates (x, y, z). The vertical yellow structure of potential is associated with the zonal flow dynamics (remember that $z = \theta_B$).

4.2.3 Integration of trajectories

Typically, the number of particles tracked by the TRACER code ranges from a few tens of thousand to a few million. After the particles have been initialized according to the needs of the run, both in space (x, y and z) and velocity (namely, $v_\parallel$ and μ), they are advanced in time by the time integrator. Several integration schemes are available, although we have stuck to a 4-th order Runge-Kutta integrator [102] for all the calculations presented in this thesis. Depending on whether the particles being pushed possess mass or not, the integrator may include (or not) the evolution of the parallel velocity, as dictated by Eq. 4.4.

Each particle trajectory is clearly independent of any other, since

there is no interaction among the various particles. This is true both for massless and massive tracked particles. As a result, the TRACER code is easily parallelizable. This is done by distributing the particles among all available processors in a balanced way, which accelerates calculations almost linearly with the number of processors.

Several typical trajectories computed with TRACER, in this case for massless particles, are illustrated in Fig. 4.2 using GENE internal coordinate system. We use to visualize them one of the diagnostics included in TRACER. As it is apparent, the motion of the tracers happens mostly along z, where tracers basically free-stream. The structure of the electrostatic potential that advect them is also shown in the figure, by mean of several isovolumes of the potential, plotted in different colors.

4.2.4 Interpolation in time of the varying turbulent electrostatic potential

At this point, it is time to discuss how the problem with the time-varying turbulent electrostatic potential mentioned previously is handled by TRACER. On one side, TRACER requires the electrostatic potential value at the particular time instants required by the particle time advance algorithm. On the other side, the electrostatic potential is written in a GENE large file, as a series of snapshots with enough frequency to capture the whole dynamics. In general the time-step used in the TRACER time advance algorithm differs from the time-step used to write the snapshots in the GENE file. Time interpolation is thus required. In particular, TRACER estimates the potential at the required time instant using the closest (in time) four snapshots existent in the potential file. Then, from those snapshots, the value is obtained using third order spline interpolation [102].

4.2.5 Diagnostics

Once the integration of the particles trajectories has been carried for a prescribed amount of time, several types of output may be produced. Some of them are dictated by the needs of the analysis techniques used to characterize the nature of transport: the calculation of propagators (along the radial direction), and the analysis of radial velocity series along the Lagrangian trajectories of the flow, etc. These quantities are typically

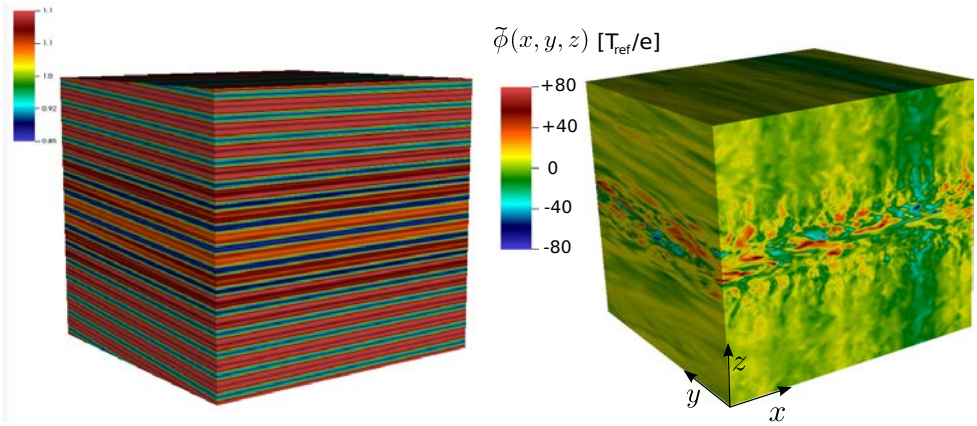

Figure 4.3: Volume colour plot of the magnetic field strength B (left) and turbulent electrostatic potential (right) shown in GENE coordinates (x, y, z). The fields have been taken from the GENE simulation carried out at the magnetic surface $s_0 = 0.10$.

written on file, in a format that facilitates its processing by other analysis tools (such as *Matlab*, *VisIt*, or various custom-made Fortran codes).

Other diagnostics that are also available are of the graphical kind and can be used to produce files (in either HDF5, Silo or text formats) that can be used to visualize (using, for instance, applications such as *VisIt* or *xmgrace*) either individual particle trajectories or to inspect the spatial (and maybe temporal) structure of all background and turbulent fields. Of particular interest are those diagnostics that allow to convert the different fields and their components from the internal GENE coordinate system to the Boozer coordinate system, or even to real space (see, as an illustration, Figs. 4.3-4.5, in addition to Fig. 2.7).

Among the various fields that can be looked at, the fluctuating electrostatic potential and its associated $\mathbf{E} \times \mathbf{B}$ drift are of particular interest to us. Specially, the radial shear of the poloidal component of the $\mathbf{E} \times \mathbf{B}$ drift that, as hinted in several parts of this thesis (see discussions in Chapters 2 and 5), is the most meaningful for the interpretation of results that refer to the nature of radial transport. As an illustration, Fig. 4.6 shows the evolution in time of the radial derivative of the poloidal angular velocity of the flow, defined by Eq. 2.27 (but without calculating the time average), that TRACER outputs at various magnetic surfaces of the QPS configuration.

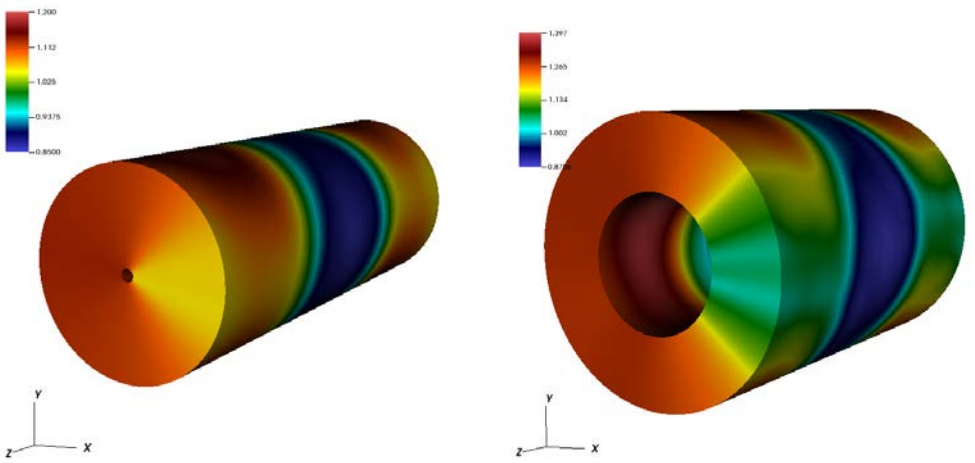

Figure 4.4: Volume colour plot of magnetic field strength B at two different radial surfaces, $s_0 = 0.10$ (**left**) and $s_0 = 0.63$ (**right**), shown in Boozer coordinates. Regions around $\theta_B = 0$ show a weaker B and a distortion of the quasi-symmetry (bad curvature effects). These effects are stronger in the external simulation (right).

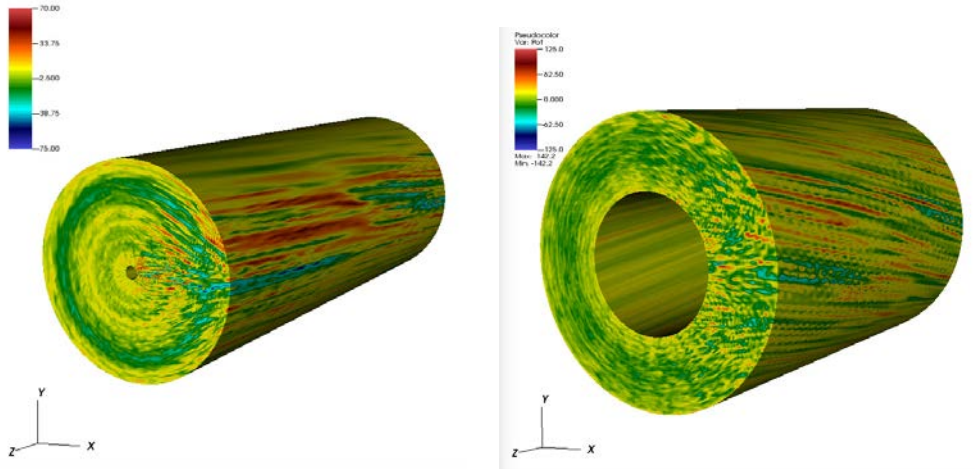

Figure 4.5: Volume colour plot of electrostatic turbulent potential Φ shown in Boozer coordinates for two different magnetic surfaces: $s_0 = 0.10$ (**left**) and $s_0 = 0.63$ (**right**). Regions around $\theta_B = 0$ show stronger turbulence effects. Radial shear flows are evident in both plots but in the left (internal) case is stronger.

As previously mentioned in Chapter 2, the radial shearing capability of the poloidal flow is positively correlated with the degree of quasi-poloidal symmetry, that decreases as one moves outwards in radius. This trend is clearly appreciated in the figure. At any rate, it is important to say that the TRACER code is very modular in its structure, and that adding any new diagnostics is extremely simple.

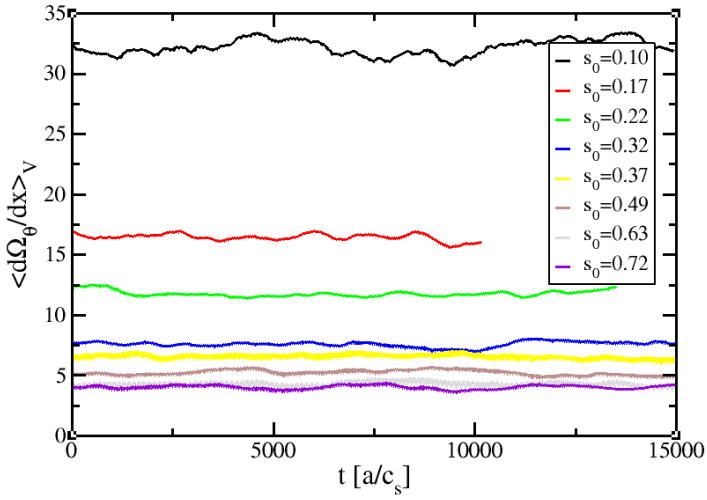

Figure 4.6: Radial sheared of the poloidal angular velocity of the $\mathbf{E} \times \mathbf{B}$, $< |\, \mathrm{d}\Omega_\theta / \,\mathrm{d}x| >_V$ (see Chapter 2, for a discussion on the significance of this quantity), as a function for the various of the QPS simulations discussed in this thesis.

4.2.6 Boundary conditions

An important point that we have not yet touched upon regarding particle trajectories is how they are treated when they reach the boundaries of the integration box. There are different options for the boundary conditions imposed on the tracked particles when their orbits reach the box limit. In GENE full-annulus simulations, all directions (x, y and z) are considered to be periodic. This does not necessarily mean, however, that tracked particles should also behave periodically. That is, that they should continue their trajectories through the boundaries as the periodicity dictates. The boundary condition imposed depends on what is it that we want those trajectories for. For instance, in order to calculate propagators along the

radial direction, it is convenient to assume that any particle that reaches any of the boundaries along the x-direction is considered as lost. If not, those particles will contribute to the propagator at shorter distances, instead of along the tail. This would distort the propagator, to the limit of render it useless after a significant number of particles has already crossed the radial boundaries. In the case of the Lagrangian method, it is also a problem to continue the orbits periodically, but for a different reason. The periodic continuation may misrepresent the type of long-term temporal correlation that we want to characterize.

In order to adapt to the various needs imposed by the transport analysis, TRACER allows to choose between three basic types of boundary conditions: *i) open boundary conditions, ii) reflecting boundary conditions, iii) periodic boundary conditions*. In the first case, particles are considered lost once they reach the boundary; in the second, the sign of the component of the velocity perpendicular to the boundary is reversed when the particle gets there; in the third one, the trajectory is continued as dictated by periodicity. Of course, different conditions can be imposed in different directions. In our case, the toroidal nature of the configurations require periodic conditions in y; the field-aligned nature of the coordinate system, periodic conditions in z; finally, we will always assume open conditions in the radial direction, x.

4.2.7 Timing

To give some idea of how long it takes to run TRACER, and in order to put it in context, it suffices to say that any of the nonlinear, full-annulus GENE simulations carried out in this thesis for the QPS configuration takes between three and four days to complete using 1024 processors. That duration does not include the amount of time needed to carry out convergence studies, both linear and non-linear (see discussion in Chapter 2). In comparison, the TRACER code can advance 10^4 tracked particles for a few tens of decorrelation turbulent times in the turbulent fields computed by GENE in just a few hours (depending on the spatial interpolation scheme selected).

A large contributor to the efficiency of the TRACER code is the parallelization. As previously mentioned, there is no interaction of the advanced particles among themselves. Therefore, the requested number of trajectories can be evenly distributed among the processes available, re-

ducing the computing time in roughly the number of processors. TRACER makes use of the MPI library of parallel subroutines to exchange information among the processors. Although further parallelization might be achieved by taking advantage of OPENMP subroutines to use the multiple CPUs per core available in many supercomputers, we have not implemented this option yet.

Chapter 5

Influence of quasi-poloidal symmetries on the nature of radial particle transport

5.1 Motivation

This chapter contains the main physics results of this thesis [40]. In it, we will investigate the changes on the nature of radial turbulent transport that may take place as a consequence of the presence of a certain level of quasi-symmetry in the underlying confining magnetic field. In particular, we focus our study on a selected configuration of the QPS device, that exhibits strong quasi-poloidal symmetry.

In electrostatic turbulence, the main contributor to particle radial motion is the $\mathbf{E} \times \mathbf{B}$ drift. In order to study the dynamics of this transport channel, it is convenient to examine first its Lagrangian properties by means of tracer particles. That is, particles without mass or charge that are simply advected by the $\mathbf{E} \times \mathbf{B}$ flow. These particles do not interact among them and do not modify any plasma field in their motion. Tracer transport is considered a good first approximation to simplify the study of the complete transport process, and it will be the first topic of discussion in this chapter.

After the Lagrangian properties of the $\mathbf{E} \times \mathbf{B}$ flow are characterized, we will proceed to study the dynamics of the transport of actual (gyro-averaged) ions, that naturally have both mass and charge. This means that, in addition to the $\mathbf{E} \times \mathbf{B}$ drift, magnetic drifts and dynamical

parallel motion need also to be considered. The comparison of the transport characteristics respectively obtained for tracers and massive ions will also be an important part of the results of this chapter.

The nature of transport (of either tracer or massive particles) will be characterized using the methodology described at length in Chapter 3. Namely, the determination of the transport (fractional) exponents H and α from the particles trajectories, calculated by theTRACER code that was described in Chapter 4. As it will be remembered, H measures the temporal correlation of the Lagrangian motion, while α measures its locality in space. Any values of H away from 0.5, or α smaller than 2 constitute evidence for non-diffusive behaviour, and of an associated fundamental change in the nature of transport dynamics. The reader should also refer to Chapter 2 to find an alternate characterization of the transport properties of the configuration examined here but using instead a more standard approach based on the computation of effective transport coefficients. The comparison of the more standard analysis with the methodology used here is indeed rather interesting.

We will determine the exponents α and H using two independent methods, both of them discussed in Chapter 3: Lagrangian analysis and propagators. This duality will allow us to provide more confidence in the results, as well as to benefit from the strengths and ameliorate the weaknesses intrinsic to each method.

5.2 Characterization of the nature of radial transport of tracer particles

In order to study the influence of the local degree of quasi-symmetry of the magnetic field, quantified by the σ_{qp} ratio (see Eq. 1.10), on the nature of radial transport, we have calculated a large number of tracer trajectories on a set of GENE simulations carried out at selected radial positions of the QPS configuration that was described in Chapter 2. Since the degree of quasi-symmetry decreases as we move radially outwards in this QPS configuration, this set of runs provide us with a sufficient variety of values for σ_{qp}. In Table 5.1, the different values of σ_{qp} at each surface examined have been collected, together with other quantities of interest (see Fig. 2.8). The range of σ_{qp} extends from 0.92 close to the axis of the configuration, to 0.65 at the outermost examined magnetic surface, that is located at

75% of the radius.

The number of tracer particles advected in the turbulence from each of the QPS simulations is around 10^4. Values for the fractional exponents α and H have been determined for each case using both the Lagrangian and the propagator methods (see Chapter 3 for a description of the methods).

s_0	$\sigma_{\rm qp}$	$\left\langle \left\lvert \frac{\mathrm{d}\Omega_\theta}{\mathrm{d}x} \right\rvert \right\rangle_V \left[\frac{c_s}{a\rho_s}\right]$	H_{RS}	H_{prop}	α_v	α_{prop}
0.10	0.92	31.87	0.42	0.42	0.81	0.76
0.17	0.91	16.52	0.43	0.42	0.77	0.79
0.22	0.85	11.65	0.44	0.43	0.83	0.81
0.32	0.80	7.59	0.45	0.44	0.85	0.80
0.37	0.78	6.55	0.46	0.45	0.82	0.80
0.49	0.73	5.12	0.47	0.47	0.85	0.82
0.63	0.68	4.27	0.48	0.49	0.87	0.85
0.72	0.65	4.02	0.50	0.50	0.88	0.87

Table 5.1: From left to right: magnetic surface s_0; quasi-poloidal symmetry ratio σ_{qp}; figure-of-merit for the radial shear capability of the zonal flow, $\left\langle \left\lvert \frac{\mathrm{d}\Omega_\theta}{\mathrm{d}x} \right\rvert \right\rangle_V$ (see Chapter 2); Hurst exponent estimated with the RS-method, H_{RS}; Hurst exponent estimated using the propagator method, H_{prop}; spatial exponent estimated from the pdfs of the radial velocity, α_v; spatial exponent obtained from the tail of the propagator, α_{prop}.

5.2.1 Hurst exponent H

The results obtained for the H exponent in the QPS runs as the quasi-poloidal symmetry ratio is varied are illustrated in Fig. 5.1 (and collected in Table 5.1). The values are very similar for the Lagrangian and the propagator methods, with no significant differences between them. It is apparent that $H < 0.5$ is found at all surfaces except for the outermost surface examined at $s_0 = 0.72$, that is also the less quasi-symmetric position. It is also clear that H and the quasi-symmetry ratio σ_{qp} are negatively correlated, with H decreasing as σ_{qp} is increased. Given the fact that the R/S-method, that we have employed to estimate H, is well-known to overestimate H by about a 5% (that is, a purely random signal typically yields $H \sim 0.55$ [100]), the obtained values for H suggest that radial turbulent

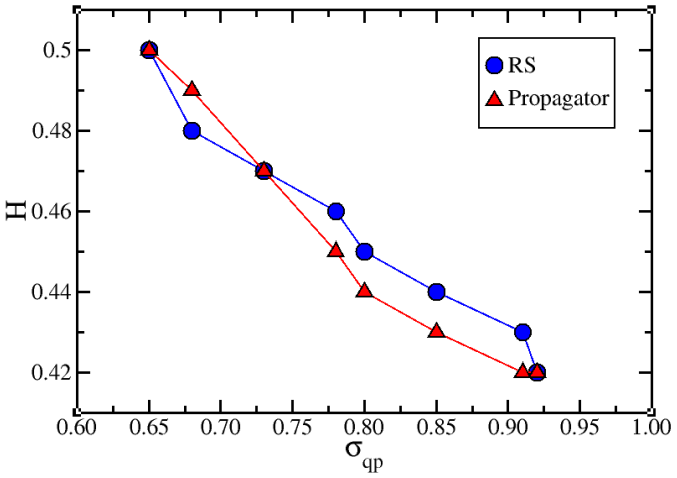

Figure 5.1: Hurst exponent values for radial tracer motion as a function of the degree of quasi-poloidal symmetry σ_{qs}. The blue circles represent values obtained with the *RS*-method; red triangles, with the propagator method.

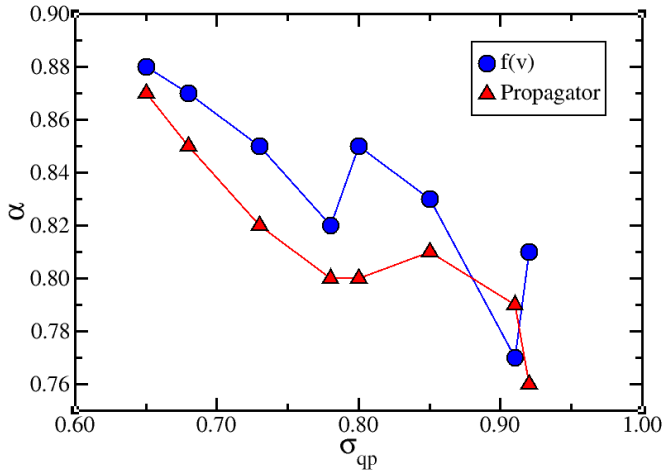

Figure 5.2: Spatial exponent α for the radial tracer motion as a function of the degree of quasi-poloidal symmetry σ_{qs}. The blue circles represent values obtained with the Lagrangian method; red triangles, with the propagator method.

transport is mildly subdiffusive in all locations. It becomes increasingly subdiffusive as one moves towards the centre of the configuration, where the degree of quasi-symmetry is larger. We will discuss our interpretation of this result and its physical meaning later, in the discussion subsection.

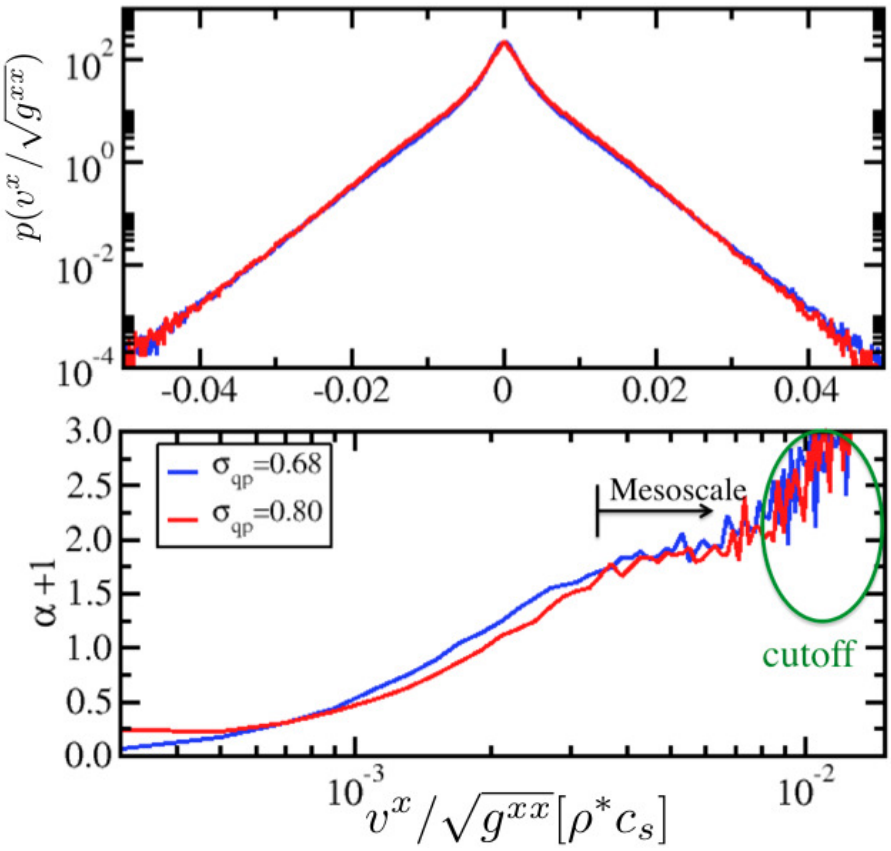

Figure 5.3: **Above**: pdfs of tracer Lagrangian radial velocities (in log-lin scale); the blue curve corresponds to tracers advanced in the turbulence calculated around the surface $s_0 = 0.32$, where $\sigma_{qp} = 0.80$; the red one, to tracers advanced around the surface $s_0 = 0.63$, where $\sigma_{qp} = 0.68$. **Below**: instantaneous tail exponent (see Eq. 3.14) for the two pdfs. The start of the mesoscale range is marked with a vertical line and an arrow.

5.2.2 Spatial exponent α

The values obtained in the QPS runs for the spatial exponent α are shown in Fig. 5.2 (and collected in Table 5.1) as a function of the degree of quasi-poloidal symmetry, σ_{qp}. As happened with the exponent H, the Lagrangian and propagator methods again coincide rather well, always yielding values of $\alpha < 1$. The maximum value, $\alpha \approx 0.9$, is reached at the magnetic surface with the lowest degree of quasi-poloidal symmetry (i.e., $\sigma_{qp} = 0.68$). The spatial exponent α is also seen to decrease softly as the degree of quasi-poloidal symmetry increases. It reaches its minimum value, roughly $\alpha \sim 0.8$, at the location of the innermost magnetic surface, where the degree of quasi-poloidal symmetry is the highest, $\sigma_{qp} = 0.92$.

Unfortunately, the estimation of the exponent α is not as clean as that of the Hurst exponent H. Any conclusions on the meaning of the obtained values for α, must thus be taken with a grain of salt. Fig. 5.3 shows the pdf of the radial Lagrangian velocities (above) and the instantaneous α exponent (below; see also Eq. 3.14). Clearly, the tail of the pdf becomes exponential too quickly. The same conclusion can be drawn from the instantaneous exponent, that exhibits just a short mesoscale of about half a decade (it is in this region that the values for α listed in Table 5.1 have been estimated), followed by an exponential cut-off. The shortness of the mesoscale severely limits the credibility of the obtained values, since one would like to have at least a decade long mesoscale.

The short mesoscale observed is not an artefact caused by the methodology used, though. In fact, the estimates obtained of α are similar to those that are obtained using more traditional (but less stringent, in our opinion) methods instead. For instance, Fig. 5.4 shows the result of fitting the survival function of the velocity pdf, $\mathrm{Sf}(V) = P[v \geq V]$, using an analytic function that includes an algebraic region of exponent α between scales v_1 and $v_2 \gg v_1$, followed by an exponential fall-off:

$$S_2(v) \sim \frac{A_2 \exp(-v/v_2)}{[1 + v/v_1]^{\alpha}}. \tag{5.1}$$

The survival function is particularly useful to examine the positive tail of the pdf (for the negative tail, the cumulative distribution function is used) [66]. Mainly, because an exponential pdf leads to an also exponential survival function; a pdf with an algebraic region scaling as $v^{-(1+\alpha)}$, on the other hand, leads to a survival function scaling as $v^{-\alpha}$ over

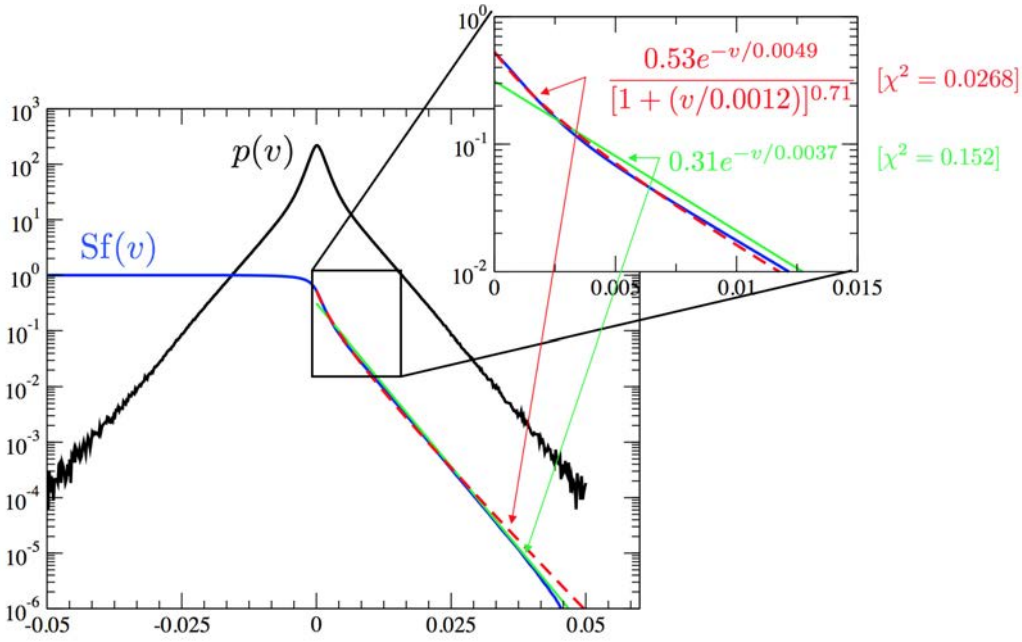

Figure 5.4: Determination of α by fitting the tail of the survival function $\mathrm{Sf}(V) = P[v \geq V]$ for the radial velocities at $\sigma_{qp} = 0.82$ against the analytical function defined in Eq. (5.1). A comparison to another fit using a purely exponential form, $S_1(v) \sim A_1 \exp(-v/v_0)$, is also included. Values of the χ^2 coefficients are also included to provide an estimate of the goodness-of-the-fit.

the same scales. Going now back to Fig. 5.4, it is clear that the range of scales over which α is roughly half a decade, followed by and exponential cutoff. In order to show that the power-law region, albeit limited, is meaningful, we have also included a purely exponential fit. The goodness-of-the-fit, measured by the standard χ^2 measure, is at least one order of magnitude lower if the power-law region is included.

We concede, however, that since the extension of the scaling region is limited to about half a decade, it is much less of what one would usually demand to show scale-invariance. In spite of that, we considered that the values of α obtained in the reduced mesoscale are still meaningful, and have included them in the discussion for the sake of clarity and completeness. They are significantly non-Gaussian, with $\alpha \sim 0.7 - 0.9$,

suggesting a mild decreasing trend with larger degrees of quasi-symmetry.

5.2.3 Analysis and discussion

The exponents H and α obtained from the analysis of the tracer radial motion in the previous subsections suggest that the fact that the effective ion heat conductivity χ_i is indeed reduced as the degree of quasi-poloidal symmetry σ_{qp} increases (see discussion in Chapter 2, including Fig. 2.8) is in itself far from providing the complete picture of what is happening with radial turbulent transport in the presence of strong quasi-poloidal symmetry of the underlying magnetic configuration.

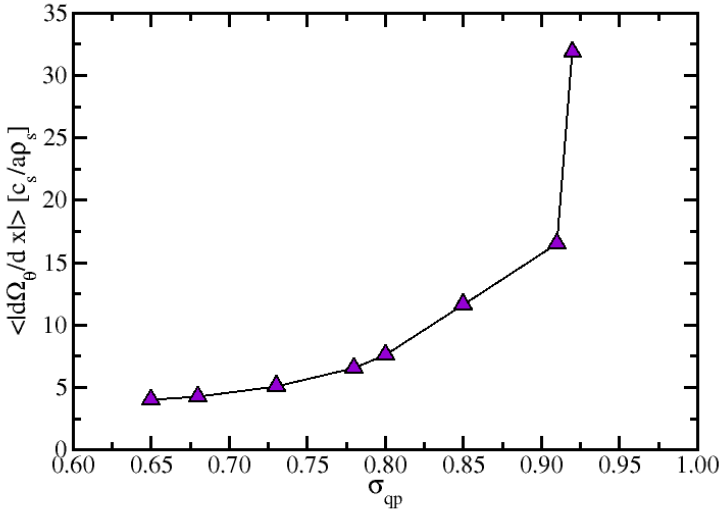

Figure 5.5: Variation of the radial shearing capability of the poloidal flow with the quasi-poloidal symmetry ratio σ_{qp} at the different magnetic surfaces where GENE simulations have been run.

The radial transport of tracers seems to manifest a clear subdiffusive character (i.e., $H < 0.5$) that becomes stronger as the degree of quasi-symmetry becomes larger. The reduction of the effective thermal conductivity has been shown by other authors to be positively correlated with an increase in the capability of self-generated radially sheared zonal

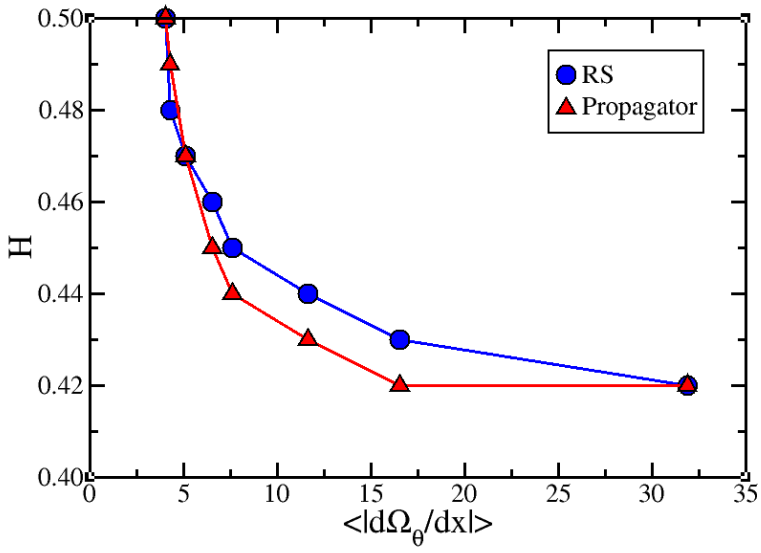

Figure 5.6: Variation of the Hurst exponent as a function of the radial shearing strength of the poloidal flow as characterized by due the figure of merit $< |d\Omega_\theta/dx| >$. The blue circles represent the values obtained with the Lagrangian method; the red triangles, with the propagator method.

flows to act and suppress the turbulence of the plasma [11]. In this case, however, the self-generated turbulent zonal flow in the poloidal direction is correlated to a larger degree of radial subdiffusion. This correlation can be made apparent, however, by characterizing the shearing capability of the flow by means of the figure-of-merit $\langle |\, \mathrm{d}\Omega_\theta / \,\mathrm{d}x| \rangle$ (defined by Eq. 2.27), that estimates the radial derivative of the local poloidal angular velocity, and therefore quantifies how strongly the poloidal flow can shear apart a radially correlated structure.

Fig. 5.5 shows the variation of the radial shearing capability of the poloidal flow with quasi-poloidal symmetry, as obtained by the TRACER code (the specific values have also been collected in Table 5.1). Clearly, it shows that the shearing capability increases for larger symmetry, thus confirming the role that the predicted reduced neoclassical poloidal symmetry plays in permitting the excitation by the turbulence of larger (and more sheared) poloidal flows [38]. The growth is clearly nonlinear with the degree of quasi-symmetry.

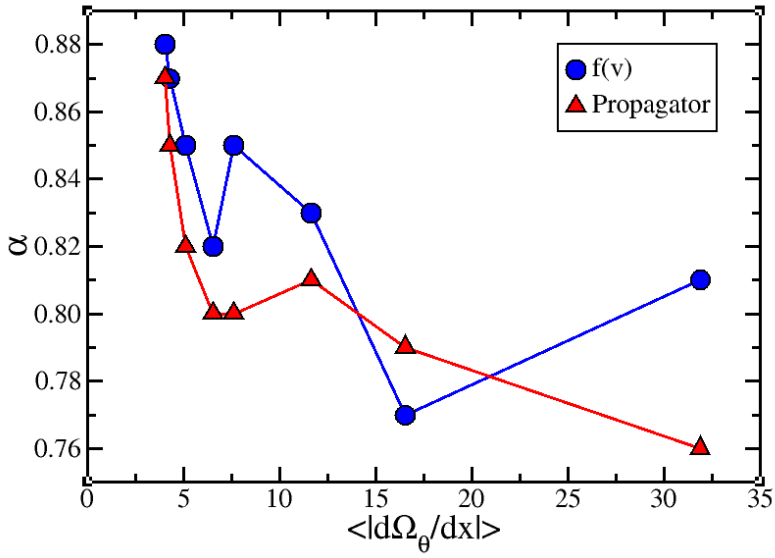

Figure 5.7: Spatial exponent α as a function of the radial shearing capability of the poloidal flow as characterized by due to the figure of merit $< |d\Omega_\theta/dx| >$. The blue circles represent the values obtained with the Lagrangian method; the red triangles, with the propagator method.

We proceed now to explore the connection between the subdiffusive nature of radial tracer transport and the radial shearing capability of the poloidal flow by plotting the exponents H and α as a function of the figure-of-merit, $\langle |\, \mathrm{d}\Omega_\theta / \,\mathrm{d}x| \rangle_{\mathrm{volume}}$. The result for H is illustrated in Fig. 5.6. Clearly, H is negatively correlated with $\langle |\, \mathrm{d}\Omega_\theta / \,\mathrm{d}x| \rangle_{\mathrm{volume}}$, implying that radial transport becomes more subdiffusive as the radial shearing capability of the poloidal flow increases.

This behaviour is very reminiscent of how radial transport was found to behave in recent gyrokinetic simulations of ITG tokamak turbulence that had strong radially-sheared poloidal flows [5, 6, 7]. In fact, most of the available numerical evidence points to the same physical mechanisms as the responsible ones for the subdiffusive radial transport observed here.

The physical mechanism for this process can be understood as follows. Any large positive [negative] value of $\langle |\, \mathrm{d}\Omega_\theta / \,\mathrm{d}x| \rangle_{\mathrm{volume}}$, whose generation via the Reynolds stresses is facilitated by the reduced neoclassical viscosity that a larger quasi-poloidal symmetry brings, causes a growth in extension and intensity of those regions with positive [negative] vorticity

together and a suppression of those with negative [positive] vorticity [7].

This process takes place in addition to the concomitant stretching along y and the shortening along x of any region of localised vorticity (along z) driven by the sheared rotation. The vorticity landscape that results from these processes makes it more probable for any radial motion to reverses its direction often, instead of moving steady, which automatically leads to the observed subdiffusion along x. This behaviour is insensitive to the sign of the shear, caring only about the shear absolute strength. This is what we observe here. More interestingly, tokamak simulations proved that the establishment of subdiffusion via this process does not require that the zonal flow be self-generated by the turbulence [5]. Transport would also become subdiffusive in the presence of externally driven flows, which suggests an interesting avenue to transport control via external biasing.

Regarding the non-Gaussian tails ($\alpha < 2$) found in the QPS simulations (see Fig. 5.7), their significance is not so clear. In previous tokamak gyro-kinetic simulations the values of the tail exponents found were much larger ($\alpha \sim 1.4 - 1.5$) and increased towards the Gaussian value (i.e., $\alpha \sim 2$) as the zonal flow shear strength decreased and transport became more diffusive [7]. This is not what we have found in the current GENE simulations for a quasi-poloidal geometry. Instead, $\alpha \sim 0.75 - 0.9$ and it seems to increase very weekly as the value of the quasi-poloidal symmetry ratio is reduced.

Due to problem with the limited size of the scaling region in the current simulations previously discussed, it is difficult to tell whether the different behaviour seen for the exponent α is caused by differences in the dominant physics caused by the geometry, or just because of factors related to the different numerical implementation used. The tokamak simulations were done with UCAN [103], a radially global, PIC gyrokinetic code. In contrast, GENE is Eulerian and radially local. Zonal flow dynamics could be quite different in these two setups due to the simplifications made in each of them, and might perhaps be the reason for the observed differences.

Be it as it may, it is our intention to further investigate this question in the near future, with a particular focus on the determination of which is causing the exponential cutoff found in the determination of α.

5.3 Characterization of the nature of thermal ion radial transport

In this section, the nature of the radial transport of actual thermal ions will be investigated. In contrast to the tracer case just described, the ion mass, charge and kinetic energy of the thermal ions is important to determine their motion. Both magnetic and curvature drifts, as well as parallel motion, are now important, which modifies the pure $\mathbf{E} \times \mathbf{B}$ approximation to motion that we considered in the previous section. The fractional exponents H and α have been determined using the same methodology as in the case of tracers. Namely, using the Lagrangian and propagator methods. The number of particles considered is very similar to the ones used for the tracer runs, including around $10^4 - 10^5$ ions.

5.3.1 Hurst exponent

It turns out that, for thermal ions, the values obtained for the exponent α barely change with respect to the ones obtained for tracers. They also have the same problem previously discussed of being well defined only over a very short mesoscale, less than a decade long. However, things become much more interesting with respect to the H exponent. This is illustrated in Fig. 5.8. The plot compares the instantaneous value of the Hurst exponent (Eq. 3.17) for three different types of TRACER runs carried out at the most quasi-poloidally symmetric position (that is, $s_0 = 0.10$ where $\sigma_{qp} = 0.92$). The red curve correspond to a tracer run in which the advection is done considering only the $\mathbf{E} \times \mathbf{B}$ drift. The green curve corresponds to the case of a thermal ion, thus including all magnetic drifts, on top of the $\mathbf{E} \times \mathbf{B}$ drift. The blue curve corresponds to an intermediate, academic case in which only magnetic drifts are kept, but with the $\mathbf{E} \times \mathbf{B}$ drift artificially set to zero.

The important thing to notice, when comparing the red and green cases, is that the long-term behaviour of the exponent (for $\tau > 10^2\ a/c_s$) seems to be very similar for thermal ions and tracers, remaining subdiffusive in both cases. However, there is a new intermediate range of scales for the thermal ions ($10 < \tau < 10^2\ a/c_s$), in which a clear superdiffusive plateau ($H \approx 0.7$) becomes apparent, that is absent for massless tracers. The same qualitative behaviour is observed at the other radial locations of the QPS configuration under study, although we have not included any

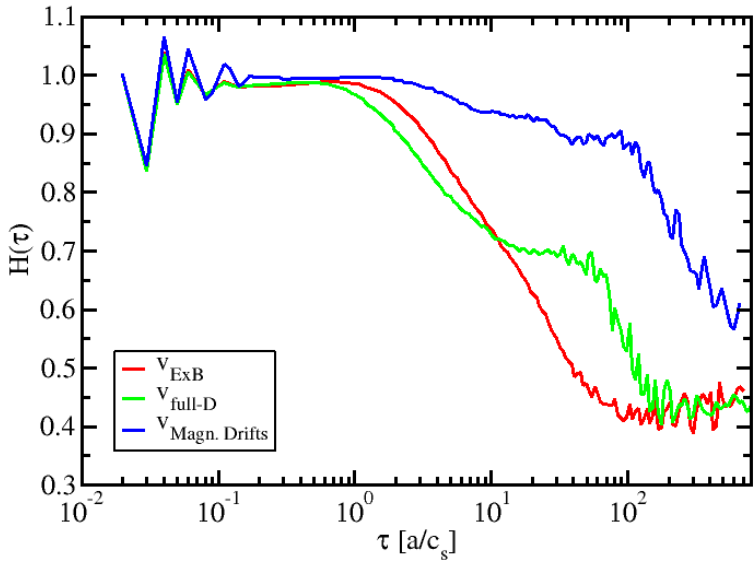

Figure 5.8: Instantaneous Hurst exponent as a function of time for three runs carried out at the same radial position ($s = 0.10$) with different schemes to advance particles. In red, the advecting velocity is just only the $\mathbf{E} \times \mathbf{B}$ drift. In green, the full dynamics are considered, including both ExB and magnetic drifts $\mathbf{E} \times \mathbf{B}$ and magnetic drifts. In blue, only magnetic drifts are considered.

additional plot. We will try to explain the physics behind this new scaling behaviour in the discussion section, with the help of the blue simulation included in Fig. 5.8 that considers only magnetic drifts.

5.3.2 Analysis and discussion

The very different behaviour of the H exponent found for massive ions and illustrated in Fig. 5.8 is indeed very interesting. We think that, in order to explain it, one needs to consider the spatial distribution of the sign of the radial component of $\mathbf{B} \times \nabla B$ that governs the magnetic drift of thermal ions. As it is shown in the left frame of Fig. 5.9 this sign is predominantly positive (i.e., red) for $z \in (0, \pi)$ and negative (blue) for

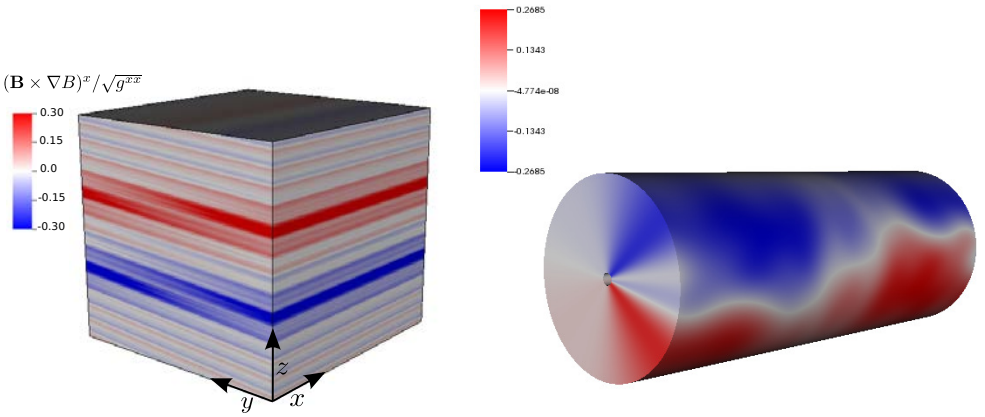

Figure 5.9: Variation of the radial component of $\mathbf{B}\times\nabla B$ across the computational volume centered at the magnetic surface $s_0 = 0.10$ (left, in GENE internal coordinates; right, in Boozer coordinates). Since $z = \theta_B$, the poloidal Boozer angle, the plot shows that massive particles are going to be pushed outwards in radius (i.e., to larger x's) when $z \in (0, \pi)$, and then inwards (to smaller x's) while $z \in (-\pi, 0)$, as they move along the field line. These ballistic processes are responsible for the superdiffusive behaviour made apparent in Fig. 5.8.

$z \in (-\pi, 0)$. Since z corresponds to the Boozer poloidal angle, this up-down asymmetry pushes massive ions radially outwards in the upper half of the configuration, and radially inwards in the lower half. But since z also represents the label that runs along any magnetic field line, massive ions feel these effects alternatively as they move along the field lines due to the relatively large safety factor. This behaviour is visually more evident in the right frame of Fig. 5.9, where the radial $\mathbf{B}\times\nabla\mathbf{B}$ component is plotted now in Boozer coordinates. It is clear that, in the upper part of the device, the magnetic drift has a negative sign, while it is positive on the lower part.

As a result of the spatial structure of the magnetic drift in the QPS configuration, the radial motion is endowed of a ballistic component that governs the scaling of radial transport in the intermediate range $(10-10^2)a/c_s$ as was apparent in Fig. 5.8. This is illustrated by the blue curve in that figure, that only considers magnetic drifts and parallel motion for the massive ions. When the contribution to perpendicular motion of the turbulent $\mathbf{E}\times\mathbf{B}$ is also included, as shown by the green curve in Fig. 5.8,

turbulent decorrelation begins to dominates for timescales $\tau > 10^2\ a/c_s$, beyond which the radial motion of massive ions becomes very similar to that of the massless tracers. In this regime, the temporal correlations start to be dominant. The final result is a radial motion that becomes more subdiffusive when the quasi-poloidal symmetry ratio is larger.

Chapter 6

Conclusions and Future Work

In this thesis, we have investigated how the nature of radial transport, and the improved confinement that should follow from it, depends of the level of quasi-symmetry in quasi-poloidal symmetric stellarators. To provide answers in this respect, we have used the GENE gyrokinetic code to produced nonlinear simulations of electrostatic, ITG turbulence around specific magnetic surfaces of a quasi-poloidally symmetric configurations. The resulting radial transport has then been investigated by means of tracked particles (massless and massive) that are advected in the presence of the ITG turbulence by a new code, TRACER. The main conclusions of the investigation as well as future lines of research are listed below.

6.1 Conclusions

1. Radial turbulent transport is reduced as the quasi-poloidal symmetry is increased.

We have demonstrated for the first time that radial turbulent transport is reduced as the level of quasi-poloidal symmetry, measured through σ_{qp}, is increased. By following first a traditional analysis, we have shown that the effective ion heat conductivity is reduced as σ_{qp} is increased. We have also shown that transport is negatively correlated with the radial shearing capability of the poloidal flow, which grows with σ_{qp} due to the smaller poloidal viscosities predicted by neoclassical theory [10, 38]. Our studies thus complete a series of previous studies carried out by other authors for other quasi-symmetries. In particular, for quasi-helical symmetry [9] and

quasi-axisymmetry [87], where a positive correlation between good confinement and the level of these types of quasi-symmetry was also reported.

2. Quasi-poloidal symmetry affects the nature of radial turbulent transport by making it become subdiffusive. The radial shear in the poloidal flow whose development quasi-poloidal symmetry facilitates is the key for this change in transport dynamics.

We have shown that the Hurst exponent that describes both tracer and thermal ion radial transport becomes increasingly subdiffusive (i.e., $H < 0.5$) as the degree of quasi-poloidal symmetry increases. Therefore, it is not that confinement becomes better because the effective turbulent conductivity is reduced due to shear-flow suppression, is that the nature of radial transport itself changes to one that leads to better confinement. Again, the reason for this behaviour must be sought in the increased ease with which poloidal flows with strong radial shear may be excited due to the reduced neoclassical viscosity associated to the quasi-poloidal symmetry. The dynamics of transport across the flow are similar to what has been previously observed in tokamaks in the presence of strong radially-sheared zonal flows [5, 6, 7].

3. Thermal ions behave very similar to tracers in terms of radial transport for sufficiently long times.

Our analysis at the end of Chapter 5 has also shown that long-term radial transport dynamics is rather similar for tracer and massive ions. Differences appear, however, at intermediate scales due to the action of the magnetic drifts in a magnetic configuration that is spatially dependent. This realization is important, since it implies that the conclusions drawn from our tracer studies are relevant at least to understand qualitatively long-term ion transport.

4. Transport dynamics seem to be non-Gaussian but quantitative evidence is still inconclusive.

All the methods used in this thesis point to non-Gaussian velocity statistics and non-local spatial behaviour for radial turbulent transport in the QPS configurations. However, strong statements cannot be made about their significance due to the short mesorange over which such behaviour is clearly displayed. It is not clear to us what the reason is, since simulations with higher spatial resolution yielded similar results. It might be related with the type of zonal flow dynamics that are allowed by the fully-periodic, full-annulus local simulation we have done, but this is an aspect of the research that will be continued in the future.

5. A new numerical tool has been created to study transport in gyrokinetic simulations: the TRACER code

We have developed a new code that integrates particle trajectories in the turbulent fields generated by a gyrokinetic code. The code is modular and easily adaptable to accept input from multiple codes, once the magnetic field structure, the metric and the turbulent fields are provided. The tool can thus easily be adapted carry out transport studies not just with the GENE code used here, but with many other codes as well, both of the gyrokinetic or fluid kinds.

6.2 Future lines of research

There are several lines of work that have arisen or has been suggested by the activities carried out during this investigation. First, we would like to keep using TRACER to examine transport dynamics in other regimes and configurations. In particular, we would like to repeat the analysis carried out in Chapter 5 for the other two quasi-symmetries: quasi-helical symmetry and quasi-axisymmetry. This would provide a nice complement to the more traditional transport studies (more in the line of what we showed at the end of Chapter 2 for QPS) that are available in the literature [86, 87]. Currently, we are already starting to analyze a configuration from the HSX quasi-helical device [8] that also has a strong variation of

the degree of quasi-helical symmetry ratio in the radial direction. Another configuration that we would like to analyze is that of the W7-X stellarator, that has a different type of property: quasi-isodynamicity [36].

In addition, we would like to explore other regimes in which non-diffusive radial transport might be relevant in fusion plasmas. One such example is the study of near-marginal turbulence, which requires fully global gyrokinetic codes run in flux-driven setups (see discussion at the beginning of Chapter 2). TRACER has already been adapted to be capable of accepting input from another well-known gyrokinetic code that has such capabilities: GYSELA [104]. We expect to be able to carry out such studies in the near future.

Another question that we would like to investigate is the behaviour we have found in the QPS simulations regarding the α spatial exponent. The cut-off found that limits the mesorange to less than a decade has an origin that does not seem to be related to resolution, but to physics. Clearly, a new set of simulations would be required to explore this issue, which is something we would like to address soon. This may require the use of a global setup in GENE , except of the local, full-annulus one we have used. There are currently efforts in the GENE team to develop such a version, which might make this activity possible in the near future.

Finally, we have also worked, during the years required to complete this thesis, in the development of new methods to characterize the nature of radial turbulent transport that could complement what we have already done using propagators or the Lagrangian methods. In particular, the use of *transport kernels* [1, 105, 106, 107]. The purpose here is not to have another independent method to validate results, but to come up with reliable methods that do not require the detailed following of particle trajectories but that can work instead with Eulerian data. Although we have tested these approaches in simulations, this activity has its sights clearly set on applications to actual experiments, which is why it has not been included as part of this thesis work. This is a line of work that will continue in the next few years.

Appendix A

Introduction to Lévy distributions

Lévy distributions are also known in mathematics as *stable distributions* [90]. In probability theory, a distribution is stable if a linear combination of two independent series of a random sample has the same distribution except for a shift (parameter usually denoted as μ) or a rescaling of the distribution. Lévy distributions are attractor distributions for properly normed sums of independent and identically distributed random variables [90]. As in the classical central limit theorem, where the normed sum of random variables with finite variance tends to a normal distribution, the generalized central limit theorem refers to the sum of random variables with infinite variance that tends asymptotically to a Lévy distribution.

Among other things, Lévy distributions are characterized by their stability parameter $0 < \alpha < 2$ (when $\alpha = 2$, they reduce to the Gaussian pdf). They have heavy-tails in the sense that, in the limit of large argument, decay algebraically as $L_\alpha(x) \sim x^{-(1+\alpha)}$ (Fig. A.1). The fatness of the tails make these distribution like a finite variance, σ^2. In fact, considering the family of moments,

$$\langle |x|^s \rangle = \int dx L(x) |x|^s, \tag{A.1}$$

Lévy laws lack any finite moment with $s \geq \alpha$. An example of these distributions is the Cauchy distribution, for $\alpha = 1$. It lacks a finite variance, and also any other moment of order one or larger. Lévy distributions with $1 < \alpha < 2$ are sometimes called *Pareto-Lévy distributions.*

A.1 Characteristic funciton

There is not an analytical closed expression for stable distributions, except for a few of them (for instance, the Cauchy distribution, or the Gauss distribution as a limiting case). Nevertheless, their characteristic function $\varphi(k)$, defined as:

$$L(x) = \int_{-\infty}^{\infty} \varphi(k) e^{-ikx} dk \tag{A.2}$$

is analytic and given by [90]:

$$\varphi(k; \alpha, \beta, c, \mu) = \exp\left(i\mu k - |ck|^{\alpha}(1 - i\beta \mathrm{sgn}(k)\Phi)\right). \tag{A.3}$$

It is defined in terms of four parameters, including the α stability parameter previously discussed. $\beta \in [-1, 1]$ is the so-called skewness parameter and measures the asymmetry of the distribution, being 0 for symmetric ones. μ is the shift parameter, whilst c is just a rescale parameter. Finally, Φ is defined as

$$\Phi = \begin{cases} \tan\left(\frac{\pi\alpha}{2}\right) & \alpha \neq 1 \\ -\frac{2}{\pi}\log|k| & \alpha = 1 \end{cases} \tag{A.4}$$

A.2 Asymptotic behaviour

The tail behaviour of Lévy distributions is one of their most interesting properties. For $\alpha \neq 1$ it is algebraic, as previously metioned, and given by [90]:

$$L(x; \alpha, \beta, \mu, \sigma)(x) \sim \begin{cases} C_\alpha \left(\frac{1-\beta}{2}\right) c^\alpha |x|^{-(1+\alpha)}, & x \to -\infty \\ \\ C_\alpha \left(\frac{1+\beta}{2}\right) c^\alpha |x|^{-(1+\alpha)}, & x \to +\infty \end{cases} \tag{A.5}$$

where the constant C_α is given by:

$$C_\alpha = \frac{\alpha(\alpha - 1)}{\Gamma(2 - \alpha)\cos(\pi\alpha/2)}, \tag{A.6}$$

being $\Gamma(x)$ the Euler Gamma function.

A.3 Symmetrical stable distributions

Symmetrical Lévy distributions are defined as those with $\beta = 0$. Their characteristic function is just a stretched exponential function ($\varphi \propto e^{-|k|^{\alpha}}$). Gaussian and Cauchy distributions are example of these distributions. Fig A.1 show several symmetrical Lévy distributions for different values of the α parameter centred at $\mu = 0$ and with the scale factor $c = 1$. As can be seen, the distributions become more peaked at the center and develop fatter tails as the α value decreases towards 0.

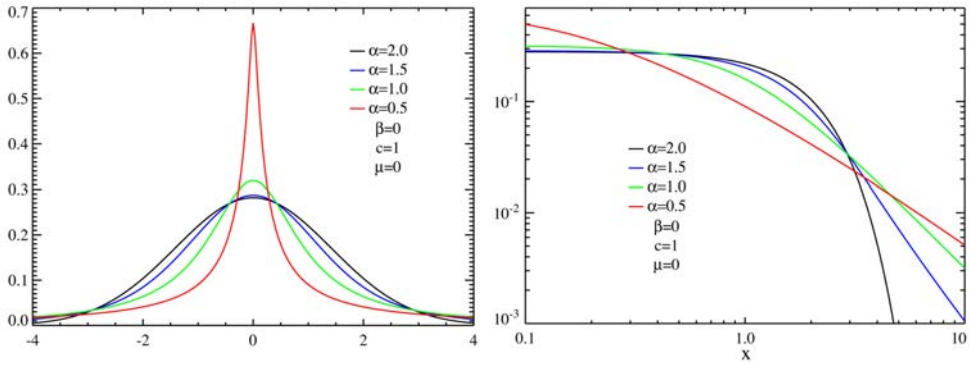

Figure A.1: Symmetric Lévy distributions for different α values in lin-lin (left) and (log-log) scales (right). The black curve is a Gaussian and the green curve is a Cauchy distribution.

A.4 Extremal stable distributions

If $\beta \neq 0$ the Lévy distribution is asymmetric. Some examples are shown in Fig. (A.2). Of particular interest is the extremal asymmetric case in which $\beta = \pm 1$, that is known as **extremal Lévy distributions**. Extremal Lévy distributions for $\alpha < 1$ are particularly interesting, since they have the property of only being defined on positive (if $\beta = 1$) or negative (if $\beta = -1$) values of their arguments, vanishing exponentially fast on the other side (see Eq. A.5). This property is quite interesting in some contexts related to the theory of fractional transport [108].

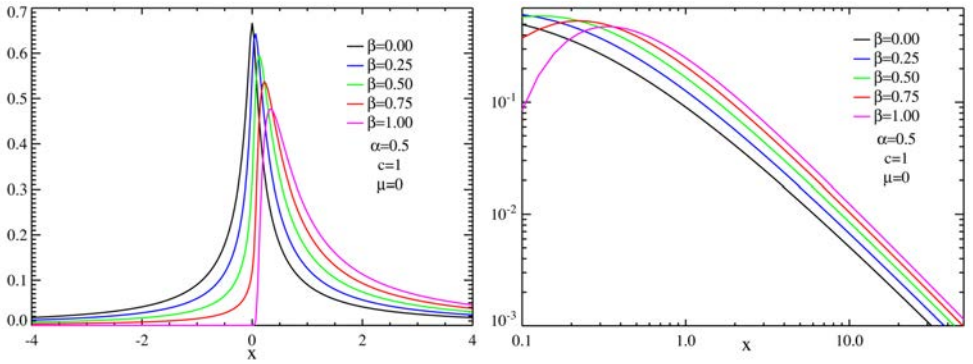

Figure A.2: Asymmetrical Lévy distributions for different β values and $\alpha = 0.5$ in lin-lin (left) and log-log (right) scales. Black curve is the symmetrical case (i.e., $\beta = 0$).

Appendix B

Introduction to fractional derivatives and integrals

Fractional derivatives (integrals) are integro-differential operators that provide smooth interpolants in between the more usual integer derivatives (integrals)[61, 62]. Although they are relatively old, they have seen renewed interest in the last decades in physics, particularly in context where non-diffusive transport is important.

B.1 Spatial fractional derivatives.

The definition of the spatial derivatives used in this thesis is related to the Rieman-Liouville definition of a fractional derivative [61, 62]. They read:

$$\frac{\partial^\alpha \phi}{\partial x^\alpha} = {}_{-\infty}D_x^\alpha \phi(x) = \frac{1}{\Gamma(m-\alpha)} \frac{d^m}{dx^m} \int_{-\infty}^{x} \frac{\phi(x')}{(x-x')^{1+\alpha-m}} dx', \qquad \text{(B.1)}$$

and,

$$\frac{\partial^\alpha \phi}{\partial (-x)^\alpha} = {}^{\infty}D_x^\alpha \phi(x,t) = \frac{-1}{\Gamma(m-\alpha)} \frac{d^m}{d(-x)^m} \int_{x}^{\infty} \frac{\phi(x',t)}{(x-x')^{1+\alpha-m}} dx', \qquad \text{(B.2)}$$

where $m-1 < \alpha < m$ with integer m. In this definition, α is the order of the derivative and $-\infty$ and ∞ are the low and upper limits of the integration respectively. In practical applications these limits must be truncated, which requires the normalization of these operators [95]. $\Gamma(x)$

represents the Euler Gamma function. These operators can be combined to define the symmetric Riesz fractional derivative [61]:

$$\frac{\partial^\alpha}{\partial|x|^\alpha} = -\frac{1}{2\cos\pi\alpha/2}[\ {}_{-\infty}D_x^\alpha + \ {}^{\infty}D_x^\alpha] \tag{B.3}$$

that plays an important role in fractional transport theory. The reason is that its spatial Fourier Transform is,

$$\mathcal{F}[\frac{\partial^\alpha\phi(x)}{\partial|x|^\alpha}] = -|k|^\alpha\phi(k) \tag{B.4}$$

which for $\alpha = 2$ tends to the Laplacian operator that appears in the classical diffusive equation (Eq. 3.3).

B.2 Temporal fractional derivatives

Since time is always positive, the starting point of the fractional derivatives is always $t_0 \geq 0$. In this thesis we always assumed that they are defined by the usual Riemann-Lioville expression [61]:

$${}_{t_0}D_t^\beta\phi(t) = \frac{1}{\Gamma(p-\beta)}\frac{d^p}{dt^p}\int_{t_0}^{t}\frac{\phi(t')dt'}{(t-t')^{\beta-p+1}}. \tag{B.5}$$

However, it is worth noting that in numerical applications this definition diverges when $t' \to t$, which forces the regularization of this operator. This is usually done in terms of the so-called Caputo fractional derivatives [109, 110, 111].

Appendix C

Publications and presentations of the results at international venues

Publications and Communications to Conferences and Workshops containing results included in this thesis:

- *"Determination of the nature of radial transport in quasi-symmetric stellarators configurations for the confinement of fusion plasma"*. J.A. Alcuson, J.M. Reynolds-Barredo, R. Sanchez and P. Xanthopoulos. Poster at IV FuseNet PhD-event. Lisbon, Portugal (2014).

- *"Development of tracer technology to characterize radial turbulent transport in stellarator geometry using the* GENE *gyrokinetic code"*. J.A. Alcuson, J.M. Reynolds-Barredo, R. Sanchez and P. Xanthopoulos. Poster at 19th Joint EU-US Transport Task Force Meeting. Culham, Abingdon, United Kingdom (2014).

- *"General Framework for statistical tracer analysis as a diagnostic for turbulent transport in gyrokinetic codes"*. J.M. Reynolds-Barredo, J.A. Alcuson, R. Sanchez and V. Tribaldos. Poster at 56th American Physical Society meeting of the Division of Plasma Physics. New Orleans, USA (2014).

- *"Influence of quasi-symmetries on the nature of radial turbulent transport"*. J.A. Alcuson, J.M. Reynolds-Barredo, A. Bustos, R.

Sanchez, V. Tribaldos and P. Xanthopoulos. Poster at V FuseNet PhD-event. Prague, Czeck Rep. (2015).

- *"Quasi-symmetry and the nature of radial turbulent transport in quasi-poloidal stellarators"*. J.A. Alcuson, J.M. Reynolds-Barredo, A. Bustos, R. Sanchez, V. Tribaldos, P. Xanthopoulos, T. Goerler and D.E. Newman. *Physics of Plasmas* **23** 102308 (2016).

Publications and Communications to Conferences and Workshops of other related results:

- *"Direct calculations of spatio-temporal transport kernels in simulations of near-marginal DTEM turbulence"*. J.A. Alcuson, J.A. Mier, D. del-Castillo-Negrete, D.E. Newman and R. Sanchez. Poster at 17th Joint EU-US Transport Task Force Meeting. Padua, Italy (2012).

- *"Characterization of the nature of transport in quasi-axisymmetric configuratons"*. J.A. Alcuson and R. Sanchez. Poster at II FuseNet PhD-event. Pont-a-Mousson, France (2012).

- *"New method for the transport nature characterization based on Integral Transforms"*. J.A. Alcuson, J.M. Reynolds-Barredo, J.A. Mier, D. del-Castillo-Negrete, D.E. Newman and R. Sanchez. Poster at III Fusenet PhD-event. York, United Kingdom (2013).

- *"Characterization of non-diffusive transport in plasma turbulence by means of flux-gradient integro-differential kernels"*. J.A. Alcuson, J.M. Reynolds-Barredo, J.A. Mier, R. Sanchez, D. del-Castillo-Negrete, D.E. Newman and V. Tribaldos. Poster at 57th American Physical Society meeting of the Division of Plasma Physics. Savannah, Georgia USA (2015).

- *"Characterization of avalanche-like transport in plasma turbulence by means of flux-gradient integro-differential kernels"*. J.A. Alcuson, J.M. Reynolds-Barredo, J.A. Mier, R. Sanchez, D. del-Castillo-Negrete and D.E. Newman. Poster at the Avalanches Processes in Condensated Matter Physics and Beyond Workshop. Barcelona, Spain (2017).

- *"Characterization of non-diffusive transport in plasma turbulence by means of flux-gradient integro-differential kernels"*. J.A. Alcuson, J.M. Reynolds-Barredo, R. Sanchez, J.A. Mier, D. del-Castillo-Negrete, and D.E. Newman. (to be submitted to *Physics of Plasmas*, 2017).

Bibliography

[1] R. Sanchez and D.E. Newman. *Plasma Phys. Contr. Fus.* **57**, 123002 (2015).

[2] P.H. Diamond and T.S. Hahm. *Physics of Plasmas* **2** 3640 (1995)

[3] D.E. Newman, B.A. Carreras, P.H. Diamond and T.S. Hahm. *Physics of Plasmas* **3** 1858 (1996)

[4] M.N. Rosenbluth. *Plasma Phys. Contr. Fus.* **41**, A99-A113 (1999).

[5] R. Sanchez, D.E. Newman, J. N. Leboeuf, V.K. Decyk and B.A. Carreras *Phys. Rev. Lett.***101** 205002 (2008).

[6] R. Sanchez, D.E. Newman, J.N. Leboeuf, B.A. Carreras and V.K. Decyk *Phys. Plasmas* **16** 055905 (2009).

[7] R. Sanchez, D.E. Newman, J.N. Leboeuf and V.K. Decyk *Plasma Phys. Control. Fusion* **53** 074018 (2011).

[8] F. S. B. Anderson, A. F. Almagri, D. T. Anderson, P. G. Mathews, J. N. Talmadge and J. L. Shohet, *Fus. Technology* **27**, 273 (1995).

[9] J.M. Canik, D.T. Anderson, F.S.B. Anderson, K.M. Likin, J.N. Talmadge and K. Zhai. *Phys. Rev. Lett.* **98**, 085002 (2007).

[10] S.P. Gerhardt, J.N. Talmadge, J.M. Canik and D.T. Anderson. *Phys. Rev. Lett.* **94**, 015002 (2005).

[11] P.W. Terry. *Rev. Mod. Phys.* **72**, 109 (2000).

[12] F. Jenko, W. Dorland, M. Kotschenreuther and B.N. Rogers *Phys. Plasmas* **7**, 1904 (2000).

[13] Energy Information Administration, U.S. Department of Energy. *"World consumption of primary energy by energy type and selected country groups, 1994-2004"* (2006).

[14] Energy Information Administration, U.S. Department of Energy. *"Short-term energy outlook".* (2009).

[15] Energy Information Administration, U.S. Department of Energy. *World outlook 2004* (2004).

[16] OPEC Secretariat. *World Oil Outlook 2008* (2008).

[17] REN21 Secretariat. *Renewable global status report: 2009 update REN21* (2009).

[18] International Energy Agency. *"Key world energy statistics 2007"* (2007).

[19] M. Schenider, S. Thomas, A. Froggatt and D. Koplow. *The world nuclear industry status report 2009"* (2009).

[20] M. Arjun and S. Scott. *"The nuclear power deception"* (1996).

[21] Nuclear Regulatory Commission. *Backgrounder on Chernobyl nuclear power plant accident"* (2009).

[22] R. Aymar, P. Barabschi and Y. Shimomura, Plasma Phys. Control. Fusion **44**, 519 (2002).

[23] J. Sheffield, Rev. Mod. Phys. **66** 1015 (1994).

[24] N.P. Taylor, E.T. Cheng, D.A: Petti and M. Zucchetti. *Overview of international waste management activities in fusion"* (2000).

[25] Huang, K . *Statistical Mechanics (2nd ed.)*, John Wiley and Sons, New York (1987).

[26] J. D. Lawson, *Proc. Phys. Soc. B* **70** 6 (1957).

[27] K. Miyamoto, *Plasma physics for Nuclear Fusion*, The MIT Press., Cambridge, Massachusetts and London, England (1980).

[28] R. Betti, R.Y, Chang, B.K. Spears, K.S. Anderson, J. Edwards, M. Fatenejad, J.D. Lindl, R.L McCrory, R. Nora and D. Shvarts. *Physics of Plasmas*, **17** 058102 (2010).

[29] J.A. Wesson. *Nucl. Fusion* **29** 641 (1989).

[30] *The JET Project-Design Proposal: EUR-JET-R5* (1976).

[31] M. Shimada et al. *Nuclear Fusion* **47** S1-S17 (2007).

[32] M. Wakatani, *Stellarator and Heliotron Devices*, Oxford Univ. Press., Oxford, England (1998).

[33] L. Spitzer Jr. *Phys. Fluids* **1** 253 (1958).

[34] Iiyoshi, A., et al. *Fusion Technology* **17**, 169 (1990).

[35] J. Sanchez et al. *Nucl. Fusion* **47** 10 S677-S685 (2007).

[36] C. Beidler et al. *Fus. Tech.* **17** 149 (1990).

[37] P. Helander, *Rep. Prog. Phys.* **77** 087001 (2014).

[38] D.A. Spong, S.P. Hirshman, L.A. Berry, J.F. Lyon, R.H. Fowler, A.S Ware, D. Alban, R. Sanchez, G.Y. Fu, D.A. Monticello, W.H. Miner and P.M. Valanju. *Nucl. Fusion* **41**, 711-716 (2001).

[39] A.H. Boozer, Phys. Fluids **24** 2002 (1981).

[40] J.A. Alcuson, J.M. Reynolds-Barredo, A. Bustos, R. Sanchez, V. Tribaldos, P. Xanthopoulos, T. Goerler and D.E. Newman. *Phys. Plasmas* **23** 102308 (2016).

[41] M.C. Zarnstorff el al. *Plasma Phys. Contr. Fus.* **43** A237-A249 (2001).

[42] A. Fick. *Annalen der Physik* **170**, 59-86 (1855).

[43] Pearson, K. *Nature* **72** 294 (1905).

[44] F.L. Hinton and R.D. Hazeltine. *Rev Modern Phys.* **48** 239 (1976).

[45] S.P. Hirshman and D. Sigmar *Nucl. Fusion* **21** 1089 (1981).

[46] A.J. Wootton et al. *Plasma Phys. Control. Fusion* **11** 1479 (1988).

[47] W. Horton. *Rev. Modern Phys.* **71**, 735 (1999).

[48] A. Banon. Thesis: *Gyrokinetic large eddy simulations*, Universite Libre de Bruxelles, Belgique (2012).

[49] S. Hamugachi and W. Horton. *Plasma Phys. Control. Fusion* **34** 203 (1992).

[50] B.G. Hong, F. Romanelli and M. Ottaviani. *Phys. Fluids B* **3** 615 (1991).

[51] R.J. Goldston. *Plasma Phys. Control. Fusion* **26** 87 (1984).

[52] R.R. Parker et al. *Nucl. Fusion* **25** 1127 (1985).

[53] R.E. Waltz. *Phys. Fluids* **28** 577 (1985).

[54] G.G. Craddock et al. *Phys. Plasmas* **1** 1877 (1994).

[55] C.W. Gardiner. *Handbook of stochastic methods*. Springer Verlag, Heidelberg (1997)

[56] R. Metzler and J. Klafter, Phys. Rep. **339**, 1 (2000).

[57] R. Balescu, *Aspects of Anomalous Transport in Plasmas*. IOP Publishers, Bristol (2005).

[58] B. Drossel and F. Sneppen. *Phys. Rev. Lett.* **69**, 1629 (1992)

[59] R. Balescu, *Phys. Rev. E* **51** 4807-4822 (1995).

[60] G Spizzo, R B White, S Cappello, and L Marrelli, *Plasma Phys. Contr. Fusion* **51** 124026 (2009).

[61] I. Podlubny, *Fractional Differential Equations*, Academic Press, New York (1998)

[62] K. Oldham and J. Spanier. *The Fractional Calculus.* Academic Press, New York (1974)

[63] P.A. Politzer, M.E. Austin, M. Gilmore, G.R. McKee, T.L. Rhodes, C.X. Yu, E.J. Doyle, T.E. Evans and R.A. Moyere. *Phys. Plasmas* **9** 1962 (2002).

[64] B.A. Carreras, B.P. van Milligen, M.A. Pedrosa and R. Balbin R. *Phys. Rev. Lett.* **80** 4438 (1998)

[65] B.A. Carreras, B.Ph. van Milligen, C. Hidalgo, R. Balbin, E. Sanchez, I. Garcia-Cortes, M.A. Pedrosa, J. Bleuel and M. Endler. *Phys. Rev. Lett.* **83** 3653 (1999).

[66] R. Sanchez, B.Ph. van Milligen, D.E. Newman, B.A. Carreras. *Phys. Rev. Lett.* **90**, 185005 (2003)

[67] P. Bak, C. Tang and K. Wiesenfeld. *Phys. Rev. Lett.* **59**, 381 (1987)

[68] T. Hwa and M. Kardar *Phys. Rev. A* **45**, 7002 (1992)

[69] F. Wagner. *Plasma Phys. Control. Fusion* **49** B1-B33 (2007)

[70] A.J. Brizard and T.S. Hahm. *Rev. Mod. Phys.* **79**, 421 (2007)

[71] J.A. Krommes. *Annu. Rev. Fluid Mech.* **44**, 144201 (2012)

[72] W.W. Lee. *Phys. Fluids* **26**, 556 (1983)

[73] GENE Development Team. GENE *: User Manual*, *http//www.ipp.mpg.de/ gene* (2013).

[74] P. Xanthopoulos, H.E. Mynick, P. Helander, Y. Turkin, G.G. Plunk, F. Jenko, T. Görler, D. Told, T. Bird and J.H.E. Proll, *Phys. Rev. Let.* **113**, 155001 (2014).

[75] W. Tang. Website: https://www.alcf.anl.gov/projects/global-simulation-plasma-microturbulence-petascale-beyond

[76] T. Görler. Thesis: *Multiscale effects in plasma microturbulence*, University of Ulm, Germany (2009).

[77] T. Hauff. Thesis: *Transport of energetic particles in turbulent plasmas*, University of Ulm, Germany (2009).

[78] X. Lapillonne. Thesis: *Local and global eulerian gyrokinetic simulations of microturbulence in realistic geometry with applications to the TCV Tokamak*, Eccole Polytechnique Federale de Lausanne, Swizerland (2009).

[79] F. Merz. Thesis: *Gyrokinetic simulation of multimode plasma turbulence*, University of Munster, Germany (2008).

[80] M.J. Pueschel. Thesis: *Electromagnetic effects in gyrokinetic simulations of plasma turbulence*, University of Munster, Germany (2009).

[81] T. Görler, X. Lapillonne, S. Brunner, T. Dannert, F. Jenko, F. Merz and D. Told, *Journal of Computational Physics* **230** 7053 (2011).

[82] D. Told. Thesis: *Gyrokinetic microturbulence transport barriers*, University of Ulm, Germany (2012).

[83] S.P. Hirshman and J. C. Whitson. *Physics of Fluids* **26**, 3553 (1983)

[84] P. Xanthopoulos, W.A. Cooper, F. Jenko, Yu. Turkin, A. Runov and J. Geiger. *Phys. Plasmas***16**, 082303 (2009).

[85] L.L. Lao et al. *Nuclear Fusion* **25**, 1421 (1985).

[86] W. Guttenfelder, J. Lore, D.T. Anderson, F.S.B. Anderson, J.M. Canik, W. Dorland, K.M. Likin and J.N. Talmadge. *Phys. Rev. Lett.* **101**, 215002 (2008).

[87] H. E. Mynick, N. Pomphrey and P. Xanthopoulos *Phys. Rev. Lett.* **105**, 095004 (2010).

[88] P. Xanthopoulos, G.G. Plunk, A. Zocco and P. Helander, *Phys. Rev. X* **6**, 021033 (2016).

[89] N. Laskin, I. Lambadaris, F.C. Harmantzis and M. Devetsikiotis. *Comp. Networks* **40**, 363-375 (2002).

[90] G. Samorodnitsky and M. S. Taqqu, *Stable non-Gaussian random processes*, Chapman & Hall, New York, NY (1994)

[91] B. B. Mandelbrot and J. W. van Ness, SIAM Rev. **10** 422, (1968)

[92] R. Sánchez, B. A. Carreras, D. E. Newman, V. E. Lynch and B. Ph. van Milligen, Phys. Rev. E **74** 016305 (2006)

[93] I. Calvo, R. Sanchez, B.A. Carreras and B. Ph. van Milligen. *Phys. Rev. Lett.* **99**, 230603 (2007).

[94] I. Calvo, R. Sánchez and B. A. Carreras, J. Phys. A. **42** 055003 (2009)

[95] D. del-Castillo-Negrete, B. A. Carreras and V. E. Lynch, Phys. Plasmas **11** 3854 (2004)

[96] D. del-Castillo-Negrete, B.A. Carreras and V.E. Lynch *Phys. Rev. Lett.* **94** 065003 (2005).

[97] J. A. Mier, R. Sánchez, L. García, D. E. Newman and B. A. Carreras, Phys. Plasmas **15** 112301 (2008)

[98] J.A. Mier, R. Sanchez, L. Garcia, B.A. Carreras, D.E. Newman *Phys. Rev. Lett.* **101** 165001 (2008).

[99] H. E. Hurst, Trans. Am. Soc. Civ. Eng. **116**, 770 (1951).

[100] M. Gilmore, C.X. Yu, T.L. Rhodes and W.A. Peebles. *Phys. Plasmas* **9**, 1312 (2002).

[101] T. Hauff and F. Jenko. *Phys. Plasmas* **13** 102309 (2006).

[102] W. H. Press, S.A. Teukolsky, W.T. Vetterling and B. P. Flannery. *Numerical Recipes, 2nd. Edition* Cambridge Univ. Press, Cambridge (1992).

[103] R. Sydora, V.K. Decyk and J.M. Dawson. *Plasma Phys. Contr. Fusion* **38** A281-A294 (1996).

[104] V. Grandgirard et al. *J. Comput. Phys.* **217**, 395 - 423 (2006)

[105] G. Dif-Pradalier, P. H. Diamond, V. Grandgirard, Y. Sarazin, J. Abiteboul, X. Garbet, P. Ghendrih, A .Strugarek, S. Ku, and C. S. Chang. *Phys. Rev. E* **82**, 025401 (2010)

[106] S. Futatani, D. del-Castillo-Negrete, X. Garbet, S. Benkadda and N. Dubuit. *Phys. Rev. Lett.* **109** 185005 (2012)

[107] J.A. Alcuson, J.M. Reynolds-Barredo, J.A. Mier, R. Sanchez, D. del-Castillo-Negrete, and D.E. Newman. *"Characterization of non-diffusive transport in plasma turbulence by means of flux-gradient integro-differential kernels"* (In preparation, 2017).

[108] R. Sanchez, B.A. Carreras and B.Ph. van Milligen. *Phys. Rev. E.* **71**, 011111 (2005).

[109] M. Caputo. *J.R. Astron. Soc. Can.* **13** 529 (1967).

[110] A. Saichev and G. Zaslavsky. *Chaos* **7** 753 (1997).

[111] D. del-Castillo-Negrete, *Phys. Plasmas* **13** 082308 (2006).